Freie Universität Berlin

Electronic Structure and Electron Transfer Dynamics at Dye-Semiconductor Interfaces Studied by Means of Time-Resolved XUV Photoelectron Spectroscopy

im Fachbereich Physik der Freien Universität Berlin
eingereichte Dissertation

zur Erlangung des akademischen Grades
eines Doktors der Naturwissenschaften (Dr. rer. nat.)

vorgelegt von

Mario Borgwardt

Berlin
Juli 2016

Gutachter:

1. *Prof. Dr. Emad F. Aziz (Betreuer)*
2. *Prof. Dr. Dr. h.c. mult. Ludger Wöste*
3. *Prof. Dr. Tobias Hertel*

Tag der Disputation: 27.02.2017

Meinem Vater
Uwe Borgwardt

Table of contents

Abbrevations and Symbols

PV	photovoltaic
PES	photoelectron spectroscopy
TOF	time of flight
MCP	micro-channel plate
HOMO	highest occupied molecular orbital
LUMO	lowest unoccupied molecular orbital
UHV	ultrahigh vacuum
UPS	ultraviolet photoelectron spectroscopy
XUV	extreme ultraviolet
XPS	X-ray photoelectron spectroscopy
CC	cross-correlation
DOS	density of states
DSSC	dye sensitized solar cell
(H)ET	(heterogeneous) electron transfer
ISC	intersystem crossing
IVR	intramolecular vibrational redistribution
IC	internal conversion
OPA	optical parametric amplification/amplifier
CB(M)	conduction band (minimum)
VB(M)	valence band (minimum)
FWHM	full width half maximum
FEL	free electron laser
HHG	high harmonic generation
FC	Franck-Condon factors
N719/N3	transition metal complexes
MLCT	metal to ligand charge transfer states
IL	ionic liquid
RZP	reflective zone plate
FTO	fluorine doped SnO_2

SCE	space charge effect
DM	drift mode
WAM	wide angle mode
TS	transient signal
E_F	Fermi level
E_g	band gap energy
E_{kin}	kinetic energy
E_{vac}	vacuum level
E_{pass}	kinetic energy
Φ_s	work function
U_p	Ponderomotive energy
I_p	ionization potential
$\hbar\omega$	photon energy
$h\nu$	vibrational energy
Δt	time delay between pump and probe

Chapter 1

Introduction

The necessity of developing sustainable and clean energy technologies becomes a very critical issue nowadays because of the tremendous increase of the carbon dioxide emission within the last centuries and its unequivocal impact on the earth's climate associated with the effect of global warming. The use of photovoltaic (PV) devices is one of the answers to satisfy the world's unavoidable growing demands in energy without producing the enormous amounts of greenhouse gases [1,2]. In the last decades, great efforts have been made to investigate new light harvesting assemblies with improved energy conversion efficiencies and to develop systems for photo-catalytic solar fuel generation.

In general, photovoltaic conversion relies on two sequential steps: photo-generation of charge carriers due to light absorption and their separation at charge-selective contacts [3,4]. Among the silicon-based solar cells, which dominate the commercial PV market at present, the dye-sensitized solar cell (DSSC) shows great promise as an inexpensive alternative to the costly silicon and is considered as an attractive candidate in the group of next generation devices. DSSCs are based on wide band gap semiconductors such as TiO_2 or ZnO, which are sensitized with specifically designed transition-metal dye compounds [5–7]. In contrast to silicon, the two functions related to charge generation and separation are distributed to different device parts. Incident solar radiation is absorbed and leads to an electronic excitation of the sensitizer, which can subsequently inject the electron to the conduction band of the semiconductor. The dye is restored to its neutral ground state by electron transfer from a surrounding electrolyte. A major enhancement was achieved in 1991 by Grätzel and O'Regan by introducing a nanoporous semiconductor electrode, which increases the effective surface area by orders of magnitude and results in a dramatically enhanced light harvesting efficiency [8]. This has triggered a remarkable growth in research activities and today DSSC devices have reached energy conversion efficiencies beyond 10% [9].

The photo-driven heterogeneous electron transfer (HET) across the nanostructured interface depicts one of the most crucial process in the DSSC [10]. Intense research during the last decades revealed that the HET process can occur on ultrafast timescales as compared to other competing reaction channels, giving rise to a high injection yield of electrons into the semiconductor. One important aspect for an efficient HET is the relative energy level alignment of the dyes donor and the semiconductor acceptor states. A typical example of the HET mechanism is illustrated in Fig. 1.1. The electronic ground state of the dye lies within the band gap of the semiconductor and the excited state of the dye is well above the conduction band minimum. The energy level position of the dyes donor state with regard to the empty acceptor states in the conduction band determines on the one hand the driving force for the electron transfer, but on the other hand, the excess energy represents a significant dissipation mechanism. Therefore, a detailed knowledge of the energy structure is inevitable to better understand various experimental aspects and to design systems with optimized energy match between the dye and the semiconductor states.

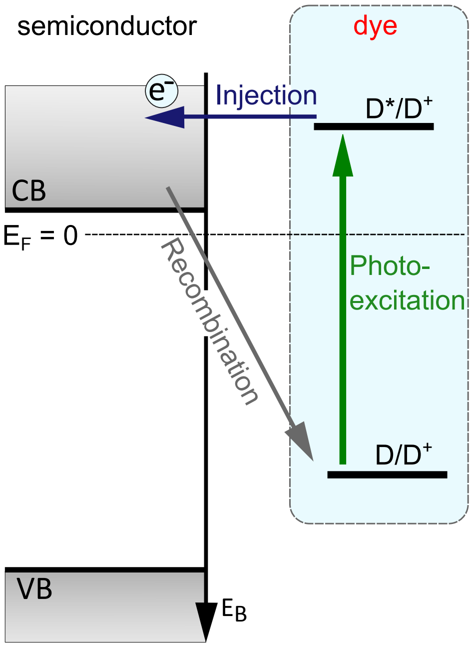

Fig. 1.1 Schematic view the band alignment at a dye-semiconductor interface. Following photoexcitation of the dye’s excited state, an electron is injected into the conduction band of the semiconductor.

Although a large number of studies provided a fundamental understanding of the charge-transfer kinetics, direct experimental knowledge of the energetics at the dye-semiconductor interface is not available until today. So far, transient absorption spectroscopy was the method of choice to gain insight into the ultrafast dynamics on a femtosecond timescale. This technique is based on the detection of relative changes in the absorption signals at the interface, which are related to the formation of positively charged dye cations or to the density increase of free electrons in the conduction band of the semiconductor. However, because of the indirect character of this method it does not provide a direct measure of binding energies and no conclusions about the relative level alignment between the dyes donor states and the semiconductor acceptor states can be drawn.

This issue constitutes the main scope of the thesis, which is designated to investigate the electronic structure and the dynamics of HET at dye-semiconductor interfaces by means of time-resolved XUV photoelectron spectroscopy (PES). The here presented studies demonstrate the capabilities and advantages of the PES approach in revealing both the injection kinetics and the binding energies of the involved states. In these experiments, high-energy photons are used to generate photoelectrons by means of ionization and the kinetic energy of the emitted electrons is used as the measure of their initial binding energy in the bulk material. In this context, the thesis can be seen as a required intermediate step towards the aim of establishing ultrafast PES as a routine technique for studying this type of interfaces.

To initiate the ionization step in a single photon process, sufficiently high photon energies are needed. Modern synchrotron light sources, which can fulfill this requirement, do not commonly provide coherent and ultrashort light pulses which, on the other hand, are required to achieve high temporal resolution. Only recently developed technologies such as accelerator-based free-electron-laser (FEL) [11,12] and the laser-based high harmonic generation (HHG) [13,14] are able to satisfy both demands, in the energy and time domains, and have opened up new perspectives in this field.

This thesis makes use of the latter laser-based approach – the up-conversion of the fundamental laser frequency in the process of high harmonic generation. A pump-probe technique is applied in the experiments, where the same laser system is used to generate optical pump pulses in the visible range at a wavelength corresponding to the maximum in the emission spectrum of the sun. Due to the intrinsic synchronization of the pump and probe pulses, the temporal resolution is only limited by their individual pulse durations and an overall resolution below 100 fs can be achieved. Such a resolution is highly suitable for the investigation of the ultrafast processes considered here. The HHG photon energies of up to 40 eV applied in this work enable to probe the entire valence-shell structure of both the semiconductor substrate and the sensitizer dye.

The thesis is organized as follows. In chapter 2, the theoretical aspects for this thesis are provided and an overview of the related physical background is given. In this chapter, the concepts and models are presented that are compared to the experimental data in the subsequent parts of the thesis. Chapter 3 describes the experimental setup that was used in the studies. It includes a detailed characterization of the spectral and temporal experimental parameters. The space charge effect, representing a general and important issue in PES studies with the use of ultrashort and intense light pulses, is also addressed in this chapter. The main part, chapter 4, contains the results obtained in this thesis. It is divided into three parts, whereas each subsection presents the study on a particular material system.

In the first investigation, the aim is to verify the currently established model of ultrafast charge transfer at the most commonly used TiO_2 interface and to gain additional information about the absolute binding energies for the involved excited states. Based on the current understanding, this approach explores the advantages of applying time-resolved PES to such kind of interfaces, and this study can be seen as a first benchmark to reveal the capabilities of the spectroscopic method.

The second investigation is focused on a particular issue which is related to the nanoporous ZnO substrates. Previous investigations reported that the HET occurs on much slower picosecond timescales as compared to the TiO_2 interfaces. The application of PES is proven to be beneficial to directly identify the possible origin of the delayed electron transfer, often related to the limited performance of ZnO-based cells. It will be shown below that due to the high surface sensitivity PES provides a valuable insight into the charge transfer mechanism.

The third investigation aims to extend the range of applications of time resolved PES with regard to electron dynamics in transition metal complexes. The reason is that in many cases light harvesting nanomaterials, commonly applied in photovoltaic devices, are utilized also as photo-catalytic materials. However, such a dual use depends critically on the charge carrier dynamics, and it requires deep knowledge of the energetic band alignment and the relaxation pathways in order to understand the functionality of these materials. Additional complications in experimental studies arise if the sample of interest requires a natural liquid environment. As in general the use of highly volatile liquids complicates the application of PES due to the need of suitable vacuum conditions, the thesis evaluates the possibility of using room temperature ionic liquids (IL) as an alternative. This type of solvents is known to exhibit extremely low vapor pressures, being perfectly suited for UHV application. The transition metal complex $[Ru(bpy)_3]^{2+}$ is used as a prototype and its ultrafast intramolecular dynamics are investigated by means of time resolved PES. Hereby, the general applicability of ILs as solvents in view of their stability under UHV conditions, the visibility of the solute signatures, and regarding the solvent-solute interaction is characterized in detail.

Finally, the results are summarized in chapter 5 and an outlook for further research activities is presented.

Chapter 2

Theoretical Background

This chapter introduces the most important theoretical aspects that are necessary for the understanding of this thesis. At first, a brief introduction to the principles of electron transfer (ET) is presented, depicting the main subject throughout this investigation. Subsequently, based on a profound literature review, a detailed characterization of the experimental systems studied in this work is given. This includes the consideration of properties of the employed dye complexes as well as of the semiconductor substrates. The interaction between the molecules and the substrates is discussed in terms of the energetic alignment between molecular electronic levels and the band structure of the semiconductors. Finally, the theoretical basics of ultrafast spectroscopy are presented regarding the generation of ultrashort laser pulses and their frequency up conversion in the process of high order harmonic generation. In this context, the fundamentals of transient photoelectron spectroscopy are outlined. This chapter addresses solely the theoretical background of the thesis. Its practical implementation in terms of the used experimental setup is described in chapter 3.

2.1 Electron Transfer Theory

Electron transfer (ET) processes play an important role in biological, chemical and physical systems [15]. Some well-known examples are photosynthesis, photo catalysis and dye-sensitized solar cells [16–18]. Hereby, an electron is transferred from a donor (D) to an acceptor (A) without any change in chemical bonds:

$$D \;+\; A \;\longrightarrow\; D^{+} \;+\; A^{-} \tag{2.1}$$

Depending on the involved donor and acceptor species, one can distinguish between homogeneous and heterogeneous ET. Homogeneous ET takes place between two equal species, e.g. two organic molecules. Contrary to this case, heterogeneous ET (HET) involves the reaction between two different species. The latter process, which represents the object of this study, is of great importance in artificially created systems, such as for instance the ET from an optically excited molecule into a semiconductor.

The first theoretical model to describe the ET reactions was given by Marcus in 1956 [19]. Originally it was developed to explain outer-sphere electron transfer reactions, in which two non-connected species change only their charge via the electron transfer process, without undergoing any large structural changes. The main important theoretical aspect of the Marcus theory lies on its direct correlation between kinetic and thermodynamic quantities. This description was later extended to covalently linked reactants and since then a number of different advances were done, especially noteworthy by Hush [20], Jortner [21] and Hopfield [22]. Aside from these seminal studies, Gerischer and co-workers introduced the basic understanding of the electrochemistry of electrodes related to the HET reactions [23]. In the past decades, a number of review articles were published in which a more detailed description can be found [15,17,18,24–29]. In the following discussion, the fundamental principles of ET reactions will be outlined on the basis of homogeneous ET. The particular characteristics of the HET are subsequently addressed by focusing on the main differences between both processes.

2.1.1 Homogeneous Electron Transfer

Marcus classical theory describes the nuclear motion in terms of harmonic oscillators, with an effective frequency ν along the reaction coordinate being identical for both the reactant and product states. An important characterization of ET processes is given by the strength of the electronic coupling between the reactant and product. If the coupling is weak and the potential energy surfaces are not altered, one speaks of the non-adiabatic (diabatic) case. Such a situation is illustrated in Fig. 2.1. It shows the two energy surfaces of the reactant (here denoted by the excited donor and acceptor pair D*-A) and the product (the positively charged donor and negatively charged acceptor D^+-A^-) along the reaction coordinate. The reaction coordinate is an abstract coordinate used to describe the progress of the ET reaction and has not to be directly related to any molecular extension.

Further the quantities $\Delta G^{\#}$ and ΔG^0 represent the activation energy, determined by the classical barrier height, as well as the standard Gibbs free energy, respectively. The parameter λ describes the reorganization energy of the system that is defined as the energy required to force the reactant from the initial coordinates to have the same final nuclear configuration as the product, without making the electron transfer.

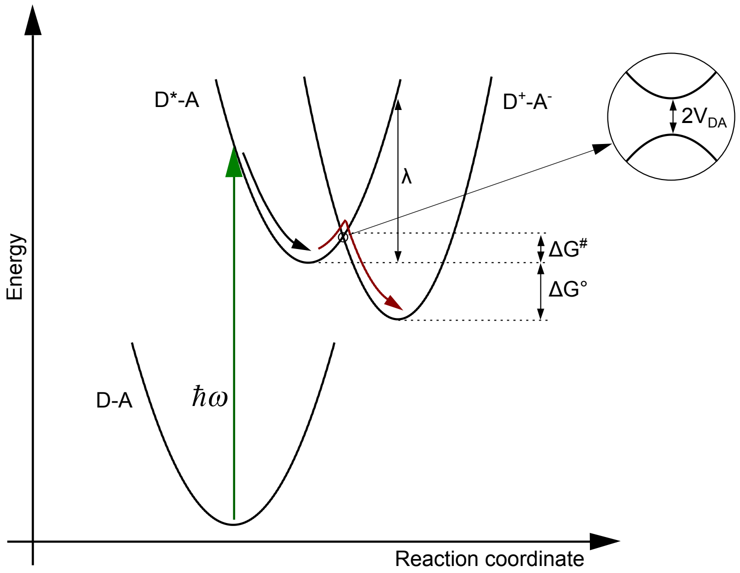

Fig. 2.1 Schematic illustration of an ET reaction initiated by an optical excitation (photoinduced ET). Three one-dimensional harmonic oscillator potential curves are shown, representing the donor-acceptor ground state (D-A), the excited donor and acceptor pair (D*-A) (reactant), and positively charged donor and negatively charged acceptor pair (D^+-A^- (product), respectively. The ET reaction occurs in the non-adiabatic limit. Important reaction parameters are indicated by the activation energy $\Delta G^{\#}$, the Gibbs free energy ΔG^0 and the reorganization energy λ, respectively. The inset depicts the level splitting of the parabolas of the reactant and the product due to the avoided crossing of the electronic states. The splitting is expressed in terms of the coupling strength V_{DA}.

Considering that the electron is moving within the reactant potential term represented by the harmonic oscillator parabola, it crosses the transition point repeatedly, giving rise to a transition probability into the product state due to the weak coupling V_{DA} between the electronic states. The standard quantum mechanical approach in terms of the first order perturbation theory can be applied to describe this transition. This leads to the Fermi's Golden rule [20,30–32] which gives an expression for the ET rate:

$$k_{ET} = \frac{2\pi}{\hbar} |V_{DA}|^2 \, (FCWDS) \,, \tag{2.2}$$

where V_{DA} is the electronic coupling matrix element between the reactant and the product state and FCWDS is the Franck-Condon weighted density of states. The FCWDS factor represents the overlap integral between the wave functions of the reactant and product states [33]. Although Eq. 2.2 appears to be rather simple, the calculation of the both terms turned out to be difficult on a microscopic level and was therefore subject of intense research during the last decades. The FCWDS factor expresses the probability of reaching the transition state. It can also be calculated classically on the basis of the Boltzmann statistics and depends on the activation barrier height as well as on the thermal energy taken from the system:

$$FCWDS_{classical} \propto \exp\left(\frac{-\Delta G^{\#}}{k_B T}\right) \tag{2.3}$$

Considering the transition at the crossing point of the two harmonic oscillator parabolas, one can derive the relation between the standard Gibbs free energy ΔG^0, the barrier height $\Delta G^{\#}$, and the reorganization energy λ. Marcus first derived this very important relation which reads:

$$\Delta G^{\#} = \frac{\lambda}{4}\left(1 + \frac{\Delta G^0}{\lambda}\right) \tag{2.4}$$

Combining Eqs. 2.2-2.4 together, one obtains the well-known Marcus dependency describing the ET rate [19,34]:

$$k_{ET} = \frac{2\pi}{\hbar}\frac{1}{\sqrt{4\pi\lambda k_B T}}|V_{DA}|^2 \exp\left(-\frac{(\lambda + \Delta G^0)^2}{4\lambda k_B T}\right) \tag{2.5}$$

This result features two important consequences. At first, the maximum transition rate is achieved if the free energy matches the reorganization energy. In this case the activation barrier vanishes and the value for λ can be experimentally determined. The second issue is the separation of the normal region $-\Delta G^0 < \lambda$ from the inverted $-\Delta G^0 > \lambda$ region. It is somewhat counterintuitive that the reaction rate decreases when the free Gibbs energy becomes more negative. One would expect in this case that the driving force should increase. However, the validity of the above equation and the existence of the inverted region was experimentally proven [35].

The classical treatment of the FC factor remains valid as long as the oscillator frequency ν is low and the thermal energy is greater than $h\nu$. Otherwise the harmonic potential energy surfaces of the reactant and product have to be described in terms of quantum mechanics. Two such attempts are reported by Bixon and Jortner [21,36], who applied a quantum mechanical approach to describe the intramolecular vibrational motion. As a first result, the energy surfaces spilt at the crossing point by $2|V_{AD}|$ and the actual crossing of both parabolas is avoided, as shown in the inset of Fig. 2.1. However, the predictions for the dependency of the transfer rate k$_{ET}$ given by the Marcus classical approach can also be found descriptively in the quantum mechanical picture [37]. As described before, the transition probability between vibrational eigenstates of the two different electronic states, expressed by the FC factor, is proportional to the overlap of the vibrational wave functions. Differently to the typical consideration of the FC factors for optical transitions, the parabolas of the electronic states for the ET reaction are treated in the manner represented by Fig. 2.2. The FC factor between the vibrational state n in the reactant electronic state and n' in the product state is defined by:

$$FC \propto |<n|n'>|^2 \tag{2.6}$$

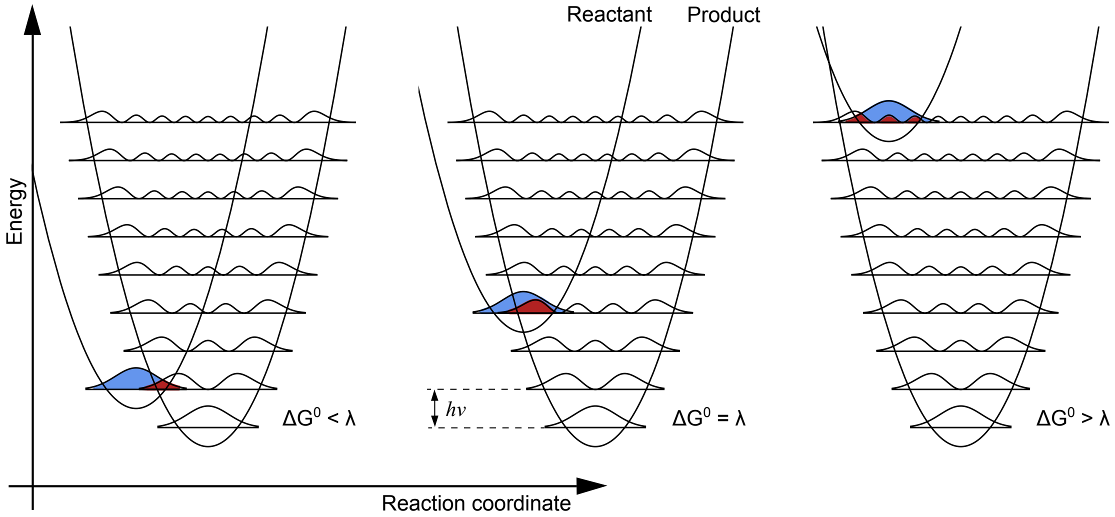

Fig. 2.2 Electron transfer reactions for three different free energies depicted by parabolic potential energy surfaces. The probability density of the quantum mechanical oscillator wave functions for different vibrational states n are illustrated and superimposed to the parabolas. The transition probability is given by the overlap of the vibrational wave functions (FC factors) represented by the red colored area. Maximum overlap is achieved when the reorganization energy is equal to the free Gibbs energy $\lambda = -\Delta G^0$ as shown in the center.

This is illustrated for the case of harmonic oscillator levels separated in both cases by $h\nu$. For the reactant parabola, only the lowest vibrational state (n=1) is shown whereas for the product parabola the vibrational states up to the free energy ($h\nu n' = \Delta G^0$) are sketched. As the energy increases in the product state, the probability density becomes concentrated at the classical "turning points", where the state's energy coincides with the potential energy. The maximum overlap between the lowest vibrational state of the reactant is found for the particular wave function in the product state satisfying $\lambda = -\Delta G^0$. It is important to note that to obtain the complete FCWDS factor in Eq. 2.2 one has to add up all single FC factors of the allowed transitions, weighted by the population of the different reactant vibrational levels.

As illustrated in Fig. 2.1, ET reactions can be photoinduced via preparing the reactant in a locally excited state. Hereby the vertical transition populates usually higher vibrational excited levels due to the Frank-Condon principle. Beside the ET reaction, a competing intramolecular thermalization can take place on similar timescale. Thus, the previously discussed static picture has to be extended to a dynamical description of the ET process. In this case the ET can occur either from the vibrational hot or equilibrated reactant state or from a state in between. This implies that the populations of the excited state becomes time-dependent, which has to be considered during the calculation of the total FCWDS factor.

Adiabatic limit

The previously described models are only valid if the electronic coupling is weak. That is the case where the frequency of the nuclear motion is larger than the ET rate. In the non-adiabatic limit, the transition probability at the crossing point was assumed to be much smaller than one. However, for the strong electronic coupling, representing the adiabatic limit, the transition probability reaches nearly one. Thus, the energy level splitting at the crossing point becomes larger and the two parabolas for the reactant and product state cannot be distinguished in this region. Therefore, the system has to be treated in terms of a single potential energy surface. The same electronic wave function, initially localized on the reactant site, is used to describe the electron motion along this potential surface. By rearrangement of the nuclear configuration, the electronic wave function becomes localized more preferably at the product site. In the presence of a solvent its contribution to the reorganization energy λ typically exceeds the intramolecular part. This introduces an additional upper limit for the ET rate given by the relaxation time of the surrounding medium, which is usually approximated by its longitudinal dielectric relaxation time [30,32,38,39].

2.1.2 Heterogeneous Electron Transfer

Most of the previously described fundamental principles for the homogenous ET are also valid for the heterogeneous case. Since the heterogeneous ET depicts the main subject of this investigation the important difference are explained in this section.

The most significant difference is that the number and the energy of accessible acceptor states are dramatically modified when the molecular acceptor is exchanged by a solid state one [23,36]. For a dye molecule chemically bound to a semiconductor, the conduction band is assumed to be a continuum of electronic states. The discrete molecular donor level, again given by its excited state, overlaps with a whole series of acceptor states. A special situation arises, if the energy difference between the molecular donor level and the conduction band minimum of the semiconductor is larger than the reorganization energy λ of the ET reaction. In the so called “wide band limit”, every vibrational state of the donor can be coupled to a particular acceptor state of the conduction band independently of the molecules nuclear configuration [40,41]. This condition is illustrated in Fig. 2.3, which shows that every point of the donor parabola can be a transition point. That means that for each reactant state the overlap with any product state is maximal and the total Franck-Condon weights sums up to one. Therefore, the FCWDS in Eq. 2.2 can be replaced by the pure density of states (DOS) factor [42,43]:

$$k_{ET} = 8\pi\hbar|V_{DA}|^2 DOS. \tag{2.7}$$

The DOS factor is given by the density of states of the semiconductor as well as by the vibrational state density of the molecule. However, these factors represent stationary properties of the investigated systems and, thus, the DOS factor is constant. Since the ET is not limited by the frequency of the nuclear motion that translates the system to the transition point, the ET rate can become very high. However, if the donor state approaches the conduction band minimum the wide band limit is not valid anymore. In this case the FCWDS summation has to be reconsidered due to fact that less acceptor states are available.

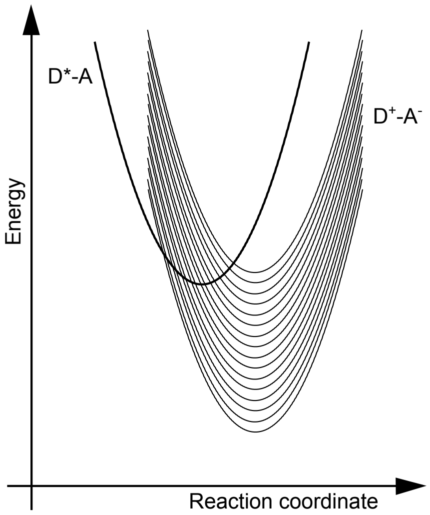

Fig. 2.3 Schematic illustration of the non-adiabatic HET from a molecular donor to a solid state acceptor. The excited donor state (D*-A) overlaps with a large number of continuous bulk acceptor states.

It is important to note that after electron injection from the molecular donor into the solid state acceptor the wave function of the electron becomes delocalized in the three dimensional continuous bulk states. This leads to a reduced probability for the electron to immediately return to the initial donor state after the ET. If the dephasing of the system would not exist, an echo-like periodical recurrence would be formed. In real systems electronic dephasing occurs due to, e.g., inelastic scattering processes, leading to the electron relaxation in the conduction band of the semiconductor within tens of femtosecond. This makes any ET highly irreversible.

In conclusion, the ET rate depends on three main factors if charge transfer in heterogeneous system is considered. As pointed out above, the rate is given by the DOS in the semiconductor coupled to the electron donating states. This can be expressed by the conduction band properties of the used semiconductor and the electronic orbital configuration of the dye. This aspect will be described in the next section. Further, the energy difference between the electron donor and acceptor states is important. The experimental determination of this quantity, accessible by means of photoelectron spectroscopy, represents the main subject of this work and the results on different dye/semiconductor interfaces will be presented in chapter 4. Finally, the coupling between the electron donating and electron accepting states determines the ET rate. The theoretical calculation of the coupling matrix element has been a subject of many studies before. However, computational efforts are demanding especially in the case of heterogeneous ET were a solid electron acceptor is involved.

2.2 Experimental Systems

In this section the investigated systems, consisting of transition metal complexes and nanostructured semiconductor substrates, will be introduced. In the first part, the individual properties and material characteristics are summarized. This is followed by a description of the dye-semiconductor interface based on a literature review. Hereby, important aspects such as the binding geometry, electronic interaction between donor and acceptor as well as the band alignment are outlined. The section is concluded with a description of the sample preparation method, which has been found to be of great importance in affecting the microscopic properties of the investigated systems.

2.2.1 The Dye Molecules

In this thesis, exclusively ruthenium-based transition metal complexes were examined [44,45]. A classical example, which has also served as a prototype and a model system of intramolecular electron and energy transfer reactions, is $[\mathrm{Ru(bpy)_3}]^{2+}$ where bpy stands for 2,2'-bipyridine [46]. It represents one of the most studied coordination compound [47–49] exhibiting a very high photosensitivity combined with favorable redox properties of the excited state [50]. These particular properties make the coordination compound to act as an extremely efficient photo catalyst for many applications, where either energy or electron transfer reactions are involved. One important aspect of this type of compound is that their absorption bands can be tuned by means of synthetic chemistry. This ability led to the invention of a huge number of dye complexes, called sensitizers, derived from the original molecule with regard to a more efficient absorption of the solar spectrum, binding geometry to the substrate and energy level alignment between donor and acceptor. The two most successful ruthenium-based sensitizers are $[\mathrm{Ru(dcbpyH)_2(NCS)_2}]$ (commonly termed N3), where dcbpy is 4,4'-dicarboxy-2,2'-bipyridine, and N719, the corresponding bis(tetrabutyl) ammonium salt. In the following, the fundamental photo physics of $[\mathrm{Ru(bpy)_3}]^{2+}$ are outlined, followed by a discussion on the similarities and differences of the specifically designed compounds.

$[\mathbf{Ru(bpy)_3}]^{2+}$

The molecular structure of $[\mathrm{Ru(bpy)_3}]^{2+}$ in its crystalline form was determined by X-Ray diffraction [51,52]. It exhibits a trigonal distorted octahedral symmetry (D_3 symmetry) and is illustrated in Fig. 2.4. Three bipyridine ligands (bpy in the following) surround the ruthenium atom and are bound to the metal center via their two nitrogen atoms as bidentate chelating ligands. All six nitrogen atoms possess an equal bond distance to the central ruthenium atom of 2.056 Å [51]. In an ideal octahedral symmetry, the angles alternately spanned by the N – Ru – N atoms would be 90°. However, due to a steric constraint originating from the short C-C bridging bond in bpy, the N – Ru – N angle within the same ligand appears to be smaller and has a value of 78.7°. This leads to a molecular symmetry possessing one three-fold rotational C_3 axis and three two-fold rotational C_2 axes.

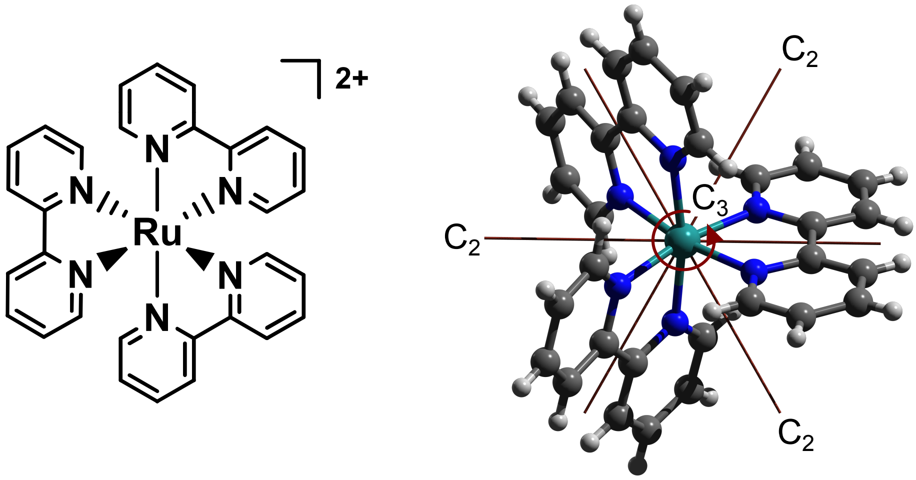

Fig. 2.4 The chemical structure of $[\mathrm{Ru(bpy)_3}]^{2+}$ (left). Three bipyridine ligands surround the ruthenium atom and bind via their two nitrogen atoms. In the three dimensional view (right) the C_2 and C_3 rotational axes are indicated.

In the absence of any ligand field, the d orbitals of the Ru center are degenerate. In octahedral symmetry (O_h) the degeneracy is lifted into the doubly degenerate e_g and the triply degenerate t_{2g} orbital bands [53]. The parameter Δ describing the energetic gap between both bands is called the ligand field splitting. The reason for the breaking of the degeneracy is given by the orientation of the orbitals relative to the coordinating ligands. The e_g orbitals are oriented in the direction of the ligands and are, therefore, raised in energy, whereas the t_{2g} orbitals are not oriented in the direction of the ligands and are lowered in energy. Considering the additional distortion of the octahedral symmetry resulting in the tetragonal D_3 symmetry, the t_{2g} orbital split further into a single degenerate a_1 and double degenerate e orbital. The splitting is summarized in the scheme of Fig. 2.5(a).

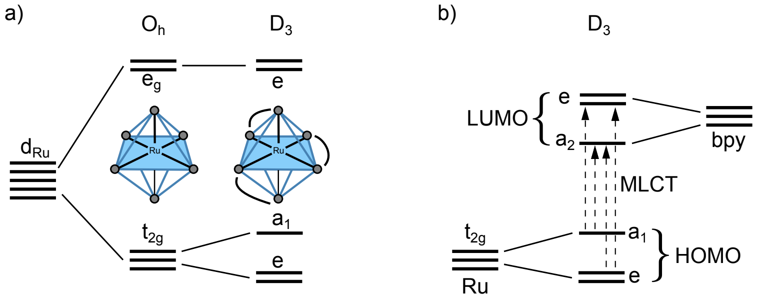

Fig. 2.5 (a) Energy level scheme of the Ru metal 4d orbital in the octahedral (O_h) as well as the trigonal distorted (D_3) symmetry. The former leads to a splitting of the initially degenerate level into t_{2g} and e_g orbitals. The degeneracy of the t_{2g} orbital is additionally lifted by the D_3 symmetry. (b) The frontier orbitals of $[Ru(bpy)_3]^{2+}$ mapped from octahedral to the D_3 symmetry. The highest occupied molecular orbital (HOMO) is localized at the metal center whereas the lowest unoccupied molecular orbital (LUMO) is localized at the ligand. Indicated by the vertical arrows are the four possible metal-to-ligand charge transfer (MLCT) states.

Each bpy ligand has a two-fold rotational symmetry (C_2) bisecting the pyridine rings. The π bonding orbitals are symmetric with respect to this axis and are energetically separated from the anti-bonding orbitals, which are antisymmetric aligned. In the reduced D_3 symmetry of the molecule, the anti-bonding orbitals of the bpy ligands split into the single degenerate a_2 orbital and the double degenerate e orbital.

The mixing of the metal d orbitals with the π^* anti-bonding orbitals of the ligand form the highest occupied molecular orbitals (HOMO) and the lowest unoccupied molecular orbitals (LUMO) as shown in Fig. 2.5(b). Due to the large energy difference between the occupied metal d orbitals and the unoccupied ligand orbitals, the HOMO is primarily localized at the metal. Differently from that, the LUMO resides mainly at the antibonding orbitals of the ligand. Therefore, the excitation from the HOMO to the LUMO is called as metal-to-ligand charge transfer (MLCT) and gives rise to an photoabsorption band structure in the wavelength range between 380 and 520 nm [49]. Due to the overlap with the visible spectral range, the MLCT transition represents the most important absorption channel, when the molecule is utilized as a photosensitizer. The optical absorption spectrum of $[Ru(bpy)_3]^{2+}$ is shown in Fig. 2.6(a). Beside the MCLT transition three other minor important transitions are visible and summarized in the inset of Fig.2.6(a). The UV range is dominated by strong transitions involving the ligands π bonding orbitals and π^* anti-bonding orbitals. They are called ligand-centered (LC) ($\pi_{bpy} \rightarrow \pi^*_{bpy}$) and ligand-to-metal charge transfer (LMCT) ($\pi_{bpy} \rightarrow e_{g,Ru}$). In between another absorption band can be assigned to the metal-centered (MC) ($t_{2g,Ru} \rightarrow e_{g,Ru}$) transition [54].

A simplified energy level scheme of the photochemical cycle of $[Ru(bpy)_3]^{2+}$ can be seen in Fig. 2.6(b). Optical excitation of the MLCT absorption band lifts a metal valence

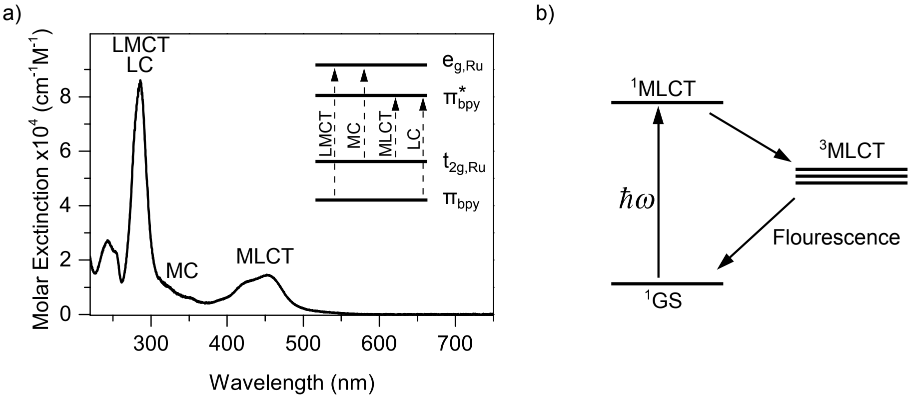

Fig. 2.6 Absorption spectrum of $[Ru(bpy)_3]^{2+}$ in water measured by Jenway 7315 spectrophotometer (a). The inset shows the four possible transitions, labeled according to the involved molecular orbitals. (b) Simplified energy level scheme of the photochemical cycle of $[Ru(bpy)_3]^{2+}$ upon a MLCT excitation. Absorption of a photon in the visible wavelength range promotes an electron from its singlet ground state ^{1}GS into the ^{1}MLCT state. Due to ultrafast intersystem crossing, it relaxes to the long-lived ^{3}MLCT state followed by a radiative decay to the ground state.

electron from its singlet ground state (^{1}GS) configuration and leads to the formation of a Franck-Condon singlet metal-to-ligand charge transfer ^{1}MLCT state [55–57]. The electron, localized at one of the bpy ligands, undergoes ultrafast intersystem crossing (ISC) and relaxes to the long-lived triplet state ^{3}MLCT˜[58]. The lifetime of the ^{3}MLCT was found to be in the order of one microsecond before the system relaxes to the ground state [59]. A more detailed description will be given in the scope of the discussion presented in section 4.3, where the ultrafast dynamics of $[Ru(bpy)_3]^{2+}$ dissolved in ionic liquids will be considered.

N3 and N719

The application of $[Ru(bpy)_3]^{2+}$ as a redox sensitizer was intensively studied because of its very long-lived excited state. One major disadvantage is the lack of absorption in the red region of the visible spectrum. This leads to losses in the potentially achievable efficiency if the dye is utilized as an absorber in a solar cell. Therefore, other Ru-based dye molecules were investigated as well as specifically designed to satisfy the required needs. One important class are the closely related bis(2,2'-bipyridyl) Ru-complexes. In the early days, they have not been considered as suitable sensitizers due to their relatively short-lived excited state, which was thought to result in a low photon-to-electron conversion yield. In general, the properties of this class of dyes are closely related to $[Ru(bpy)_3]^{2+}$. However, it was found that an ultrafast heterogeneous electron injection from the dye attached to a semiconductor appears, thus, competing with the deactivation of the excited state[60]. Since then increased research interest led to the invention of many new dye complexes.

In 1993 Nazeeruddin introduced the so called N3 sensitizer, where one bpy ligand is replaced by two thiocyanate groups, and has additionally carboxylate groups as anchoring sites [61]. The chemical structure is shown in Fig. 2.7. With the use of N3 in a solar cell, an efficiency increase of up to 10% was reached, setting a benchmark for all dyes that followed.

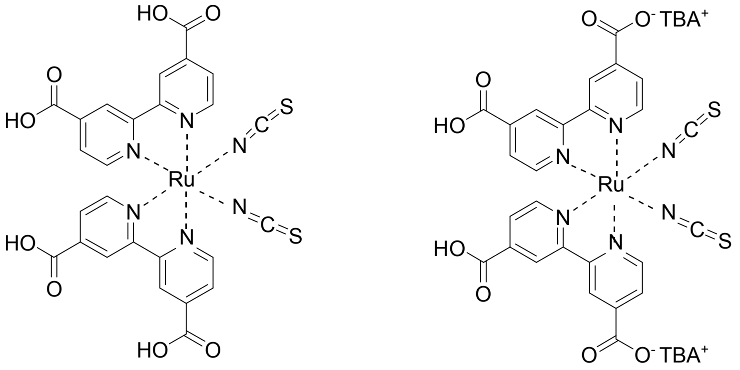

N3 **N719**

Fig. 2.7 Chemical structures of the N3 (left) and N719 (right) Ru-based transition metal complexes.

One possibility to improve the conversion efficiency is a change in the protonation of the anchoring groups. Due to the fact that the protons are partially transferred to the surface of the semi-conductor substrate, they might influence the energy level alignment. One attempt was done for the dye N719 where two protons were exchanged by a tetra-butyl-ammonium (TBA) group. Slightly better performance was found, which includes N719 into the group of reference dyes. A comparison of the absorption spectra of both dyes in ethanol is shown in Fig. 2.8. For N3 and N719 the maximum of the MLCT band is red shifted to a wavelength of 530nm, as compared to the $[Ru(bpy)_3]^{2+}$ complex.

The N3/N719 complexes are covalently bonded to the substrate via their carboxylate groups. This electronic interaction influences the excited state of the dye and depends additionally on the adsorption geometry of the molecule. A comparison of the absorption spectra of N3 in ethanol and attached to ZnO substrate is shown in Fig. 2.9. The most apparent difference is the shift of the MLCT absorption band by 30 nm to shorter wavelengths in the N3/ZnO spectrum. The spectral response was found to be dependent on dye concentration and on residence time of the ZnO film in the dye solution. Further details are presented with regard to the sample preparation in section 3.3.

The photochemical cycle of N3/N719 is similar to the one described above for $[Ru(bpy)_3]^{2+}$. A more detailed description will be presented at the relevant points in the thesis. The N719 dye is utilized in the study of the ultrafast charge transfer from a sensitizer to a nano colloidal TiO_2 semiconductor substrate (section 4.1). A similar study, but particularly focused on the formation of an interfacial charge transfer state, was performed with N3 deposited on a ZnO electrode (section 4.2).

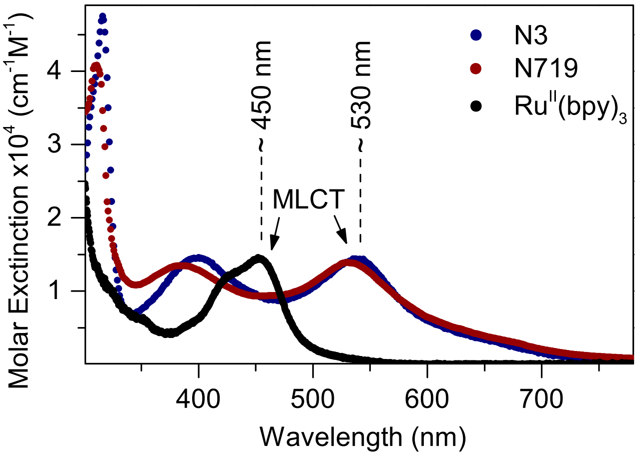

Fig. 2.8 Comparison of the absorption spectra of N3, N719 and $[Ru(bpy)_3]^{2+}$ in ethanol measured by Jenway 7315 spectrophotometer. The MLCT transitions are indicated with their maximum located at 530 nm for N3/N719 and 450 nm for $[Ru(bpy)_3]^{2+}$.

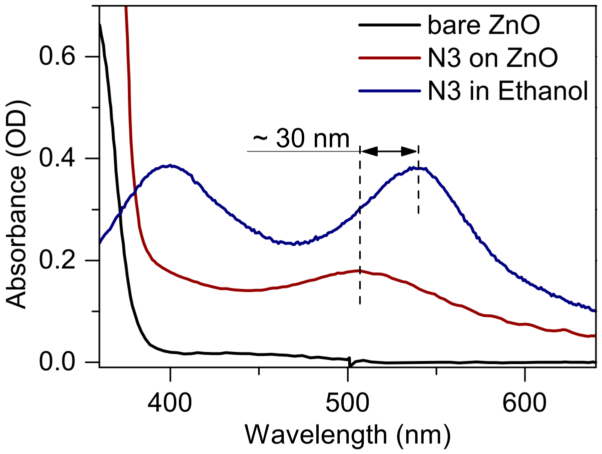

Fig. 2.9 Absorption spectrum of bare and N3 sensitized ZnO films. Additionally the spectrum of N3 in ethanol is shown. A distinct shift of 30 nm and a broadening due to the substrate dye interaction is found.

2.2.2 The Substrates

This section gives a short overview of the fundamental properties of the substrates used in this work.

Titanium Dioxide

Titanium dioxide (TiO_2) is a very versatile and well investigated semiconductor [62–65]. The most important examples for the application of this material are photocatalysis [66], the already mentioned dye sensitized solar cells, and its use as an additive to avoid UV induced degradation. TiO_2 crystallizes in three different lattice structures. The scientifically and technologically most important phases are rutile and anatase, both exhibiting the tetragonal crystal structure. Although rutile is the most common form, anatase can be efficiently grown in the form of nanoscale colloids. Dye sensitized solar cell make use of these anatase colloidal films exhibiting a sponge-like structure, covered with a monolayer of dye, and by that increasing the active surface by a factor of more than 1000. Since anatase was exclusively used throughout this work, the focus is put on its properties in the following. Anatase crystallizes according to the space group D_{4h}^{19} or $I4_1$/amd with the lattice constants of a=b=3.79 Å and c=9.54 Å [67], as shown in Fig. 11.

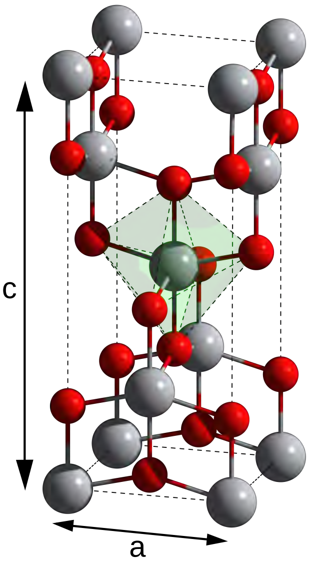

Fig. 2.10 Crystal structure of anatase. The conventional unit cell consists of slightly distorted octahedral symmetry. The big gray spheres represent Ti atoms and the small red spheres indicate O atoms. The lengths of the unit cell are indicated in the scheme (see text). The central [TiO_6] octahedron is emphasized in green.

Most important for the use in an electronic device is the band alignment of the valence (VB) and conduction band (CB) as well as the electron mobility. By means of absorption spectroscopy a rather large indirect band gap of about 3.2 eV was found for anatase [68].

Therefore, TiO_2 is in general classified as a wide band gap semiconductor and sensitization is needed to obtain sufficient absorption of the solar spectrum. The electron mobility in bulk anatase is $10\,\mathrm{cm}^2/(\mathrm{V\,s})$ [69]. However, this value can vary in nanoporous materials to a large extend [70].

Intrinsic defects play an important role. Oxygen vacancies form occupied defect states below the conduction band leading to an intrinsically n-type doping. The Fermi level position was found to be close to the conduction band [71]. As a consequence the conductivity can vary by orders of magnitudes [72].

For the electron transfer from the excited dye molecule donor orbital into the CB of TiO_2, the density of accessible states is of great importance. The conduction band of TiO_2 is formed from unoccupied 3d orbitals of Ti^{4+} [73]. The valence band edge is dominated by the 2p orbitals of Oxygen [74]. Further analysis of the electronic properties of TiO_2 is given in chapter 4.

Zinc Oxide

Zinc Oxide (ZnO) has been object of intense research since many decades [75,76]. During this period, the interest in this material has featured remarkable discontinuity. However, nowadays attention is focused on its prospects in optoelectronics applications as an efficient electron transport material. Considered as an electron acceptor in a dye sensitized solar cell, ZnO represents a promising alternative to TiO_2 due to its much higher bulk electron mobility [77,78] and great diversity in the nanostructured electrodes that can be easily produced. Some noteworthy examples are nanoparticles [79,80], nanorods [81] and nanosheets [82]. ZnO exists in two main crystalline forms, the wurtzite (as shown in Fig. 2.11) and the zinc blende structure, whereas the former is the most common and thermodynamic stable form. The space group of the hexagonal wurtzite structure is D^4_{6v} or $P6_3mc$, with the lattice constants a = 3.25 Å and c = 5.2 Å [75].

Crystallographic investigations indicate predominantly the presence of wurtzite structure in nano-powders [83]. For this crystal type a band gap of 3.2 eV was found [84], which is rather similar compared to TiO_2. ZnO in its wurtzite structure appears naturally as a n-type semiconductor because of a deviation from stoichiometry caused by the presence of intrinsic defects such as oxygen vacancies and zinc interstitials. However, it remains still controversial which type of intrinsic defects play the major role. Extrinsic n-type doping was found to be relatively easy compared to p-type doping. Usually group III elements like In, Ga and Al are used as substitutional elements for Zn and group VII element like Cl and I as a replacement for O, resulting in an n-type doping. P-type doping has only recently been achieved [85]. This renders the potential use of ZnO in bipolar devices, e.g. diodes, difficult.

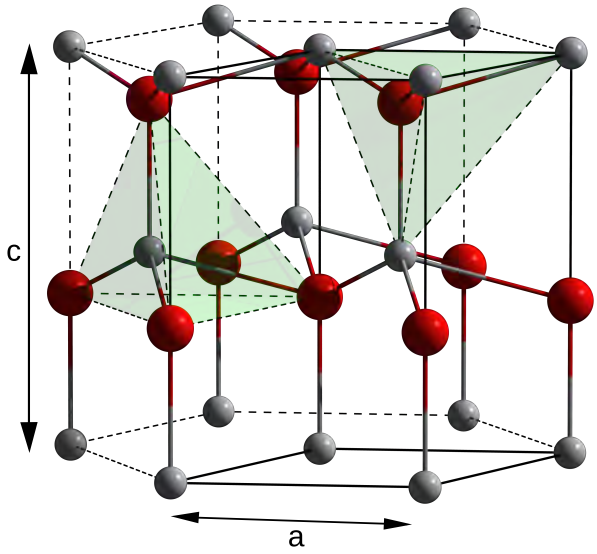

Fig. 2.11 Hexagonal unit cell of wurtzite ZnO. The small gray spheres represent Zn^{2+} atoms and the larger red spheres indicate O^{2-} atoms.

Ionic Liquids

Ionic liquids (ILs) are organic salts comprising melting points below 100 °C being in liquid phase already at room temperature (also called Room Temperature Ionic Liquids) [86–88]. ILs are mainly composed of inorganic anions and organic cations and exhibit in most cases relatively low viscosities. The definition allows to distinguish them from the classical molten salts with typically very high melting points e.g. NaCl (801 °C) and high viscosity.

Since the first report on a room-temperature IL, the ethylammonium nitrate, in 1914 by P. Walden [89], a large number of other ILs has been synthesized. ILs are typically made of bulky asymmetric organic cations, such as imidazolium, pyridinium, pyrrolidinium, quaternary ammonium, which exhibit weak intermolecular interactions, low charge densities and very low symmetry [90–93]. Due to the delocalization of the charge and steric effects, the formation of a regularly packed and stabile crystal lattice is hindered. Therefore a minor amount of thermal energy is already sufficient to break down the crystal structure, giving rise to the low melting points [94]. Due to their characteristic properties, ILs are often considered as future solvents for catalytic[95,96] and chemical reactions,[97] as well as for electrochemical purposes [98]. In DSSC, ILs have been investigated as solvents for electrolytes due to their non-volatility and high electrochemical stability in contrast to the so far used organic solvents [99–102]. In this work, the 1-Ethyl-3-methylimidazolium trifluoromethanesulfonate (obtained from Iolitec) was chosen as a solvent to investigate the charge dynamics in $[Ru(bpy)_3]^{2+}$. The chemical structure of this IL is shown in Fig. 2.12.

The solubility of different species in imidazolium ionic liquids depends mainly on the hydrogen bonding ability and on polarity. The $[Ru(bpy)_3]^{2+}$ complex was found to be soluble

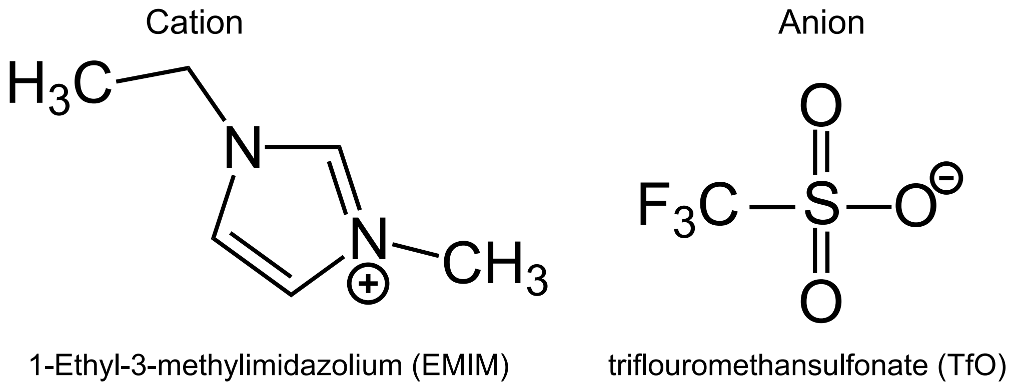

Fig. 2.12 Chemical structure of 1-Ethyl-3-methylimidazolium trifluoromethanesulfonate (EMIM TfO).

up to 100 mM whereas in the case of N3 and N719 much lower concentrations could be reached. For the investigation under UHV conditions, the vapor pressure is of particular importance. The extremely low vapor pressures for most of the ILs (10^{-10} Pa at 25 °C) make them perfectly suitable for any application as a solvent when a high-vacuum condition is required [103]. Simultaneously, they provide sufficient electric conductivity which is needed to recharge the sample in photoelectron spectroscopy experiments. Their general stability under UHV and with regard to XUV irradiation will be discussed in section 4.3.

2.3 Ultrafast Spectroscopy

Studies of the interaction of light with matter, based on spectroscopy, can yield a comprehensive microscopic view of nature. In its simplest implementation, the stationary approach, it is capable to reveal structural information [104]. However, to understand fundamental processes, time-resolved methodologies are required to examine how functionality is connected to molecular dynamics [36,105–109].

The function of physical, chemical, or biological systems is determined by processes that appear on an extremely short time scales between one femtosecond (10^{-15} s) and several picoseconds. Therefore, most of these experiments are implemented in a pump-probe configuration in which an ultrafast pump pulse triggers a reaction or, more generally, prepares a system in a non-stationary state. The evolution of this state is then monitored by means of a second probe pulse. Depending on the chosen probe scheme, the character and amount of information obtained therein varies considerably. The spectroscopic methods can be specified either by the used probe scheme or by the applied frequency range of the probe pulse.

Considering the studies on solid state samples, transient absorption spectroscopy in the visible and near IR range is often the method of choice. With this technique the relative changes in the absorbance with respect to the pump-probe time delay is recorded. Though, the actual transitions that involve population of excited states are probed indirectly, and it is difficult to draw conclusions about the energy structure in this case.

Another approach, time-resolved photoelectron spectroscopy, does not rely on this drawback. In these experiments, the probe pulse generates photoelectrons through ionization and the kinetic energy of the emitted electrons is measured as a function of pump-probe time delay [110,111]. Since the ionization transition is not restricted by the dipole selection rules, it is possible to monitor the electron density distribution among the ground and excited states. However, to be able to ionize the system in a single photon process the photon energy has to be sufficiently high. Recently developed coherent light sources of ultrashort pulse duration in the XUV and Soft X-Ray domain, such as laser-based high harmonic generation (HHG) [13,14] and accelerator-based free-electron-laser (FEL) [11,12] opened up new perspectives in this field.

In this section the fundamental aspects of ultrafast laser physics are discussed. It addresses the generation and characterization of coherent and intense laser pulses, followed by a general introduction to the field of high-order harmonic generation. In the last part of this section, the physical principle of photoelectron spectroscopy is described and its implementation in a pump-probe scheme is outlined. The practical realization is subsequently described in chapter 3.

2.3.1 Generation of Ultrashort Laser Pulses

Before discussing the theoretical aspects of high-order harmonic generation some introductory description about the physics of ultrashort pulses is given. It provides a basis for the subsequent discussion of laser frequency up-conversion and ultrafast spectroscopy.

Continuous monochromatic light is described in the time domain by a plane wave. The time representation is given by [112,113]

$$\mathrm{E}\left(\mathrm{z},t\right) = \mathrm{E}_0 e^{i(\mathrm{kz}-\omega_0 t)}, \tag{2.8}$$

were E_0 is the amplitude of the electric field, ω_0 is the angular frequency. Based on this plane wave representation, light pulses can be constructed by multiplying Eq. 2.8 with a bell-shaped envelope [114]. For simplicity a Gaussian envelope is chosen and its spatial propagation is omitted. The resulting Gaussian-shaped pulse can be written as

$$E\left(t\right) = E_0 e^{-\Gamma t^2 + i\omega_0 t} \tag{2.9}$$

The temporal evolution of Eq. 2.9 is shown in Fig. 2.13. Hereby Γ is called the shape factor of the Gaussian envelope and is dependent on the pulse duration, $\Gamma \propto {t_0}^{-2}$. The spectral components of the laser pulse can be obtained by a Fourier transformation. The general relationship between the time and frequency domains of a pulse reads:

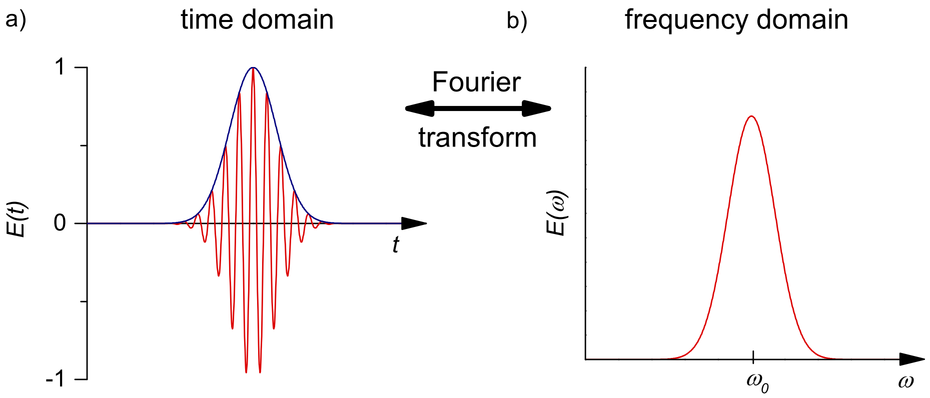

Fig. 2.13 Gaussian shaped laser pulse. In a) the time evolution of the electric field (red) is shown obtained by multiplying a cosine function with a Gaussian envelope function (blue). In b) the Fourier transform of the Gaussian pulse in the frequency domain is presented. The transformed function is also a Gaussian function centered around ω_0.

$$\begin{aligned} \varepsilon\left(t\right) &= \frac{1}{2\pi}\int_{-\infty}^{\infty} E\left(\omega\right)e^{-i\omega t}d\omega \\ E\left(\omega\right) &= \frac{1}{2\pi}\int_{-\infty}^{\infty} \varepsilon\left(t\right)e^{-i\omega t}dt \end{aligned} \tag{2.10}$$

The Fourier transform of a Gaussian shaped pulse in the time domain is also a Gaussian function in the frequency domain with a central frequency as illustrated in Fig. 2.13(b). The spectrum of the laser pulse can therefore be described by

$$E\left(\omega\right) = \exp\left[\frac{-(\omega-\omega_0)^2}{4\Gamma}\right] \tag{2.11}$$

For an arbitrary light pulse that can be defined by its general pulse duration Δt in the time domain and by $\Delta\omega$ in the frequency domain it can be shown that both quantities are related through the following universal inequality:

$$\Delta t\Delta w \geqslant \frac{1}{2} \tag{2.12}$$

This dependency can also be derived from the Heisenberg's uncertainty principle in energy and time, $\Delta E\Delta t \geqslant \hbar/2$. From this simple equations some very important facts for the physics of ultrashort pulses can be derived, which will be in the following shortly summarized [115]:

- In order to produce a light pulse with a given duration it is necessary to use a sufficiently broad spectral bandwidth.
- The value of 1/2 in Eq. 2.12 can only be reached by light pulses with Gaussian time and spectral envelopes.

- For non-Gaussian shaped pulses the right side of Eq. 2.12 appears to be larger than 1/2.
- For a given spectrum it exists one pulse envelope that exhibits the shortest possible duration in the time domain.
- Only for symmetrical spectra the shortest transform-limited pulses can be constructed.

2.3.2 High-harmonic Generation

The term High-harmonic generation (HHG) denotes the mechanism in which laser light is frequency up-converted to integer multiples of the fundamental frequency by means of a highly nonlinear interaction with a medium (e.g. noble gas). In this section the main principles will be described whereas more profound descriptions of HHG can be found in various reviews and book chapters [14,116–118].

First experiments on HHG were already reported between 1987 [119] and 1988 [120]. Since then many different types of lasers were applied to drive the HHG process, including short-wavelength excimer lasers,[121–123] dye lasers in the visible spectral range,[124,125] and IR-lasers [125,126]. Thereby it was found that the generation can cover a very broad spectral range of up to several hundred eV [119,127] and in some cases even thousand eV [128] can be reached. A typical intensity distribution of HHG light depending on the harmonic order n is illustrated in Fig. 2.14.

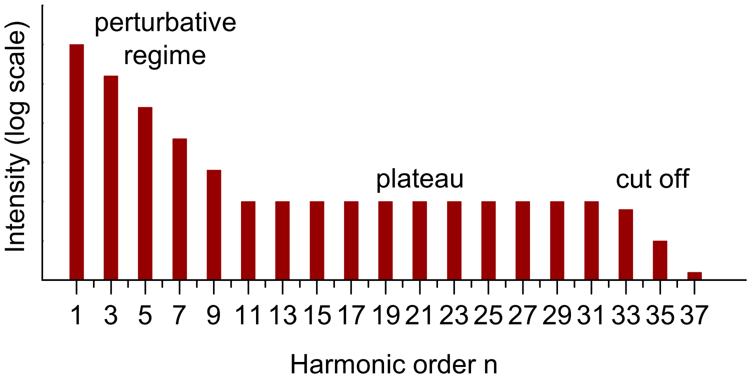

Fig. 2.14 Intensity distribution (logarithmic scale) of a typical spectrum obtained by high harmonic generation. For low harmonic order n, in the perturbative regime, the intensity is rapidly decreasing. For higher order, a plateau can be seen which is terminated by the cut-off, depicting the highest harmonics that are generated. Additionally, only odd harmonics of the fundamental frequency can be generated.

In the limit of small n, a very rapid decrease of the HHG yield with the increase of the harmonic order is visible, as one would expect by applying the perturbation theory to describe multi-photon transitions. The perturbation theory predicts that the transition probability decreases exponentially with n, in conjunction with the intensity of emitted photons (called the perturbative region of HHG spectrum). Subsequent to this spectral region, a plateau of equally intense harmonics can be found followed by a sharp decrease to zero. The presence of the plateau range could not be understood by a simple perturbative approach. Additionally, only odd harmonics of the fundamental frequency can be generated. To explain the large number of equally intense harmonic peaks, another theory had to be found to account for these results. In 1993 Corkum [129] and Kulander [130] presented a semi-classical theory, which reproduced the observed plateau behavior in the HHG spectra. This so called "three-step-model" was later confirmed by quantum mechanical calculations [131,132]. In the three-step model, the electron is initially treated quantum-mechanically as it undergoes tunnel ionization in the laser field, but then its subsequent dynamics are described classically.

The three-step model describes the HHG process by the following sequence of steps: (also illustrated in Fig. 2.15)

1. Tunnel ionization: If an atom is irradiated by a strong laser field it can be ionized. This leads to the formation of an ion (the parent ion) and a free electron with zero initial kinetic energy.
2. Acceleration: The electron is accelerated by the laser electric field. When the electric field changes its sign, the electron can be driven back to the parent ion.
3. Recombination: If the electron collides with the parent ion, the ion and electron can recombine and the excess energy is released in the form of photon.

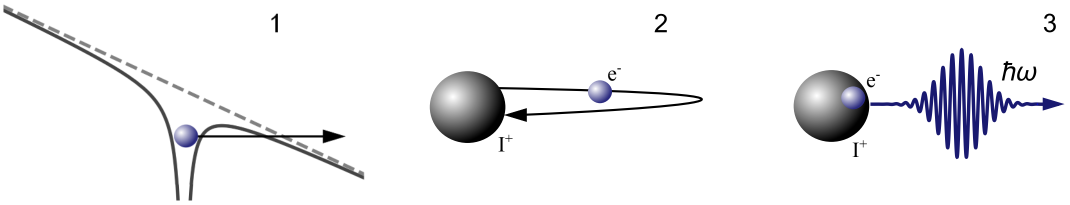

Fig. 2.15 Schematic of the three step model: (1) ionization, (2) acceleration by the laser electric field, (3) recombination via emission of a photon

Ionization

In the focus of ultrashort laser pulses, the strength of the external electric field can be comparable to the field strength experienced by the bound atomic electron in the vicinity of its parent atom. In this case, if laser intensities in the order of $10^{14}\,\mathrm{W/cm^2}$ are applied, a strongly non-perturbative regime is reached. The resulting potential experienced by the electron represents the superposition of two potentials:

$$V\left(\vec{r},t\right)=-\frac{e^2}{4\pi\varepsilon_0 r}+e\vec{E}\left(t\right)\vec{r} \tag{2.13}$$

where the first term describes the Coulomb interaction between the atomic core and the electron and the second term is the dipole potential induced by the external laser field. In Eq. 2.13, e denotes the elementary charge, ϵ_0 is the vacuum permittivity, and r is the distance between the electron and the atomic core. At sufficiently high laser field strength, the Coulomb potential becomes significantly distorted. This is illustrated in Fig. 2.16 which depicts the superposition potential (Eq. 2.13) for three different cases. The ionization potential remains unperturbed if the electric field strength is considerably low (see Fig. 2.16(a)). For sufficiently high laser frequency, multi-photon ionization can take place. In scenario b), the Coulomb potential is significantly modified leading to the formation of a finite barrier. The electron can tunnel through this barrier and, as a result, appears as a free particle with zero kinetic energy exposed to the external laser field. For very strong electric fields, the barrier is completely suppressed and the electron can directly leave the parent core (over-barrier ionization, see Fig. 2.16(c)).

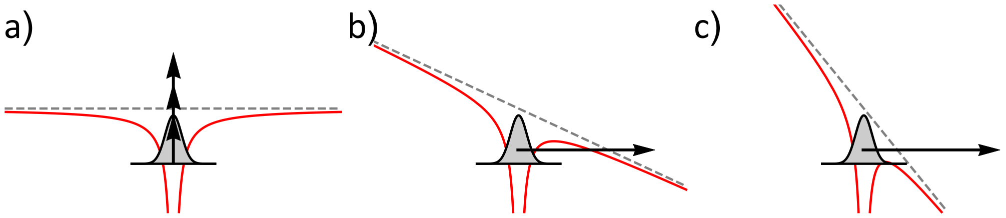

Fig. 2.16 The three different ionization scenarios. The ionization potential remains unperturbed if it is stronger than the external electric field, as shown in a). This leads to the absorption of multiple photons and multiphoton ionization being the dominant ionization mechanism. b) The external electric field strength is increased and the atomic potential is significantly modified. Ionization appears due to tunneling through the created barrier (tunnel ionization). c) For very large electric fields, the potential is strongly distorted and the electron can directly leave the parent core (over-barrier ionization).

The first theoretical description of the tunnel ionization was given by Keldysh [133] in 1965. In his work he introduced the very important parameter γ (called the Keldish adiabaticity parameter):

$$\gamma=\sqrt{\frac{I_p}{2U_p}} \tag{2.14}$$

where I_p is the ionization potential and U_p is the ponderomotive potential:

$$U_p=\frac{e^2E_0^2}{4m_e\omega^2} \tag{2.15}$$

which represents the cycle-averaged quiver energy of the electron in the oscillating electric field. The value of γ determines the ionization regime. For values larger than one ($\gamma > 1$) multi-photon ionization takes place, whereas values in the range or smaller than one ($\gamma \lessapprox 1$) determine the ionization regime. In the case where the Keldish parameter is much smaller than one ($\gamma \ll 1$) the third, over the barrier ionization [134], is present. The highest efficiency for high-harmonic generation is achieved in the tunneling regime, as it can be understood by considering the subsequent propagation step.

Electronic Motion in the Electric Field (Acceleration)

Following the tunnel ionization event, the electron can be approximately treated as a free charged particle exposed to the electric laser field $E(t) = E_0 \cos(\omega t + \varphi)$. The phase of the electric field denotes the moment (time zero) when the ionization takes place. The electron motion in the external ac-field is described classically. As initial conditions, one considers that the electron is released from the atom at position $x_0 = 0$ with an initial velocity of $v_0 = 0$. The velocity $v(t)$ and position $x(t)$ at time t can be calculated by:

$$v(t) = \int_0^t -\frac{e}{m_e} E(t')\, dt' = \frac{E_0 e}{m\omega} (\sin(\omega t + \varphi) - \sin(\varphi)) \tag{2.16}$$

$$x(t) = \int_0^t v(t')\, dt' = \frac{E_0 e}{m\omega} (\cos(\omega t + \varphi) - \cos(\varphi)) + \sin(\varphi) \cdot t \tag{2.17}$$

The velocity given by Eq. 2.16 exhibits a time-independent term called drift velocity. For a nonzero drift velocity the electron atom distance will continuously increase, superimposed to the oscillatory quiver motion caused by the field. The electron trajectories for certain phases φ are illustrated in Fig. 2.17. The amplitude of the oscillatory motion is referred to as the ponderomotive radius $a_0 = E_0 e / m\omega^2$ and is used as the unit for the electron-atom distance in this graph. Its value is in the order of some nanometers for typical laser intensities ($10^{14}\,\mathrm{W/cm^2}$) and by that is much larger than the atomic radius. For different phases of the electric field, the electron trajectories behave differently in time. As it can be seen in the enlarged view in Fig. 2.17(b), only trajectories with small phase φ return to the origin of the atom and can give rise to the electron recombination with the parent ion. The recombination is the key step in the generation of high harmonics and is discussed in the following.

Recombination

If the electron collides with the parent atom, the ion and electron can recombine, giving rise to the emission of a photon carrying the excess energy. The photons energy is given by:

$$\hbar\omega = I_p + E_{kin}, \tag{2.18}$$

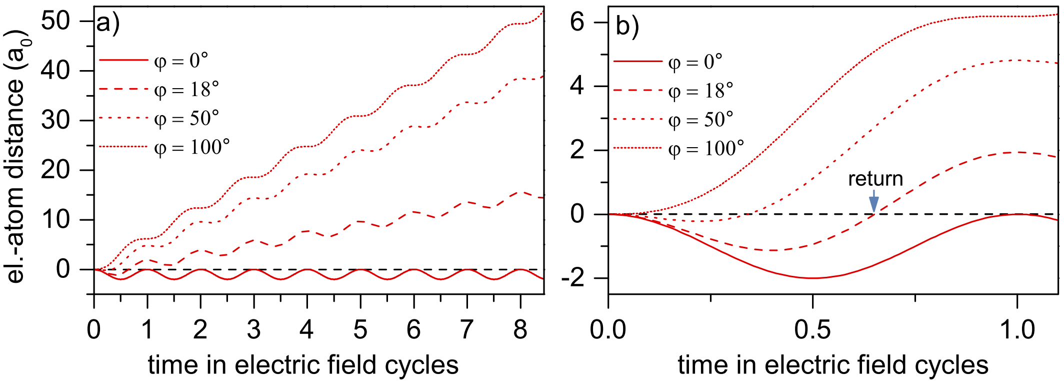

Fig. 2.17 Electron trajectories as a function of time for different phases. The vertical scale, representing the distance between the electron and the atom, is expressed in terms of the ponderomotive radius a_0. b) The enlarged view of a) for small times. Electrons ionized at different phases follow different trajectories. Only for certain phases the electron returns to the atom. The velocity of the electron at the zero crossing point is given by the absolute slope at that point.

where I_p is the ionization potential of the atom and E_{kin} the kinetic energy that the electron gains in the laser field. Depending on the phase of the electric field at the instant of the tunnel ionization event, the different trajectories lead to different kinetic energies at the moment of the electron return to the parent ion. This is illustrated by the different slopes at the trajectories intersection points with the $x = 0$ axis in Fig. 2.17(b). The highest photon energy that can be released in the process of high harmonic generation is thus connected to the maximum kinetic energy the electron can gain in the electric field. To this end, one needs to solve the Eq. 2.17 for $x(t) = 0$ and calculate the kinetic energy at that instant. The solution cannot be expressed in terms of elementary functions. However, it can be found numerically. The different kinetic energies for various phases φ are shown in Fig. 2.18.

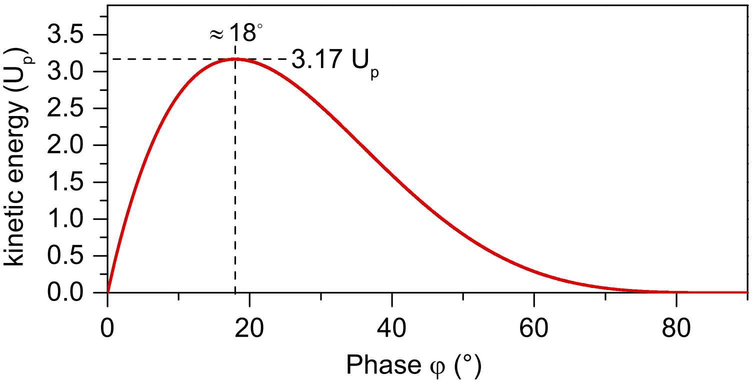

Fig. 2.18 Kinetic energy upon the electron return to the parent core as a function of the phase of the electric field, at which the ionization takes place. The maximum is achieved at approximately 18°. In this case, the kinetic energy upon return reaches 3.17 U_p.

Its maximum arises at a phase of 18° and a kinetic energy of 3.17 U_p. This value defines the cutoff energy in the high harmonic spectrum and is called the cutoff law:

$$\hbar\omega_{cut} = I_p + 3.17U_p \tag{2.19}$$

This theoretical finding was empirically proven in experiments and represents another example of justification of the validity of the three-step model. From Eq. 2.19 it can also be seen that in order to generate high energetic photons (large harmonic order n) a large ponderomotive potential is needed. This calls for applications of long laser wavelengths and high intensities, implying the tunneling regime of ionization in the first HHG step.

In general, after tunnel ionization different processes can take place. Beside the recombination with the parent atom leading to emission of high energetic photons, the electron can also be scattered on the residual core in the presence of the laser field, which can lead to the increase in the electron kinetic energy. This multiphoton effect is denoted by high-order above-threshold ionization (HATI) [135,136] and represents a competing reaction mechanism to the HHG.

Summary on high harmonic generation:

- High photon energies can be reached if U_p is large. This requires application of high laser intensities and low frequencies.
- The high harmonic generation strongly depends on the phase of the electric field. Therefore, the harmonics are coherent to the fundamental laser field.
- The high harmonics generation is repeated every half period T/2 of the laser frequency. The Fourier transform of this signal consist therefore of peaks separated by 2ω, meaning that only odd harmonics of the fundamental frequency can be generated.

2.3.3 Time-resolved Photoelectron Spectroscopy

In general, photoelectron spectroscopy (PES) refers to the measurement of the kinetic energy of electrons after their emission from solid, liquids or gases due to the photoelectric effect. From the kinetic energy spectrum and the used photon energy, conclusions about the binding energy of the electronic state from which the electron was removed can be drawn. If these states are core states the method also exhibits element-specific information and is called ESCA (electron spectroscopy for chemical analysis). Depending on the used light source it can be distinguished between ultraviolet (UPS, <100eV) and x-ray photoelectron spectroscopy (XPS, >100eV). Because of the limited photon energy range, UPS is restricted to accessing the valence states, while XPS can also probe deeper lying core states. In this section the main principles of transient PES will be describes, whereas a much deeper consideration and applications of this method can be found in numerous text books on photoelectron spectroscopy [137–139]. The basic principle of photoelectron spectroscopy is depicted in Fig. 2.19. The incoming photon is absorbed by an electron, which is then transferred from its initial state into an excited state. For sufficiently high photon energy the electron is ejected into vacuum and can be considered as a free moving particle. The binding energy of the electron in the sample can be determined from the following equation:

$$E_{kin} = \hbar\omega - E_b - \Phi_s, \tag{2.20}$$

where Φ_s denotes the samples work function. In solids the binding energy is generally referred to the Fermi level, whereas in free atoms or molecules in most cases the vacuum level is used as a reference. Electronic states, measured in a solid, that lie below the Fermi level (occupied states) are usually characterized by their positive binding energies.

In order to measure the kinetic energy of the electrons, the sample has to be in contact to the analyzer, where they are counted. This leads to a contact potential that, depending on the sign, accelerates or decelerates the electron into the detector. For this reason the kinetic energy of the electron are intrinsically measured against the work function of the analyzer. An initial calibration of the binding energy scale is done by measuring the Fermi edge of a metal sample (e.g. gold) and set this value to zero binding energy ($E_b = 0$). Further, it has to be noted that the escape depth of electrons is only a few nm, depending on their kinetic energy. The short mean free path of electrons is given by the strong interaction with dense matter. For the kinetic energies considered in this work, the universal curve of the mean free path [140] possesses a minimum of approximately one nm. In this case PES probes only the first few monolayers at the surface of the investigated sample.

The time resolution is achieved by introducing another so called pump pulse and by delaying the pump and probe pulses against each other. Such measurements are referred to as pump-probe measurements, where the pump pulse populates an intermediate state and a delayed probe pulse detects the population as a function of time. This process is illustrated in Fig. 2.19(b). The optical pulses can have different wavelengths. In this thesis the pump photon energy is chosen to be in the visible range to excite well-defined optical transitions in the sample. The photon energy of the applied pump pulse does not exceed the work function and, therefore, no electrons are emitted. Contrary, the probe pulse is in the XUV range give rise to a high probability of single photon ionization. This leads to a stationary photoelectron background independent of the time delay between pump and probe (steady state spectrum).The total spectrum consists of the background signal and a time dependent part (transient signal). Therefore an appropriate background subtraction is needed to separate both contributions. This can be done by using spectra recorded without applying the pump pulse.

A detailed description of the experimental procedure, including the generation of the pump and probe pulses as well as a characterization of the spectrometer, is given in the next chapter.

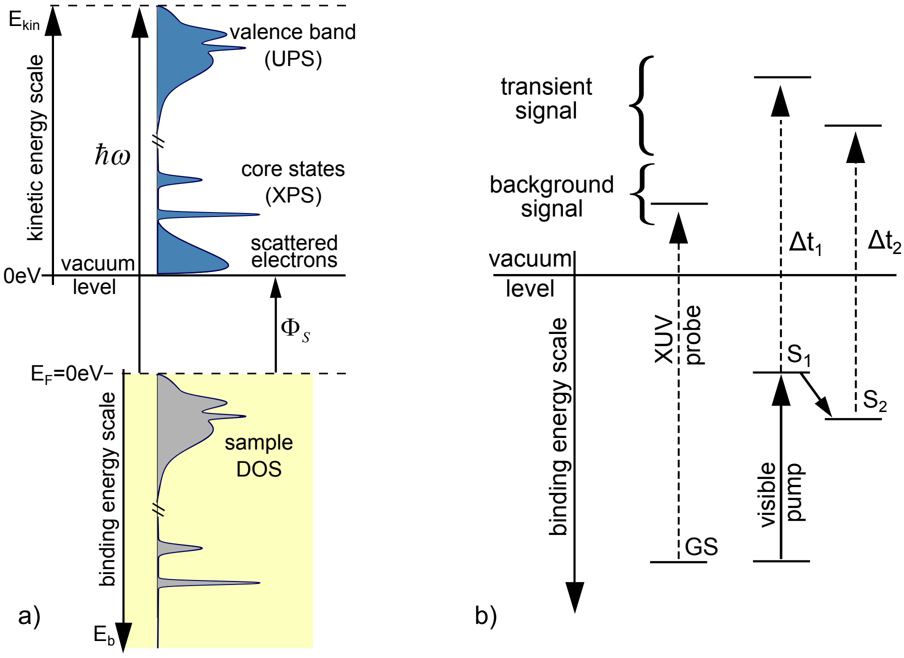

Fig. 2.19 Energetic scheme of a photoelectron spectroscopy experiment. In a) the general principle of the PES is explained on a metallic sample. The chemical potential is indicated by the dashed horizontal line. The vacuum level, i.e. the zero kinetic energy of unbound electrons, is denoted by the thick horizontal line. The difference between the vacuum levels and the Fermi edge is given by the work function Φ_s of the sample. By means of different photon energies, the core as well as the valence band states can be addressed separately. In b) the pump-probe principle is illustrated. The high energetic XUV photons lead to a single photon emission channel, giving rise to a stationary background signal. The evolution of the intermediate states (denoted by S1 and S2) can be investigated by applying different pump-probe delay times Δt.

Chapter 3

Experimental Set-up

Time resolved photoelectron spectroscopy was exclusively used throughout all investigations presented in this thesis. This chapter deals with the practical implementation explaining in detail the design and characteristics of the system. Further information is provided in our recent publication about the time resolved photoelectron spectrometer [141]. A schematic overview of the experimental setup is shown in Fig. 3.1. It consists of different parts, including a commercial available femtosecond Ti:sapphire laser. The laser output is split into two beams and a certain fraction of the infrared pulse energy is used to pump the HHG. The other split beam is used to pump an optical parametrical amplifier (OPA) generating the pump pulses in the visible spectral range.

The central part of the setup is dedicated to the generation of high harmonics, their spectral separation and characterization. Subsequently, the pump and probe pulses are overlapped and focused onto the sample. The emitted electrons are detected in a time-of-flight spectrometer (TOF) which measures their kinetic energy via recording the flight time. Both the HHG part and the TOF spectrometer part require UHV conditions because XUV photons and electrons can be easily attenuated in a gas medium. In the following, each part is described in detail.

3.1 The Laser System

The fs laser is based on a commercial available Ti:sapphire amplifier system (Fig. 3.2). The oscillator (COHERENT Vitara) is pumped by a solid state laser (Optically Pumped Semiconductor Laser, OPSL, Verdi – G5) delivering 5 W cw power. The oscillator operates at 80 MHz and delivers pulses with approximately 10 nJ pulse energy and a central wavelength of 800 nm. The pulses are amplified by means of chirped pulse amplification (CPA) in a typical stretcher/amplifier/compressor configuration. The regenerative amplifier (COHERENT, Legend Elite Duo) is thereby pumped by a Nd:YLF pulsed laser (COHERENT, Evolution) with an output power of 75 W. After recompression, the pulses exhibit approximately 2.5 mJ

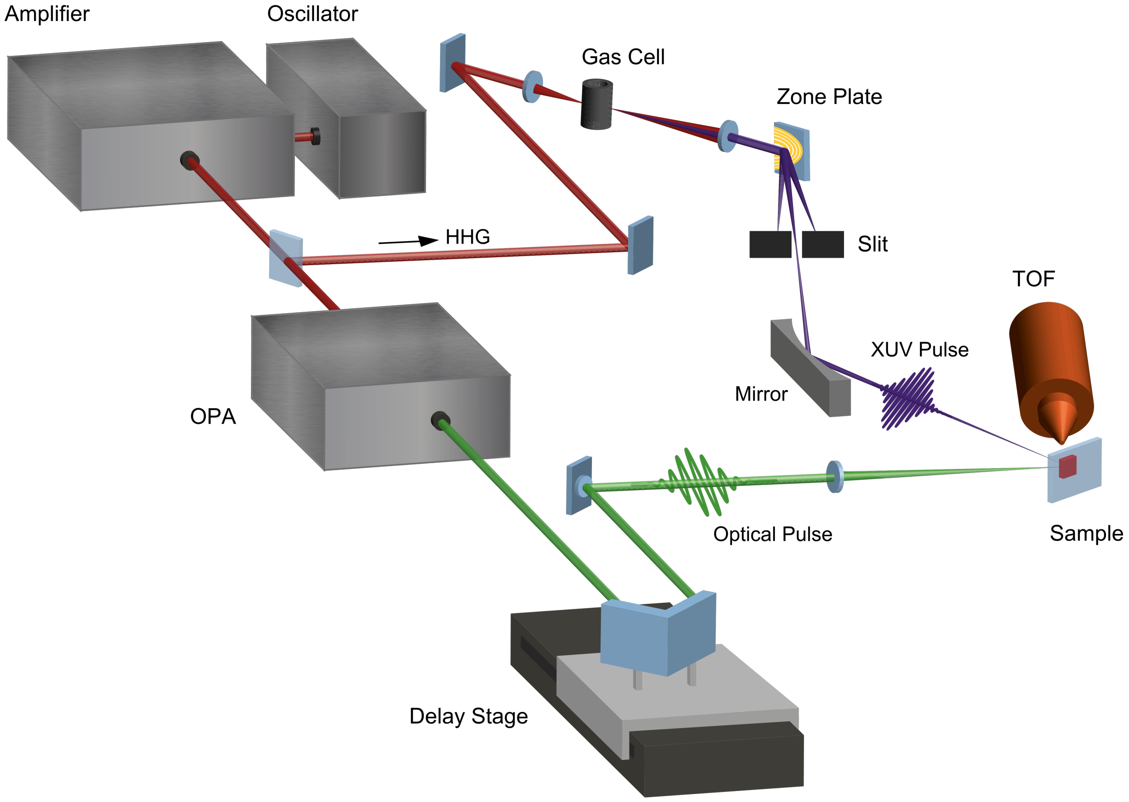

Fig. 3.1 Schematic overview of the experimental setup. The output of the commercial Ti:sapphire laser is split into two parts. One part is dedicated to the generation and monochromatization of the XUV probe beam whereas another part is used to pump an optical parametrical amplifier (OPA) generating the pump pulses in the visible spectral range. Afterwards both beams are overlapped onto the sample. The emitted photoelectrons are measured by means of a time-of-flight spectrometer (TOF).

pulse energy and a pulse duration of 25 fs (FWHM). The amplifier system operates at a repetition rate of 5 kHz. Laser pulses are split into two beams by a beam splitter (BS) so that pulse energy of up to 1.5 mJ is available to pump the HHG process. The other split beam is used for pumping the optical parametric amplifier (OPA). The OPA enables the tune the output wavelength in a range from 240 to 2600 nm.

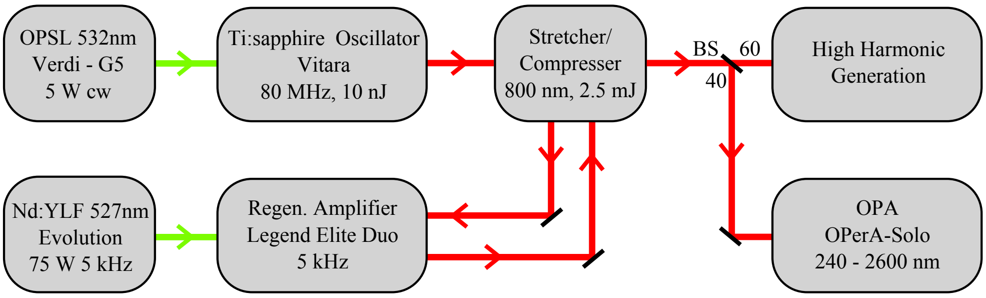

Fig. 3.2 Schematic view of the fs laser system. Detailed description is provided in the text.

Optical Parametrical Amplifier (OPA)

The application of parametric amplifiers is particularly favorable for the generation of wavelengths which are difficult to access directly with lasers due to the lack of suitable gain media. Additionally, they are beneficial if a large tuning range or high gains on short length scales are required. In the first part of this section the process itself is explained, followed by a description of the used OPA (COHERENT, OPerA-Solo).

Parametric amplification is based on the use of nonlinear optical crystals exhibiting a large nonlinear susceptibility of second order $\chi^{(2)}$ [142]. Typically used materials are BBO (β-barium borate), LBO (lithium triborate) or KTP (Potassium titanyl phosphate). Due to parametric effects in the medium, a single photon can be split into two photons or vice versa. This process is illustrated in Fig. 3.3. The three involved photons obey energy and momentum conservation. Depending on whether the pump frequency is smaller or larger than the signal frequency and whether the pump, the signal or both photons are annihilated creating a new photon, four different cases can be distinguished. Here we concentrate exclusively on the scenario where parametric amplification, also called difference frequency generation, takes place. In this case one pump photon with frequency ω_2 is annihilated via the creation of a signal photon with frequency ω_1 and an idler photon with frequency ω_3. Energy and momentum conservation implies the two equalities:

$$\omega_3 = \omega_2 - \omega_1 \tag{3.1}$$

$$\vec{k}_3 = \vec{k}_2 - \vec{k}_1 \tag{3.2}$$

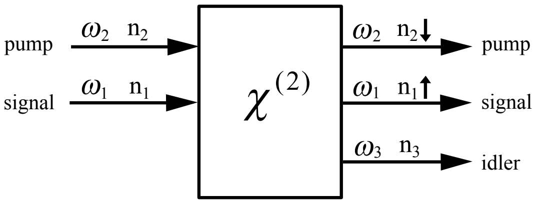

Fig. 3.3 The parametric effect is induced by the second-order susceptibility of a nonlinear material, in which one photon is split into two photons as shown in this case.

This means that the signal and idler beams are amplified, and the pump intensity decreases. This type of amplification should not be confused with the amplification taking place in a laser medium by stimulated emission. In the latter case an inverted electronic population is necessary, which is not the case for the OPA.

The frequencies of both signal and idler photons are determined by the phase-matching condition [143]. It can be varied e.g. by changing the temperature or the angle between the incident pump beam and the optical axis of the crystal. An adjustment of the frequency of signal and idler photons can, therefore, be achieved by rotating the nonlinear crystal.

The OPerA Solo

The OPA “OPerA Solo” from COHERENT is used to cover a broad spectral range of pump frequencies. It is pumped by the fundamental laser output with a wavelength of 800 nm and pulse energy of approximately 1 mJ. It includes a white-light continuum generation stage and two stages of parametric amplification. In the following the individual steps are explained. At first, a considerably small fraction of the pump beam (about 1-3 µJ) is used to generate a white light continuum (WLC) in a sapphire plate. The spectral broadening of the pump light is mainly caused by self-phase modulation [144]. A detailed description of this non-linear process is not provided in the scope of the thesis but can be found elsewhere [145,146]. Subsequently another small fraction of the pump beam (30-70 µJ) and the WLC are focused non-collinearly into the first preamplifier crystal, where parametric amplification takes place. By changing the delay of the WLC with respect to the pump pulse, a different signal wavelength can be chosen (called “Delay 1”). Additionally the crystal angle has to be adjusted to achieve the phase matching condition (and, thus, efficient amplification) for the specific signal wavelength chosen by Delay 1. By doing so, the signal can be tuned in the wavelength range between 1100 and 1600 nm. The non-collinear geometry enables to easily separate the amplified signal beam from the residual pump and idler beams, which are both blocked after the crystal. Afterwards the signal beam is expanded and collimated by a lens telescope, and guided into the second amplification stage.

The main amplification stage is pumped by the main part of the input pump beam. The pump and signal beams are overlapped collinearly in the second nonlinear crystal. Due to the parametric amplification in the crystal, the signal pulse is amplified of up to several hundreds of µJ and in addition the idler wave is generated. For efficient conversion, it is necessary to adjust the time delay between the signal and the pump beam as well as to tune the crystal angle for optimum phase matching condition. After the crystal, the signal and the idler beam are separated by a dichroic mirror. Depending on the wavelength range needed for experiment, different subsequent configurations in a third stage can be used. The simplest application of the OPA is to use directly the signal (1100nm - 1600 nm) or idler (1600 – 2600 nm) output. In addition, both beams can be used for second harmonic generation, leading in the case of the signal to a tuning range from 600 nm to 800 nm and in the case of the idler to a range from 800 nm to 1050 nm. It is also possible to mix the signal or idler beam with a portion of the fundamental pump beam to induce the process of sum frequency generation in an additional non-linear crystal. The sum frequency generation of the signal, mainly used in this thesis, covers the range between 475 nm to 540 nm. In this mode, pulse energies of up to 200 µJ can be achieved. Most of the tuning parameters are motorized and can be controlled by the “WinTOPAS” software. For each wavelength, a set of parameters is stored in a calibration file. This allows in general an easy and fast change of the OPAs output wavelength.

Auto- and Crosscorrelation

In general, a direct temporal characterization of femtosecond laser pulses by means of electronics (e.g. with a photodiode) is not feasible. Even nowadays the fastest response of only up to several tens of ps can be achieved with photodetectors. To overcome this limitation correlation techniques are widely used. To measure the temporal width of a pulse, the (second-order) intensity-autocorrelation is applied employing either a two-photon absorption step in e.g. a semiconductor or, alternatively, a $\chi^{(2)}$ process in a phase-matched doubling crystal. In the latter method the incident laser pulse is split into two pulses by a beam-splitter and a time delay Δt between the two pulses is introduced. Subsequently both pulses are focused into a frequency-doubling crystal and the resulting second harmonic generation auto-correlation trace is measured by a detector as a function of the time delay. If the intensity of the complex electric field corresponds to $I\left(t\right) = \left|E\left(t\right)\right|^2$, the autocorrelation function is defined by:

$$I_{AC}\left(\tau\right) = \int_{-\infty}^{+\infty} I\left(t\right) I\left(t-\tau\right) dt \tag{3.3}$$

Note that the auto-correlation is always a symmetric function that does not contain any information about the shape of the pulse. To determine the pulse duration a certain pulse shape has to be assumed. For different pulse shapes the relation between the FWHM of the auto-correlation trace and the pulse itself can be calculated. In case of a Gaussian shaped pulse this is given by $\tau_{AC} = \sqrt{2} \cdot \Delta t_{pulse}$. Special care must be taken for spectrally broad and in this context ultra-short pulses. Due to the limited spectral acceptance of the used non-linear crystals the spectra might be only partially frequency mixed. In this case the autocorrelation becomes too narrow and overestimates the real pulse duration [147]. Usually auto-correlation that employs two-photon absorption in semiconductor diodes does not suffer as much from this disadvantage.

The intensity auto-correlation does not allow to draw any conclusion about the phase of the spectral components of the pulse. To obtain this information more sophisticated methods like the Spectral phase interferometry for direct electric-field reconstruction (SPIDER) have to be used.

If the femtosecond pulse is not correlated with itself but rather with another different pulse instead, the cross correlation between both is measured. It requires that the shape of one of the pulses is known (called reference pulse) and from the cross-correlation trace the shape of another pulse can be reconstructed. If both pulses exhibit a large difference in their pulse duration, the cross-correlation width is mainly given by the longer one. This implies that to measure an unknown pulse a sufficiently short reference pulse, at least of the same order of pulse duration, has to be available. Another complication arises if the pulse duration in the XUV range has to be determined. In this case frequency mixing in nonlinear crystals is not applicable. Here, a multiphoton ionization process that involves absorption of an XUV probe photon simultaneously with absorption or emission of one or more pump photons is used. A detailed description is given in the subsequent section.

3.2 High-harmonic Beamline and the RZP Monochromator

This section is based on publication (6) from Optics Express, 2014, 22 (9) pp. 10747-10760

Since HHG is a highly nonlinear process, it is very sensitive to a number of different parameters. These are divided into the laser parameter given by the wavelength, the pulse energy, the pulse duration, as well as by the beam profile. Further, the focusing geometry, the interaction length and the gas pressure in the cell are of high importance. Finally, the type of gas used as the non-linear medium influences the achieved maximum XUV flux and photon energy. In the following the most relevant aspects for the HHG are elucidated.

The layout of the high harmonic beam-line can be seen in Fig. 3.4. It is completely implemented in a UHV framework. The HHG process takes place in an argon-filled gas cell in the first vacuum chamber. The cell is mounted at the end of a straight tube, which serves as the gas feed-through into the vacuum. The cell position is fixed by an intake at the bottom of the chamber. The laser is focused by a lens of 600 mm focal length into the gas cell. A $\lambda/2$ wave plate and a polarizer were used to control the intensity and polarization axis of the pump beam. In order to adjust the focus position relatively to the gas cell, the lens is mounted onto a translation stage. The gas cell is initially sealed with an aluminum foil into which the first laser shot drills apertures at the entrance and exit due to the high intensity in the focus. This procedure ensures a perfect alignment of the laser beam to the holes and that only the minimum of the needed aperture size is obtained. The argon pressure in the gas cell is adjusted by a dosing valve and typically applied pressures under operation are in the order of several tens of mbar. This results in a base pressure of approximately 10^{-3} mbar in the HHG chamber. To maintain UHV conditions in the subsequent part of the beamline, the design makes use of extensive differential pumping.

Gas cells of several different lengths were manufactured to test the HHG performance. It was found, that the cell of 16 mm length exhibits the highest efficiency in terms of XUV flux of the desired harmonic and yields smaller spectral bandwidth of XUV light. Further, it is well known that the focus position influences the HHG efficiency through the Gouy phase [148] as well as the pump pulse intensity and the gas pressure. These three parameter are highly correlated. The best results were achieved with a focus position directly behind the gas cell (in the beam propagation direction), with a pulse energy of 1 mJ, and with a gas pressure of 20 mbar. It is also noteworthy that the pump beam profile plays an important role. Particularly, any form of astigmatism in the focus significantly reduces the HHG efficiency. A beam profiler is used to ensure the best possible HHG pump beam quality. The above mentioned parameters have to be optimized on a daily basis.

After the HHG and the differential pumping stage, the desired harmonic is selected by a monochromator assembly. Its design and practical implementation is given in the following.

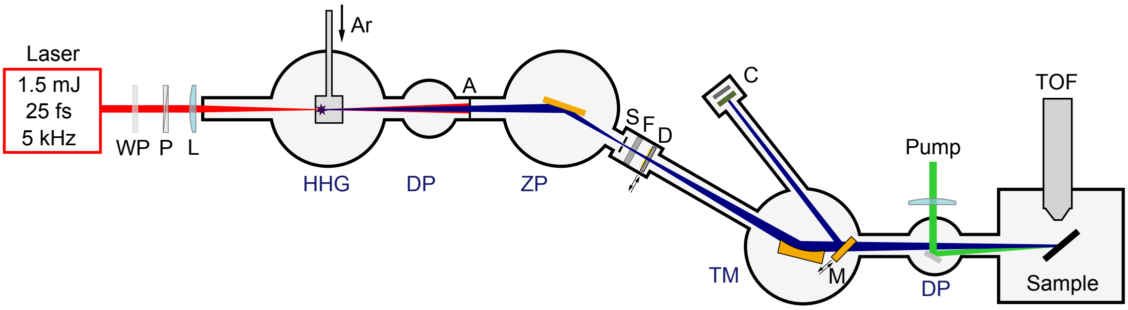

Fig. 3.4 Schematic view of the experimental setup. Notations: (WP) wave plate, (P) polarizer, (L) lens, (HHG) High harmonic generation chamber, (DP) differential pumping stage, (A) aperture, (ZP) zone plate chamber, (S) slit, (F) Al foil, (D) movable photodiode, (TM) toroidal mirror chamber, (M) movable plane mirror, (C) position-sensitive detector, (TOF) time-of-flight electron spectrometer.

The Reflective Zone-plate Monochromator

To be able to conduct photoelectron spectroscopy, a single harmonic of desired photon energy has to be selected from the HHG spectrum. A number of different approaches are available that need to be benchmarked with regard to two important challenges. To obtain sufficient energy resolution, the use of dispersive optics introduces inherently a temporal broadening of the pulse. It is a result of the path length difference caused by diffraction at the grating and can easily reach several hundred femtoseconds or even a picosecond depending on the number of grooves that are illuminated and the wavelength of light that is used. This represents a dramatic value that renders any time resolved approach in the fs regime obsolete. The time dispersion can be compensated by the use of a second grating [149–151]. The so called time delay compensating monochromator enables to compress the XUV pulse duration down to ten fs or even below [152,153]. However, in such a set-up, where the two gratings are additionally complemented by two mirrors for focusing and collimation purposes, a significant loss in transmission efficiency is unavoidable. Furthermore, the large number of optical elements makes the design and handling of the beam path complicated. This means that besides the temporal broadening the total transmission efficiency represents the second important attribute for a monochromator. Another approach is the use of narrow-band multilayer mirrors [154] to select a single harmonic. While a time resolution in the order of 100 fs could be achieved with the use of multilayer mirrors, the disadvantage of this method consists in the poor spectral selection of harmonics.

In the present set-up, off-axis reflection zone plates (RZP) were used for the purpose of monochromatization. Similar to a toroidal grating, an off-axis RZP diffracts different spectral components of the incident beam at different angles and focuses them into spatially separated spots.

The monochromator in the present set-up was designed to select the 17th, 21st and 25th harmonic, covering an energy range between 26 and 39 eV. For this purpose three different RZP were fabricated on a single silicon substrate with 50 mm diameter by e-beam lithography and reactive ion etching. In Figure 3.5, an image of the schematic view as well as the practical implementation is presented. To adjust the monochromator for selection of the desired wavelength, the substrate has to be moved along the y-axis depicted in Fig. 3.5(b) to position the optical axis of the corresponding RZP into the incident beam.

In general, a RZP makes use of the same concept as a classical Fresnel zone plate, with two distinct differences. Contrary to transmission mode of a classical Fresnel zone plate the RZP works in reflection mode and additionally its zone structure is not concentrically arranged. This leads to a dispersive character, combining properties of a grating and the focusing ability of a Fresnel lens in one single element.

The simplified optical layout of the RZP monochromator is shown in Fig. 3.6. The RZP, as shown in Figure 3.5(a), is used in an off-axis geometry meaning that the working area is located outside of the optical axes. This gives rise to two main advantages: (1) The specular reflex (zero-order reflection) is directed out of the optical axis and can be easily separated from the dispersed part. (2) Due to the high off-center mean line density, high dispersion is provided and a slit in the plane perpendicular to the optical axis can be installed for the energy selection.

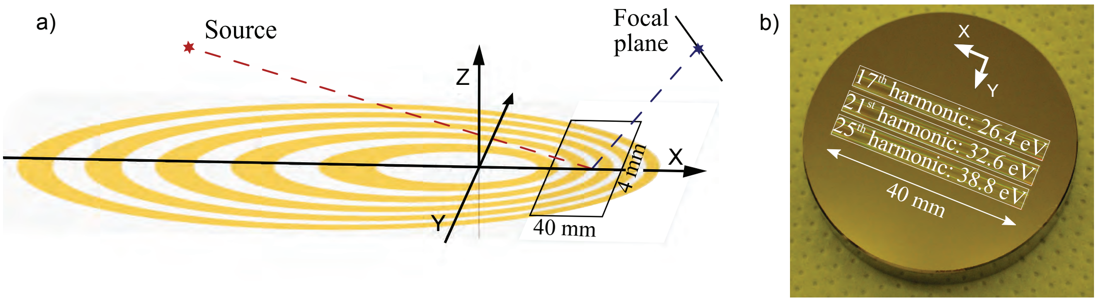

Fig. 3.5 Image of the RZP. In a) a schematic view of the Fresnel lens is illustrated. The RZP is used in off-axis geometry meaning that the illuminated part is outside of the optical axis. In b) a picture of the gold coated silicon substrate is shown. The three manifactured RZP on top are indicated by the inscription.

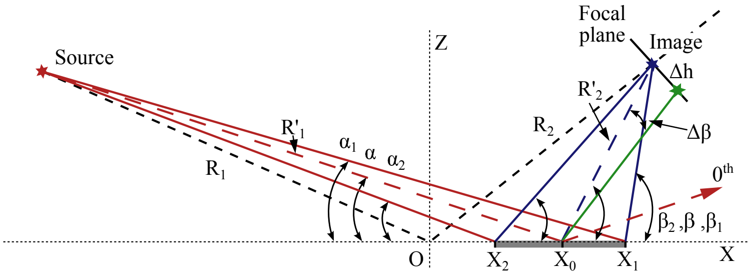

Fig. 3.6 Optical layout of the RZP. The area of use between X2 and X1 is indicated by the gray horizontal line. The meaning of notations is given in the text.

Is has to be noted that each single RZP monochromator is designed for a certain wavelength λ_0 and a focal length $F(\lambda_0)$. For any other wavelength the focal distance will be linearly dependent and all other energies will be unfocussed in the focal plane.

Using the common grating equation the spatial linear dispersion in the plane perpendicular to the optical axis can be calculated by:

$$n\lambda = d\left(\cos(\alpha) - \cos(\beta)\right) \tag{3.4}$$

where n is the diffraction order, d is the local line period in the middle of the illuminated area, α the incident angle and β the diffraction angle. Based on the grating equation, the angular dispersion in the middle of the working area can be derived as:

$$\Delta\beta = \frac{\Delta\lambda}{d\sin(\beta)} \tag{3.5}$$

where $\Delta\lambda$ represents the spectral bandwidth. By defining a slit size Δh this equation can be used to calculate the energy resolution given by:

$$\frac{\lambda}{\Delta\lambda} = \frac{R'_2\lambda}{\Delta h \cdot d \cdot \sin(\beta)}\ , \text{ if } \Delta h \geqslant \Delta S\frac{R'_2}{R'_1} \tag{3.6}$$

where ΔS denotes the source size, R_1' and R_2' represent the source-grating and grating focus distance, respectively. In the last equation the role of the geometrical magnification factor $M = R'_2/R'_1$ is indicated, which limits the minimum size of the slit width. According to Eq. 3.6 the energy resolution of the RZP monochromator can be varied by the values β, d and the slit size Δh.

By combining Eq. 3.4 and 3.6 one can calculate the local grating period for the first diffraction order which has the form:

$$d = \frac{\lambda}{\sin(\alpha)}\left[\sqrt{1 + \cot^2(\alpha) + \left(\frac{R'_2}{\Delta h}\frac{\Delta\lambda}{\lambda}\right)^2} - \cot(\alpha)\right] \tag{3.7}$$

The RZP sections were manufactured with a length of 40 mm (length in X-direction, X1-X2=40mm) and a height of 4 mm (Y - direction). The used geometrical parameters and the chosen energy resolution of the RZP monochromator in the center of each RZP are summarized in Table 3.1.

Table 3.1 The energy resolution and the geometrical parameters of the RZP monochromator.

$E/\Delta E$	$\alpha°$	$\beta°$	R_1' (mm)	R_2' (mm)	M
167	9.6	10.4	1000	350	0.35

If one assumes a HHG source size of 100 µm, the geometrical demagnification factor leads to a maximum slit size of 35 µm in the focal plane. The meridional line periods d in the center of each RZP were determined for the three different photon energies by using Eq. 3.7 and are given in Table 3.2:

Table 3.2 Meridional structure period d for the three manufactured RZP.

Harmonic	E (eV)	d (µm)
17	161.5	18.2
21	130.7	14.7
25	109.8	12.4

From the spectral resolving power of the RZP monochromator of $\lambda/\Delta\lambda = 167$ the temporal broadening of the incident pulse can be estimated by $\Delta t = \lambda^2/\Delta\lambda c$. For the photon energy of the 21st harmonic this yields a value of $\Delta t \simeq 21 fs$.

In the following the performance characteristics of the monochromator will be described. Results are presented mainly with regard to the RZP designed for the 21st harmonic. However, the performance characteristics of the two others RZPs were found to be similar.

Spatial intensity distribution

To characterize the dispersive performance of the RZP monochromator, the exit slit in the focal plane was exchanged by a position sensitive XUV detector. An image of the intensity distribution of the XUV radiation, obtained with the use the RZP designed for the 21st harmonic, is shown in Fig. 3.7.

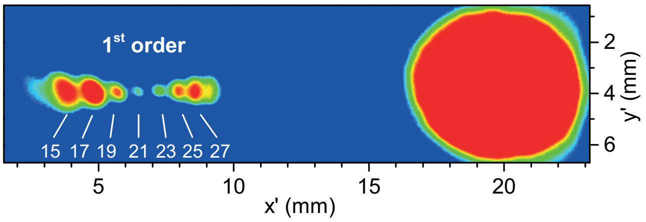

Fig. 3.7 Intensity distribution of XUV light in the slit plane. The image was recorded with the use of the RZP designed for selection of the 21st harmonic. The spots on the left hand side denote the first diffraction order and the individual spots are labelled according to their harmonic order. The large spot on the right hand side depicts the specular reflex.

On the left hand side of the image, the first diffraction order can be seen, which comprises a sequence of spots labeled according to their harmonic order. The clear separation of the individual spots demonstrates the high dispersive performance of the RZP. Furthermore they appear with different spot sizes, originating from the fact that only the desired wavelength is focused in this plane. Therefore, the smallest spot in the center arises from the 21st harmonic, whereas the foci of all other harmonics lie either before or behind the detector plane leading to larger spots in the image. As described before, the use of a slit with a proper width can easily block all unwanted contributions from neighboring harmonics. It is important to note that the relative intensities between the different harmonics are not correctly reproduced. The reason can be found in saturation effects of the detector (MCP - fluorescence screen stack) caused by the high XUV photon flux density of the tightly focused central harmonic. This further prevents a reliable determination of the real focus size by this method, which was obtained by another procedure. In this case the spot size is not measured in the slit plane but rather in the experimental chamber, where a 1:1 imaging by means of a toroidal mirror is accomplished. By using the razor-blade method, the beam diameter was measured at different positions along the propagation direction yielding a focus size of approximately 80 µm. Since no magnification is involved due to the refocusing, the monochromatized XUV beam is expected to have approximately the same size in the slit plane of the monochromator.

Spectral Characteristics of the Selected Harmonics

The spectral bandwidth of the XUV pulses is measured by means of XUV photoelectron spectroscopy of argon gas. The 3p ground state of argon exhibits a binding energy of 15.76 eV, associated with the formation of the Ar^+ ion in the $^2\mathrm{P}_{3/2}$ state, and the binding energy of 15.94 eV that corresponds to the formation of the $^2\mathrm{P}_{1/2}$ state. The XUV light was focused in the experimental chamber in front of the skimmer of the TOF spectrometer. The characterization shown in this section has been conducted with the commercial available time-of-flight spectrometer (TOF) (SPECS, Themis 600) equipped with electrostatic lenses. In this investigation, the electrostatic lenses were disabled and the spectrometer performed as a classical drift tube with an acceptance angle of $\pm 1°$. The spectrometer represents an essential part of the experimental setup and its principles of operation will be presented in more detailed in the next section. During the experiments, the argon pressure was maintained at 8×10^{-4} mbar in the experimental chamber.

Figure 3.8 shows the photoelectron spectra obtained with the use of the RZP designed for the 21st harmonic. Special care was taken to verify that the recorded spectra did not suffer from charging effects of the ionized sample. This was achieved by validating the proportionality between the total electron yield and the Ar gas pressure while maintaining the XUV focus position and spectral width constant.

A slit size of approximately 100 µm was used in the experiment, resulting in the spectrum shown in the main part of Fig. 3.8. A spectrum obtained with an open slit configuration is shown in the inset. The comparison demonstrates how the contributions of the neighboring harmonics can be suppressed by reducing the slit size. Whereas for an opened slit the intensity of neighboring harmonics is of the same order as compared to the selected one, a high attenuation is achieved for the narrow slit width. The contribution of the 23rd harmonic, which remained in the spectrum, had to be multiplied by a factor of 330 to gain any visibility. From this measurement, an intensity ratio of $1 : 3 \times 10^{-4}$ between the selected and the neighboring harmonics of can be calculated. It is important to note that the slit

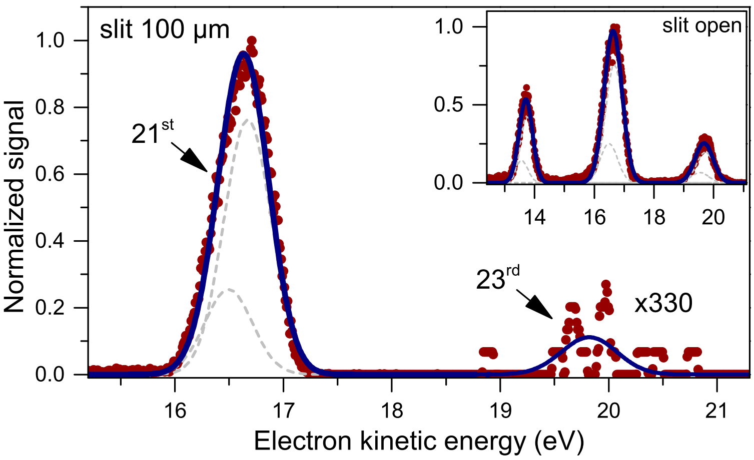

Fig. 3.8 Kinetic energy spectrum generated by ionization of Argon with the use of the RZP designed for the 21st harmonic and a slit width of 100 µm. The solid curve depicts a fit to a sum of two Gaussians representing the spin orbit splitting of the ground 3p state of the residual ion. The spectral contribution of the 23rd harmonic was multiplied by a factor of 330. The inset shows a spectrum obtained with an open slit configuration, giving rise to contributions of the neighboring harmonics of the same order as the selected one.

width of 100 µm does affect noticeably the transmission of the selected harmonic through the monochromator.

The fit of a sum of two Gaussian profiles, representing the spin-orbit splitting of 0.18 eV of the final state of Ar^+, is shown by the solid blue line whereas individual peaks are shown by gray dashed lines. The total width of the peak is given by the splitting of the two spin-orbit states convoluted with the bandwidth of HHG light as well as with the spectrometer resolution. Taking these facts into consideration, a spectral bandwidth of the XUV source of 0.5 eV (FWHM) is obtained. However, this finding is strongly related to a number of different parameters, namely the pump beam parameters such as the intensity, beam profile, and pulse compression, the focus position of the lens focusing the beam into the gas cell, as well as the gas pressure in the cell. In general, a lower pump beam intensity leads to a smaller bandwidth, accompanied by a decrease in the photon flux. For the conditions presented here, a flux of 10^6 photons per pulse was measured behind the monochromator, giving rise to a suitable XUV intensity in the experimental chamber. The spectral bandwidth and the peak position were determined by the same method on a daily basis to ensure constant experimental conditions throughout all measurements.

XUV Pulse Duration

The XUV pulse duration was measured by means of a cross-correlation technique. When the pump and the probe pulses overlap in time, a process of multiphoton ionization occurs that involves absorption of an XUV probe photon simultaneously with absorption or emission of one or more pump photons. This process does not require the presence of an excited state that can be resonantly populated by the pump beam. It has received a description in terms of laser-assisted photoionization of a medium [155,156]. In the cross-correlation experiment, argon gas was used as the sample and the fundamental IR beam was employed as the pump. Exposing an argon atom simultaneously to IR and XUV radiation, it can undergo the above mentioned multiphoton ionization transition. The kinetic energy of the photoelectron can be expressed as:

$$E_{kin} = \hbar\omega_{XUV} + N\hbar\omega_{IR} + I_p \tag{3.8}$$

where $\hbar\omega_{XUV}$ and $\hbar\omega_{IR}$ are the photon energies of the XUV and IR light, and I_p is the ionization potential of Argon. $|N|$ represents the number of involved IR photons and its sign describes whether the process is associated with absorption (positive) or emission (negative).

To initiate a multiphoton transition the IR field needs to be sufficiently strong. However, an upper limit is given by the process of above-threshold-ionization, leading to direct ionization of the argon atoms by the pump beam. Therefore, an IR peak intensity of approximately $2 \times 10^{12}\,\mathrm{W/cm^2}$ was chosen, satisfying both criteria. The IR pulse duration of 25 fs was measured with a SPIDER device. Figure 3.9 shows a sequence of kinetic energy spectra for different time delays between the XUV and IR pulses. In this experiment, the RZP designed for the 21st harmonic and a reduced HHG pump intensity of $1.5 \times 10^{14}\,\mathrm{W/cm^2}$ was used. One can see that several side bands (SB) appear on both sides of the main central photoemission peak The SBs are framed and labeled in the figure according to their number. For the IR intensities applied in this experiment, it is possible to use a perturbative approach to describe the cross correlation signal. In this case the ionization rate appears to be proportional to the product $I_{XUV} I_{IR}^{|N|}$, where I_{XUV} and I_{IR} are the intensities of the XUV and IR light. The total ionization yield in the N^{th} SB at a given time delay τ be represented by the integral:

$$S(\tau) \propto \int_{-\infty}^{+\infty} I_{XUV}(t)\, I_{IR}^{N}(t-\tau)\, dt \tag{3.9}$$

The dependency of the integrated yield on the time delay is shown in Fig. 3.10. Assuming Gaussian shapes for both XUV and IR pulses, one can calculate from Eq. 3.9 that the cross-correlation signal is given by a Gaussian shape as well:

$$S_N(\tau) \propto \exp\left(-\tau^2 \Big/ \tau_N^2\right) \tag{3.10}$$

with

$$\tau_N^2 = \tau_{XUV}^2 + \tau_{IR}^2 \Big/ |N| \tag{3.11}$$

In this equation τ_{XUV} and τ_{IR} denote the temporal width of the XUV and IR pulses, respectively. From Eq. 3.11 it can be concluded that the temporal width of the cross correlation signal is decreasing with the increase of the sideband number and converges to the value of the XUV pulse duration in the limit of large values of N. Taking this into consideration, Gaussian fits to the three sidebands shown in the inset of Fig. 3.10 revealed that the XUV pulse duration converges to 45 fs.

The laser-assisted photoeffect can also be accomplished on surfaces, which is used in the present work when solid state substrates such as ZnO or TiO_2 are investigated. It provides the same physical basis to measure the temporal system response.

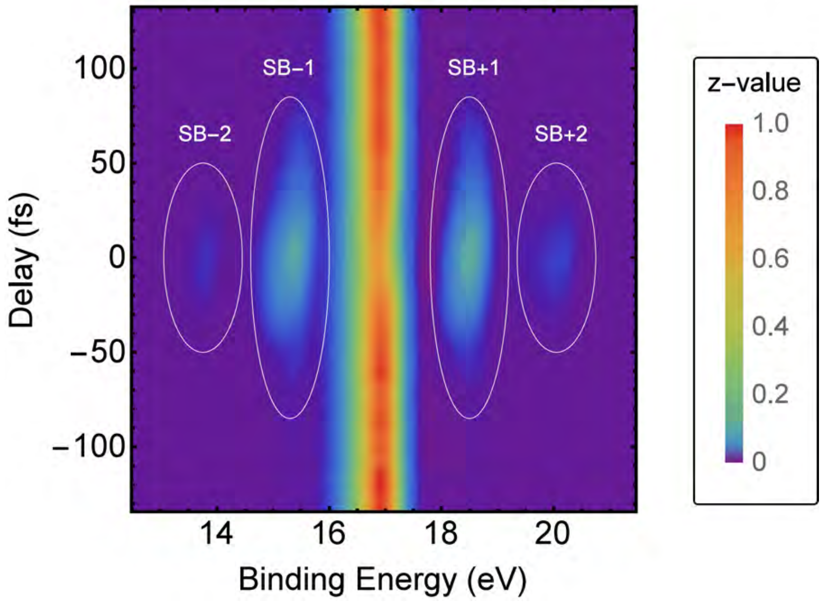

Fig. 3.9 Photoelectron spectra of Argon obtained for different time delays between IR pump and XUV probe pulses. The sidebands due to the emission and absorption of IR photons in the process of IR-assisted ionization arise when the two pulses overlap in time, giving rise to a cross correlation signal of pump and probe pulses.

3.2.1 The Time of Flight Spectrometer

In the present work, the commercial available photoelectron spectrometer THEMIS 600 (SPECS) was used. Its main principle relies on the measurement of the time-of-flight (TOF) of photoelectrons to a detector placed at a certain distance from the interaction region. The electrons velocity and kinetic energy can be derived from the measured TOF. Beside the energy dispersion, the THEMIS 600 exhibits additionally two features. (I) Due to a position sensitive detector angle-resolved PES is feasible. (II) The drift tube is equipped with electrostatic lenses giving rise to a very flexible use of the spectrometer in terms of acceptance

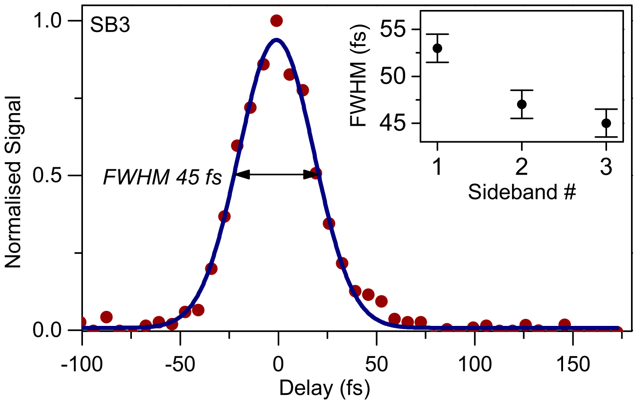

Fig. 3.10 Integrated yield of the third sideband (red circles) as a function of the pump-probe time delay. A Gaussian fit to the data points is represented by the blue solid line. The inset shows a comparison of the sidebands up to the third order, pointing out the convergence of their widths for increasing sideband number.

angle, energy- as well as angular resolution. In the following the two main operation modes and their properties will be described. A schematic drawing of the TOF including exemplary electron flight trajectories is shown in Fig. 3.11. It consists of ten cylindrical electrostatic lenses that are labeled L1-L10. To compensate external magnetic fields mu – metal shielding is used. The screening is extended in the sample area by Helmholtz coil pairs for each spatial dimension (not shown in the figure).

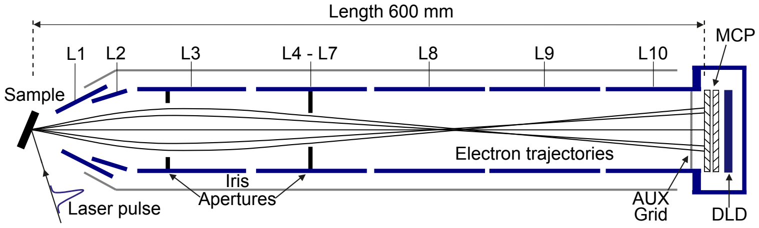

Fig. 3.11 Schematic view of the SPECS Themis 600 time-of-flight spectrometer. Electron trajectories are indicated by the black lines extending from the sample to the MCP/DLD detection unit. The electrostatic lenses are labeled L1 - L10 giving rise to a flexible use of the spectrometer in terms of energy- and angular resolution. The AUX grid positioned in front of the detector serves as a high-pass filter to avoid unduly large number of electron reaching the detector.

Electrons emitted from the sample surface are collected by the electrostatic lenses and imaged onto the detector. To this aim, a number of different lens modes are available. Additionally, a completely field-free operation (drift mode, DM) can be deployed were the spectrometer performs like a classical drift tube with an acceptance angle of ± 1°, given by the sample – detector distance and the detector aperture of 40 mm. However, larger acceptance angles, ranging from ± 3° to ± 15°, with simultaneously improved collection efficiencies are achieved in four distinct modes allowing angular resolution as well. An overview of modes is given in Table 3.3.

Table 3.3 Overview of the different operation modes that can be applied.

Mode	Abbreviation	Acceptance angle (°)
Drift Mode (lenses off)	DM	±1
High Angular Dispersion	HAD	±3
Medium Angular Dispersion	MAD	±5
Low Angular Dispersion	LAD	±7
Wide Angle Mode	WAM	±15

Further, two modes with spatial resolution exist, which are exclusively used for alignment purposes and are not explained in more detail here.

The electrons can be accelerated or decelerated by the electrostatics lenses. Following the definition used for hemispherical analyzers, the initial kinetic energy is denoted by E_{kin} and the final energy of the electron in front of the detector is denoted by E_{pass}. Due to a finite temporal resolution, both parameters can be used to balance the performance of the spectrometer between the maximum accepted spectral energy range and the energy resolution. To obtain kinetic energy spectra and emission angles, simulations of the electron trajectories in the electrostatic fields are needed. Such a transformation is fully integrated in spectrometers software.

Detector

The measurement of the TOF of photoelectrons relies on a start-stop method. A trigger signal synchronized with the laser defines the point in time when the laser pulse impinges on the sample and the photoelectrons are created. The stop signals are induced by single electron registration on the detector. The start and stop signals are allocated and their time difference constitutes the TOF. The spectrometer is equipped with a three-dimensional (x,y,t) delay line detector (DLD), which was developed and build by Surface concept. A simplified scheme is shown in Fig. 3.12(a). It consist of two microchannel plates (MCP), mounted in Chevron configuration, which amplify the incoming electrons. Behind the MCP, the electron cloud reaches two "crossed-serpentine" delay lines, each inducing an electronic pulse. The pulses propagate in both directions towards the ends of each line. In one dimension, the position of the incoming electron can be calculated by the signal arrival time differences at the opposite ends. Therefore, two delay lines crossed by 90° are needed to enable a two-dimensional position sensitive detection. Each end of the delay lines is connected to a constant fraction discriminator (CFD) and a time-to-digital converter (TDC) to measure the arrival times individually. The time coordinate can be calculated by the average of all four arrival times taking a general time off-set into account.

After an electron counting event, the detector cannot immediately process another one. This so called "dead" time given by the detector and the electronics lies in the range of 15 ns. For typical flight times of 100 ns, it implies that only one electron per laser pulse should be detected. Otherwise the detection of subsequent electrons generated by the same laser shot might be omitted or their position can be incorrectly registered. This would lead to a distortion of the measured spectra, e.g. overweighting of the fastest electrons which is called pile-up effect. To avoid an unduly large number of electrons reaching the detector, it is equipped with a low-energy cut off filter. It consist of a grid (AUXiliary) positioned in front of the detector, were a deceleration voltage can be applied blocking all electrons below a certain kinetic energy. Independent of the used spectrometer lens mode, the total count rate was always kept below the lasers repetition rate of 5 kHz.

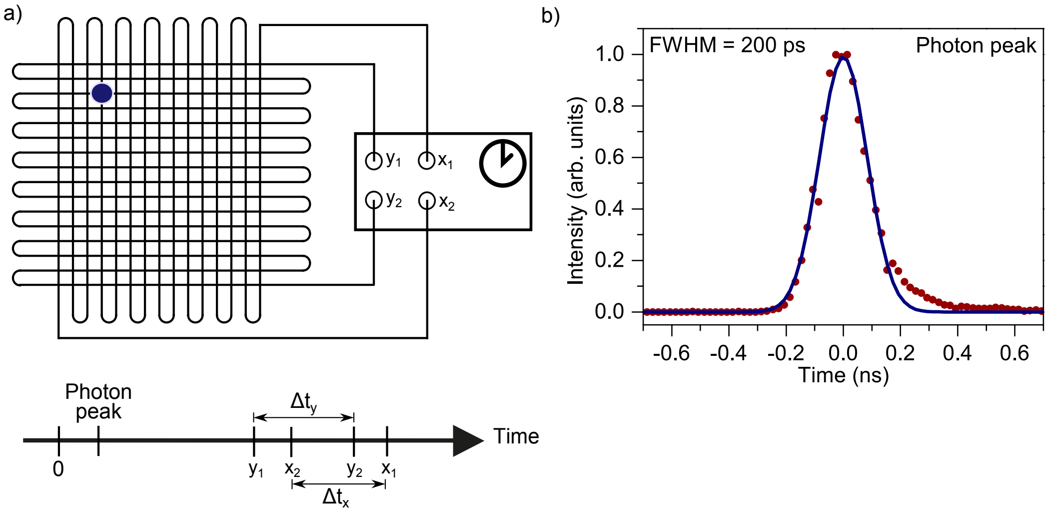

Fig. 3.12 Schematic drawing of the delay line detector (a) and detector response function measured by diffusely reflected laser light (b).

The detector response is shown in Fig. 3.12(b). It determines the time resolution of the system and is found to be approximately 200 ps. The response curve was measured with the use of photons that were diffusely reflected off the sample to the detector where they created photoelectrons. Due to the ultrashort time duration of the laser pulses, the peak solely represents the detectors response. Additionally, it is used to calibrate the time zero off-set while subtracting 1.8 ns given by the time of light propagation from the sample to the detector.

Data Acquisition

The data acquisition software was implemented in the programming language python. The original software delivered with the spectrometer was adapted by Daniel Tolksdorf to meet the required needs of pump probe spectroscopy. Therefore, the control of various experimental parameters e.g. control of delay stage position, beam shutter status, laser pulse intensity measurement and a rotational stage was combined in one main acquisition interface. Data acquired in a single measurement with a fixed set of parameters is stored in one file with HDF5 format (Hierarchical data format). This file contains all attributes of the measurement, the three dimensional TOF data (x,y,t) and a converted kinetic energy spectrum according to the used spectrometer mode.

To calculate kinetic energy spectra, the electron trajectories in the presence of the electrostatic fields have to be simulated. The overall distribution of the potential given by the ten electrostatic lenses can be calculated by a superposition of the individual lens contributions. With the software package SIMION, those single contributions can be obtained by taking the spectrometers geometry into account. For initially defined intervals of kinetic energy and emission angle at the sample, electron trajectories are simulated. This leads to a transformation matrix that maps kinetic energy and emission angle pairs to positions and transition times at the detector. By the inversion of this matrix the kinetic energy spectra can be calculated.

3.3 Sample Preparation

The ZnO and TiO_2 films used throughout this thesis were prepared by the group of Prof. Leone Spiccia form Monash University (Australia). Two different glass substrates coated with a conductive FTO layer were used. For the experiments with TiO_2 samples presented in section 4.1, conductive glass substrate with a FTO layer of $10\,\Omega/\text{cm}^2$ resistivity was purchased from Nippon Sheet Glass (NSG, Japan). For the experiments presented in section 4.2, FTO glass (TEC7) from the company Dyesol (Australia) was used. In both cases an area of 4×4 mm^2 size on the FTO layer surface was coated with a mesoporous semiconductor film with the use of a commercial semiautomatic screen printer and a commercial printing paste containing either colloidal TiO_2 particles of 18 nm average size (PST-18 NR, JGC Catalysts and Chemicals) or colloidal ZnO particles of 100 nm average size, (Nano powder, Sigma-Aldrich). Other chemicals were obtained from commercial suppliers and used as received. The N3 dye was purchased from Solaronix (Switzerland) and the N719 dye from Dyesol (Australia). For sensitization with the N719 dye, a solution was prepared with a 0.3 mM dye concentration in a mixture of acetonitrile and tert-butylalcohol with a volume ratio of 1:1. The sensitization with the N3 dye was carried out in a different manner, by using a dye solution of 0.3 mM concentration dissolved in ethanol (Sigma-Aldrich, HPLC grade). Prior to sensitization, the films were sintered at 500 °C for 30 min, cooled to 80 °C and then immersed into the dye solution. The TiO_2 electrodes were sensitized over night at room temperature. In the case of ZnO, a reduced sensitization time of 30 min was chosen in order minimize the impact of the dye solution to the samples [157]. The films were rinsed by the same bare solvent mixture to remove unbound dye and afterwards were transferred in atmosphere into the experimental vacuum chamber. A typical residual gas pressure in the chamber was in the range of 10^{-7} mbar during the experiment.

The part of the FTO layer surface which remained uncoated with the semiconductor films served as a reference sample, with the dye not linked to TiO_2 or ZnO, respectively. Especially for the investigation presented in section 4.1, a comparison between the N719/TiO_2 and N719/FTO interfaces was conducted. In addition to all sensitized electrodes, the corresponding un-sensitized / bare samples were prepared as well. Because of the ex-situ sample preparation, special attention was paid to possible surface contamination. To exclude any influence by contaminants, measurements on these identically prepared un-sensitized samples were performed (see section 4.1.3: Pump-probe measurements on bare substrates). Slight changes of the samples spectra were observed when exposed to the XUV beam on a time scale of several ours. Therefore, the sample position was changed according to this finding. Detailed analysis of XUV-induced sample damage can be found in section 4.2.3 (Sample damage measurements).

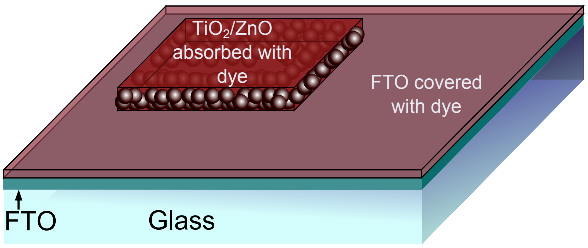

Fig. 3.13 Schematic view of the prepared samples. Mesoporous nano colloidal TiO_2/ZnO films with an 4 × 4 mm^2 area were screen-printed on commercial available FTO glass. After sensitization the dye is absorbed onto the semiconductor film as well as onto the FTO layer surface.

3.4 Space Charge Effect

This section is based on publication (5): New Journal of Physics, 2015, 17 (93016).

When pulsed and intense light sources are used in photoelectron spectroscopy experiments the photo-emitted electrons can experience energy redistribution after their escape from the sample surface [158,159]. This occurrence, in general denoted as the space charge effect (SCE), can cause spectral shifts and broadenings distorting the intrinsic information contained in the photoelectron spectrum and often represents a limiting factor in experiment. The development of photon sources with ultrashort pulse length, e.g. achieved by utilizing HHG or in FELs, and the improvements on the photoelectron analyzer side has moved this issue increasingly into focus [160–164].

When SCEs are considered two different scenarios have to be distinguished. In static PES experiments with an ultrashort and intense XUV photon pulse a single electron cloud is produced within a relatively short timescale and with a high electron density in front of the samples surface. Because of the Coulomb interaction, the fast electrons tend to be pushed by the electrons behind them whereas the slow electrons are retarded by those fast electrons resulting in the previously described effect of a spectral broadening and shift. Additional complication arises when PES is conducted in a time-resolved pump-probe manner. Here, a second electron cloud is produced by the pump beam interacting with the electron cloud generated by the probe. In this case the SCE does not solely depend on the parameters of both laser pulses but rather the temporal delay between the two emitted electron clouds has to be considered. In the scope of this work the former effect within a single electron cloud of the XUV probe pulse appears to be negligible due to the relatively weak XUV photon flux used in the experiments. However, the intensity requirements for the pump pulse in order to sufficiently excite the sample leads to direct multiphoton ionization of the sample and results in the second described scenario of interacting electron clouds. The effect on the XUV photoelectron spectra and its dependency on the pump beam intensity as well as pump probe delay represent the subject of this section.

Previously, this effect was also reported in other pump-probe PES experiments, where XUV light [165,166] or soft X-ray [167] and hard X-ray [168] radiation was used to probe a solid-state sample irradiated by a pump laser pulse. Common to all of these investigations is the fact that the electron cloud generated by the pump laser pulse causes a shift of the photoelectron spectra to higher kinetic energies. The same effect was obtained in this work when time resolved PES was applied to the solid state substrates. However, as we could demonstrate in our recent investigation on liquid samples SCE associated with negative spectral energy shifts can occur [169]. This finding is especially important when the results obtained with the use of ionic liquids as a solvent are presented later.

As discussed in Ref. [168] and [169] a simple mean-field model can quantitatively predict the spectral shift of the photoelectron spectra caused by the SCE. An illustration of the charge dynamics is shown in Fig. 3.14 for the two cases with the probe (a) or pump pulse (b) being the first laser beam interacting with the sample.

As a first step, solely the interaction of the both electron clouds produced by the pump and probe beams will be considered. For both pulse sequences this interaction leads to the negative SCE accelerating the XUV electrons. This can be easily understood for the case of the probe pulse being first and the pump beam ionizing afterwards (Fig. 3.14(a). The electron cloud of the probe beam is pushed by the pump electron cloud behind them leading to the described effect. For the reversed pulse sequence the difference in kinetic energy has to be additionally taken into account. Due to the much higher photon energy the kinetic energy of the probe electron cloud is sufficiently high to reach the cloud of the pump generated slow electrons and penetrates through it. Although being initially decelerated an overall net energy gain for the XUV cloud is achieved. Detailed calculations for this scenario can be found in Ref. [169].

An example of exclusively negative space charge obtained with N3 sensitized TiO_2 substrate can be seen in Fig. 3.15. Here, the shift in kinetic energy of electrons originating from the N3 HOMO peak for a pump-probe time delay range of ± 150 ps is shown. The horizontal dashed line indicates the position of the peak of about 26.0 eV in the photoelectron spectrum without any pump beam applied. For overlapping pump probe beams a shift to higher kinetic electron energies and therefore lower effective binding energies can be seen. For different pump probe time delay the corresponding photoelectron spectra are shown in Fig. 3.15(b). With the pump intensities 2×10^{10} W/cm^2 used is this experiment a maximum shift of about 300 meV to higher kinetic energies was observed. One can see that for time delays larger than ± 150 ps the SCE vanishes whereas is reaches its maximum at zero time delay.

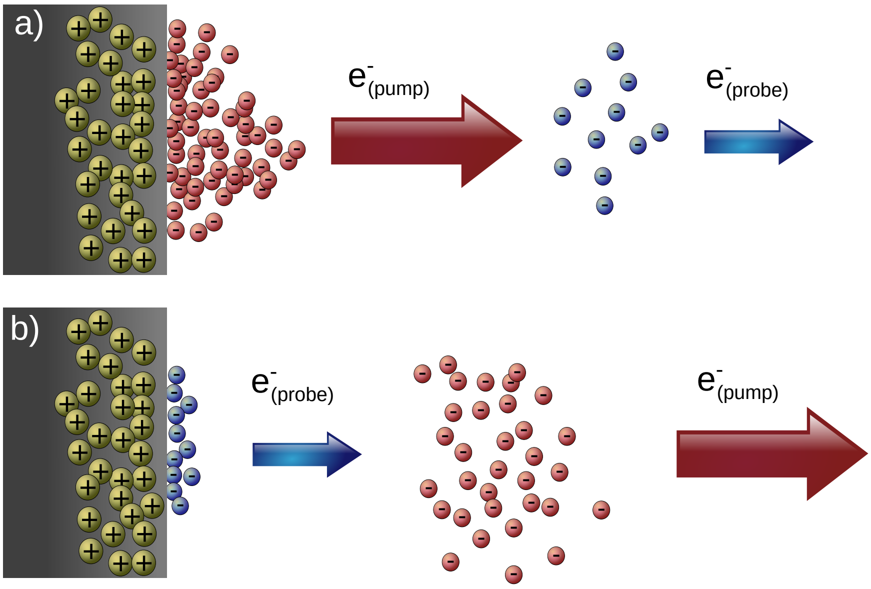

Fig. 3.14 Illustration of the space charge effect for the two different sequences of pump and probe pulses. In a) the probe pulse arrives first and the pump secondly whereas in b) the opposite situation is depicted.

This characteristic enables to use the SCE as a method to align the spatial overlap as well as to approach the temporal overlap of XUV and laser pump pulses within a sub-picosecond precision. This is accomplished by applying the high pass energy filter in the spectrometer cutting most of the spectrum for the situation when pump beam is not present. Hence, if the pump beam is added the positive SCE leads to a higher amount of electrons passing the filter and results in an increasing total electron yield.

The intensity of the space charge effect relies most notably on the pump laser pulse parameters. Figure 3.16 demonstrates the appearance of the SCE effect in XUV spectra obtained for three different values of the pump pulse energy. In case of a pulse energy of 1 µJ, corresponding to a peak intensity of 10^{10} W/cm^2 of the pump beam, the SCE effect can

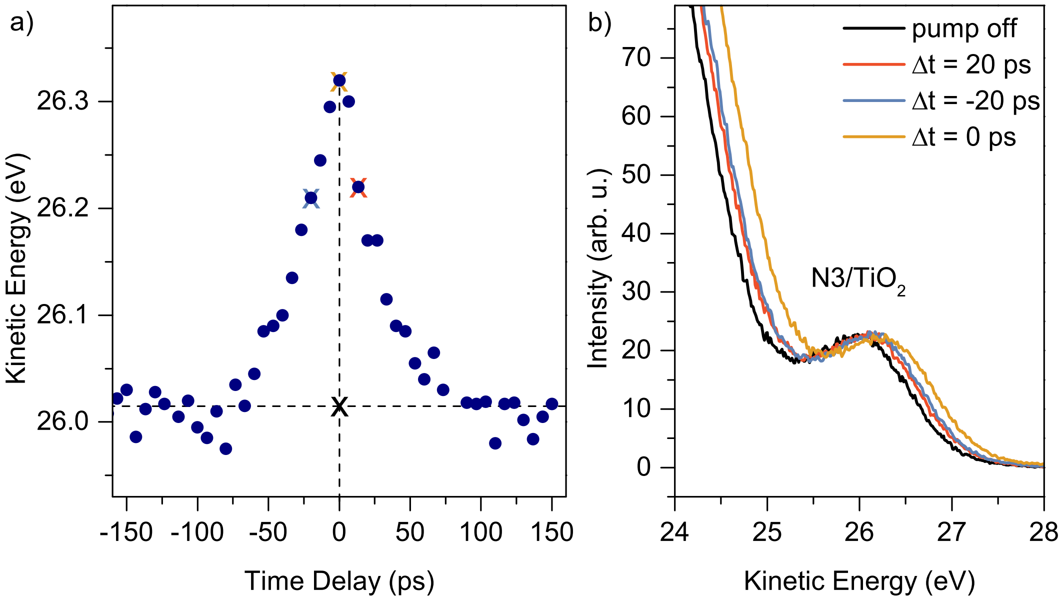

Fig. 3.15 Space charge effect in dependence of the pump probe delay. In a) the kinetic energy of the N3 HOMO band peak as a function of the time delay between pump and probe pulses is plotted. The colored crosses indicate the associated spectra presented in b) for different time delays. The black colored line represents the spectrum obtained without any pump beam applied.

be neglected. For higher peak intensities of the pump beam the density in the electron cloud generated by the pump increases and the kinetic energy distribution changes to higher values. Therefore the influence to the probe electron cloud is stronger leading to a larger SCE shift as in this case of up to 4 eV. However, even higher intensities can result in additional spectral broadening and ultimately in a complete distortion of the spectra. This is in contrast to two relevant aspects related to the time resolved experiments. Most important is achieving a high time resolution being directly associated with the use of ultrashort and intense pulses. And secondly, to excite a sufficient amount of sample the total photon flux needs to be high. In some cases it unavoidable to satisfy both criteria so that it might be necessary to work in a moderate SCE regime. Therefore algorithms were developed and can be applied to compensate for the SCE. Their function and use during the data analysis will be noted later.

The general difference when considering solid state samples and liquids lies in their carrier mobility. The intense pump beam ionizes the sample, which therefore acquires a residual positive charge localized within the interaction region of the laser beam. This fact is indicated by the positively charged atomic cores in Fig. 3.15. Considering solely the presence of this attractive force to the probe electron cloud the decrease in their kinetic energy is easy to understand. Depending on the carrier mobility the dissipation of the induced positive charge can occur on an ultrafast time scale and hence the possible interaction can be disregarded. For solid state samples with a rather high carrier mobility this is valid, whereas for liquids as

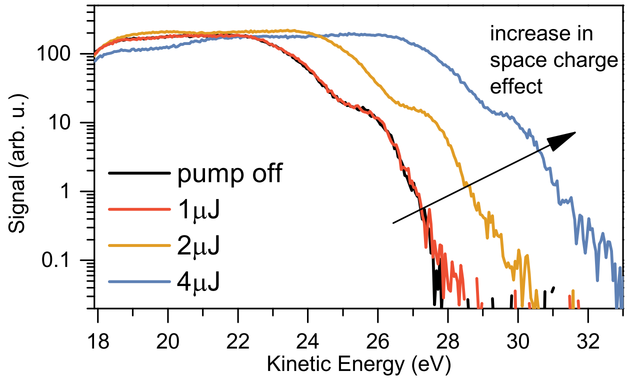

Fig. 3.16 XUV spectra of the sensitized ZnO sample recorded for three different values of the pump pulse energy and temporal overlap: 1 µJ (red), 2 µJ (orange), and 4 µJ (blue). The black line shows a steady-state XUV spectrum without any pump beam applied.

well as other non-conducting samples the positive SCE, decelerating the electrons kinetic energy, needs to be taken into account. The positive SCE, being a special property when liquid samples are used, is discussed in detail in Ref. [169]. An example for a positive SCE that emerges with the use of ionic liquids is presented in Fig. 3.17. The SCE in dependence of the pump probe delay is shown and for a positive delay times (pump excites first) a shift of the kinetic energies to lower values can be obtained.

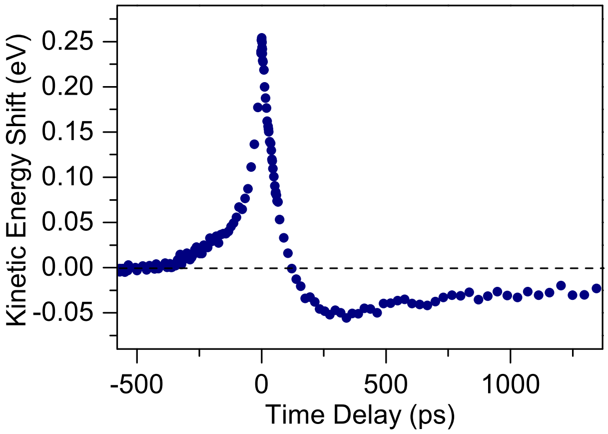

Fig. 3.17 Space charge effect in dependence of the pump probe delay obtained on ionic liquid sample.

Chapter 4

Results and Discussion

This chapter presents and discusses the results of the time-resolved measurements conducted at the different interfaces and samples. It is divided into three main parts covering the previously introduced issues of the charge transfer at the dye semiconductor interfaces and the electron dynamics of the ruthenium complex dissolved in ionic liquids.

4.1 Injection Kinetics and Electronic Structure at the N719/ TiO_2 Interface

Publication (4) reproduced in part with permission from Journal of Physical Chemistry C, 2015, 119 (17), pp 9099-9107. © 2015 American Chemical Society

4.1.1 Motivation

Heterogeneous electron transfer (HET) at the interface between a molecular dye and a wide-band gap semiconductor plays a crucial role in photovoltaic devices or for photocatalytic solar fuel generation [6,10]. Following the invention of the nanostructured dye-sensitized solar cell (DSSC) by Grätzel and O'Regan [8], considerable efforts have been made to investigate light induced fundamental processes related to such devices. It was found that the ruthenium-based dye complexes, e.g. $(Bu_4N)_2Ru(dcbpyH)_2(NCS)_2$ (N719), exhibit high efficiency (close to unity) of the HET mechanism in the visible range of the solar spectrum [61,170,171]. Due to this property and the achievement of solar-to-electric energy conversion efficiency exceeding 10%, the N719 complex has been considered over the years as a reference dye for studying fundamental aspects of photo induced electron transfer properties in the DSSCs [5,170].

The high injection yield of electrons into the semiconductor state is related to a rather fast HET process compared to other competing reaction channels. In order to reveal the competition of different processes, the application of ultrafast time-resolved spectroscopies is, therefore, needed to follow the complex electron dynamics induced by photoexcitation at the dye-semiconductor interface.

Femtosecond transient absorption spectroscopy represents so far the most common method used for studying the electron dynamics at interfaces. This method was applied, in particular, to investigate the injection kinetics from the Ru-based dye complexes to a TiO_2 layer. The injection process was found to exhibit a coexistence of an ultrafast ($\leq$100 fs) transfer component and one or more slower components occurring on a picosecond and even longer timescales [41,172-175]. This feature is associated with the population dynamics of different metal-to-ligand charge-transfer (MLCT) states of the dye complex. Following excitation at the maximum of the absorption band, the dye is initially prepared in the singlet ^{1}MLCT state. This state promotes the fast electron transfer directly into the conduction band (CB) of TiO_2, which takes place simultaneously with an internal relaxation into the triplet ^{3}MLCT state via intersystem crossing [176-180]. Both injection and relaxation processes were found to occur on a timescale of 50-100 fs [181,182]. Injection from the relaxed triplet state is significantly slower and occurs on a picosecond timescale. To account for the competition in the injection kinetics between the direct electron injection and the intramolecular relaxation, Asbury et al [179]. proposed a two-state injection model. The ratio between the short- and long-lived states were found to depend on the excitation wavelength, confirming that the main injection channel originates from the nonthermalized singlet ^{1}MLCT state [179]. The two state injection process is schematically depicted in Fig. 4.1.

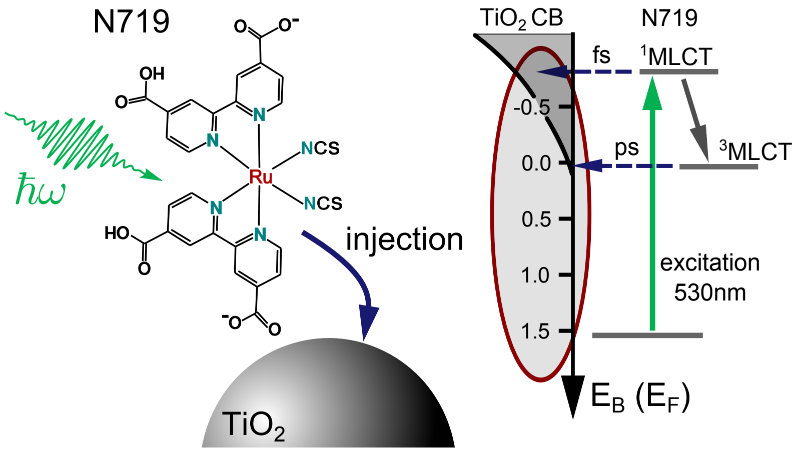

Fig. 4.1 Illustration of the light induced HET process at the dye N719 / semiconductor interface. In the right part of the figure the two state injection model is presented. For further details see text.

Apart from the injection kinetics, the binding energies of the ground and excited states and their match at the dye–semiconductor interface are fundamentally important for the function of a DSSC. On the one hand, the energy difference between the donor (excited dye) and the acceptor (CB of TiO_2) determines the driving force for the electron transfer [183], and on the other hand, the excess energy represents a dissipation mechanism and by that influences the overall reachable conversion efficiency of the cell. Thus, a detailed knowledge of the energy structure is inevitable to better understand various experimental aspects and to specifically design new and more efficient sensitizers. For Ru-based sensitizers, the ground- and excited-state redox potentials were measured by cyclic voltammetry combined with absorption and emission spectroscopy [184–186]. The molecular band alignment with the CB of TiO_2 was predicted by theory and the calculated results were verified by comparison with the absorption spectra [187,188]. However, direct experimental knowledge of the energetics at the dye–semiconductor interface is not available until today and the development of other approaches is required to gain insight into the actual band alignment.

The method of transient absorption spectroscopy does not provide a direct measure of binding energies. The changes in absorption signal are related to the formation of positively charged dye cations or to the density increase of free electrons in the CB of the semiconductor. The actual transitions that involve population of excited states are probed indirectly, and it is difficult to draw conclusions about the energy structure in this case.

Therefore the capabilities of femtosecond time-resolved photoemission spectroscopy (PES) are examined in both revealing the injection kinetics and determining the binding energies of the involved states. An attempt is made to verify the current understanding of ultrafast charge transfer at the N719/TiO_2 interface and to provide additional information about the binding energies for the involved excited states. As a reference sample, the fluorine-doped SnO_2 substrate (FTO) covered with dye is used. By measuring the injection kinetics at the N719/TiO_2 interface in comparison to the N719/FTO interface, conclusions about the unique properties of the TiO_2 electrode can be drawn. Such a comparison is straightforward to make, since the HET process at the N719/FTO interface is much slower and, in particular, the ultrafast injection component is highly suppressed.

4.1.2 Sample Characterization

To characterize the samples ground state structure steady state XUV spectra were recorded for the bare and sensitized TiO_2 and FTO samples. The results are presented in Fig. 4.2. Equal acquisition times were used throughout all spectra and no normalization was applied. The positions of the higher-lying energy levels are important for the photo induced electron transfer at the N719/TiO_2 interface and can be elucidated from these measurements.

The valence-band edge of the nonsensitized TiO_2 sample lies at a binding energy of 3.2 eV, which is in good agreement with previously found values in literature [189,190]. It was obtained by fitting a line to the spectral onset and using the intersection point of this line with the abscissa axis. Although this method represents a standard procedure in literature to determine the valence band edges of semiconductors it renders slight uncertainty. From the analysis of the absorption spectrum measured for bTiO_2, we obtained a value of 3.3 eV for the energy gap between the valence and conduction bands. Using this value, the conduction band edge position can be estimated to lie 0.1 eV above the Fermi edge [71].

For the sensitized sample, the maximum of the HOMO band of the N719 dye arises at a binding energy of 2.2 eV. This value is in agreement with other reported results for the N719/TiO_2 interface [71]. The bandwidth is found to be 0.6 eV after deconvolution with the spectral response of the system. Profound DFT calculation revealed the contributions to the highest occupied orbitals [191] giving rise to this broad HOMO band. As for the prototype molecule $[Ru(bpy)_3]^{2+}$ the highest three HOMO levels have essentially Ruthenium t_{2g} character, but for the N719 dye a considerable contribution coming from the thiocyanate (NCS) ligand orbitals mix in an antibonding fashion with the metal states [192]. The substantial contribution from the NCS group was also found experimentally before by Rensmo et al. [193]. The subsequent HOMO-3 level is comprised of an isolated orbital made of a nonbonding combination of the sulfur lone pairs and the nitrogen p orbitals localized on both NCS ligands [191]. Theoretical calculations predict this contribution lying 0.3 eV below the HOMO-2. This implies that the HOMO band has to be treated as a combination of different orbitals and its maximum does not directly reproduce the central position for the maximum overlap to the excited ^{1}MLCT state. This fact has to be kept in mind when the band alignment at the interface is discussed later.

At binding energies larger than 4 eV, photoemission from the valence band of TiO_2 dominates the ionization yield. In this energy range, the signal intensity of bTiO_2 is higher. This is due to the fact that, for the sensitized sample, the dye absorbs XUV light as well as attenuates electrons emitted from the substrate.

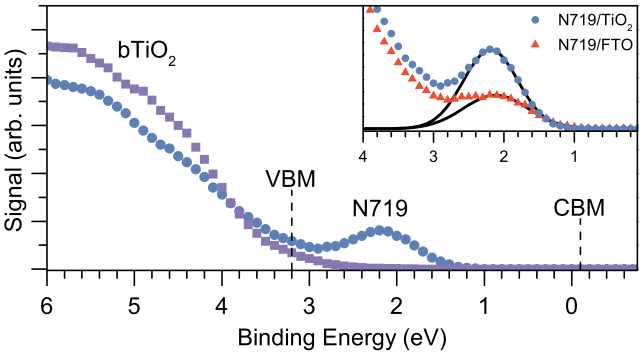

Fig. 4.2 Steady-state XUV spectra of photoelectrons recorded for the bare (squares) and sensitized (circles) TiO_2 samples. The emission peak from the ground state of the dye is labeled by N719. The inset shows a comparison of emission spectra obtained for sensitized TiO_2 (circles) and FTO (triangles) samples. The solid lines show the fit results of the HOMO ionization signal to a Gaussian profile.

The inset of Fig. 4.2 shows a comparison of XUV spectra of the sensitized TiO_2 and FTO electrodes. For both samples, the ionization contribution from the HOMO band was fitted to a Gaussian profile in the region of lower binding energies where contribution from the valence band of the substrate can be disregarded. One can see that the HOMO-band contribution for the TiO_2 electrode appears stronger and its peak position lies 0.1 eV higher on the energy scale. The difference in the ionization yield from the HOMO bands can be easily understood as being due to a different surface roughness of the two electrodes, leading to a different amount of dye deposited on the surface. This is an important issue here, since the FTO substrate is used as a reference and the transient signal needs to be normalized to the amount of deposited dye.

From the results shown in Fig. 4.2, one finds that the colloidal TiO_2 surface exhibits by a factor of 2.4 higher amount of dye than the FTO surface. This was obtained by comparing the HOMO-band yields integrated over the respective Gaussian profiles. The reason for the slightly different position on the energy scale is most probably caused by the difference in the electronic coupling between the dye and the two surfaces. The alignment of the ground-state energies of the dye absorbed on TiO_2 was analyzed by DFT calculations [187]. However, theoretical investigations of electronic coupling for FTO are not available. These investigations are needed to reveal the difference in the electronic structure at the two interfaces, giving rise to different HOMO peak positions. It is important to note that the character of the dye-surface interaction affects not only the energetic structure at the interfaces but also the electron kinetics at higher excitation level, which will be considered in the subsequent discussion.

4.1.3 Time-dependent Cross-correlation on the Bare Surface

Before considering the injection kinetics at the dye-semiconductor interface, it is instructive to present results of pump–probe measurements with the use of the bare TiO_2 and FTO samples. The spot sizes of the pump and the probe beams at the sample were 500 and 100 µm, respectively. A pump pulse energy of 4 µJ was used, corresponding to a photon flux of 5×10^{15} $photons/cm^2$ in the interaction region and a peak intensity of about 10^{10} $\mathrm{W/cm^2}$. This intensity was used to prevent excessive direct ionization of the sample by the pump beam. At such an intensity, only a small amount of slow electrons is generated by the pump pulse and their contribution to the higher-energy part of the XUV spectrum is negligible. The spectral shifts due to the space charge effect, as described in section 3.5, was also negligibly small. This was verified by comparing the pump–probe spectra recorded at negative time delays (the probe pulse arrives first to the interaction region) with the steady-state XUV spectra. The negative-delay pump–probe spectra are, thus, used as a background measurement in the analysis of transient spectra presented in the following.

Similar to the determination of the XUV pulse duration presented in section 3.2 by means of a cross-correlation (CC) measured in argon the temporal resolution can be obtained on the bare substrate surfaces. However, beside the knowledge of the CC width, which is important during the data analysis of the ultrafast dynamics, these measurements facilitate to reveal possible contributions from the substrates to the signal of the sensitized samples. Due to ex-situ preparation of the samples it is not possible to exclude a priori any contamination (e.g., by water or organic materials). Since PES is highly surface sensitive the influence and contribution of the substrate to the transient signal has to be carefully examined. This issue has received in literature only minor attention. Hahlin et al. [194], who implemented the same method of sample preparation as used in the present work, concluded that water does not contaminate ex-situ prepared electrodes. The influence of the contamination by organic materials was investigated by Lyon et al. [71]. and it was argued that such impurities introduce only weak interface dipoles, and their effect is insignificant to the measured band alignment of the involved states. A different situation appears when ultrafast dynamics are considered. Even without any signature of contamination to the steady state spectra a contribution from the substrate to the transient signal might be present. Therefore the same sample preparation used for the sensitized samples was applied to the bare ones.

As described before if the pump and the probe pulses overlap in time, a process of multiphoton ionization occurs that involves absorption of an XUV probe photon simultaneously with absorption or emission of one or more pump photons. This process does not require the presence of an excited state that can be resonantly populated by the pump beam [155,156]. The ionization yield integrated over a sideband of the laser assisted ionization process represents a cross correlation signal of the pump and the probe beams. By recording the CC signal at higher kinetic energies in the XUV emission spectrum as a function of the time delay the CC trace can be obtained representing a convolution of temporal profiles of the pump and the probe pulses. However, if any resonant state is involved in the two photon transition yielding a lifetime comparable or even larger than the pulse duration of pump and probe the CC gets asymmetric and the maximum amplitude is shifted with respect to the time zero of the overlapping pulses. That means any asymmetric result obtained in the CC measurement would indicate the presence of contaminations or that the substrate itself yields a transient signal possibly intermixing with the sensitized signals. The latter fact can be excluded by considering additionally the energetic position of the transient signal obtained in the spectra. This helps to determine the signals origin and to distinguish between the contributions from the bare and sensitized substrates. The results recorded with the bTiO_2 sample are presented in Fig. 4.3. A fit of the experimental data to a Gaussian profile yields a CC width of 98 fs (FWHM). This value constitutes the time resolution in the pump-probe measurements. Furthermore the signal appears to be highly symmetric with regards to zero time delay. As a result, the lifetime of a resonant state, if any is present at all, is expected to be well below this time scale.

In Figure 4.4 the appearance of the corresponding ionization sidebands in the kinetic energy spectra are shown. Here, in panel a) the spectra recorded at time delays of 0 and ±100 fs are presented. Their difference, shown in panel b, reveals the energetic position of

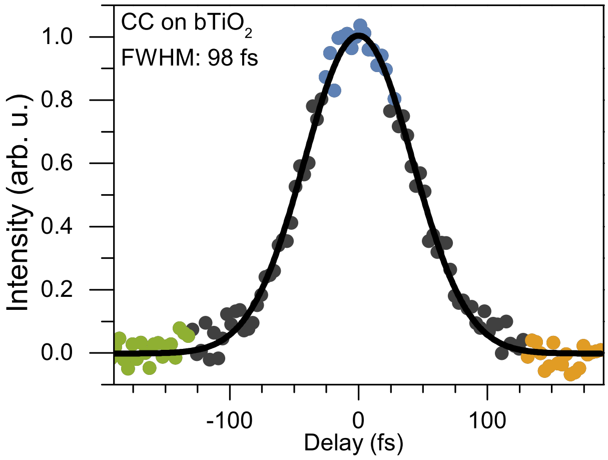

Fig. 4.3 Cross correlation measurements performed with the bare TiO_2 sample. The background-subtracted transient signal is shown, the solid curve shows the fit of the CC trace to a Gaussian profile yielding a CC width of 98 fs (FWHM). The colored ranges indicate the pump probe time delay at which spectra shown in Fig. 4.4 were taken.

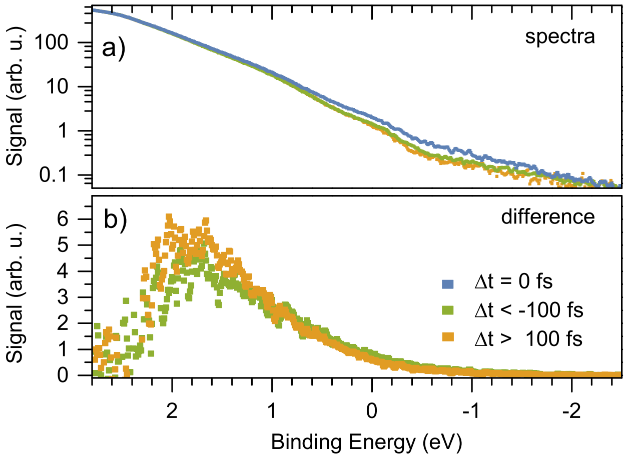

Fig. 4.4 Photoelectron spectra recorded at −100 fs (green), 0 fs (blue), and 100 fs (yellow) time delays. In b) difference between the spectra is presented.

the CC signal. It can be seen that the CC signal extends over a range from 0 eV up to 2.5 eV in binding energy. This fact should be kept in mind when the transient signal arising from the sensitized samples is analyzed. It is important to note that XUV spectra recorded at a given positive or negative time delay of the same absolute value are identical. This means that the pump beam does not initiate electron population dynamics in the bare samples, and laser assisted ionization is the only process where it plays a role. Very similar results were obtained for all other non-sensitized samples.

4.1.4 Ultrafast Kinetics on Dye Sensitized Samples

The injection kinetics at the dye-sensitized samples was studied with the same experimental conditions as described above. A comparison of spectra obtained at different pump-probe time delays is shown in Fig. 4.5. The spectra were recorded in drift mode (DM), which means that the spectrometers electrostatic lenses are switched off and a broad spectral overview can be acquired. In the binding energy range of around 0 eV a clear transient contribution gets visible. It lies well above the HOMO band of N719 and encompasses the ionization contributions from transient states excited by the pump beam. Furthermore, the transient signal changes for the two given time delays already indicating the different transient contributions that can be assigned to different excited states and their lifetime.

However, to gain a comprehensive picture about the ultrafast kinetics it is inevitable to measure transient spectra for a much larger number of pump-probe delays. Recording a time window of one picosecond with a step size of about 10 fs, yielding one tenth of the measured CC bandwidth, implies the acquisition of 100 spectra. Though, the acquisition time of a single spectrum presented in Fig. 4.5 required more than one hour rendering this approach nearly impossible. The reason can be found on the one hand in the rather low amount of transient contribution to the overall signal and on the other hand in the limited count rate of the spectrometer given by the low repetition rate of laser system. The former issue is easily understood by the fact that in DM the HOMO band contribution yields about one percent to the total spectrum. If one assumes an overall excitation of again one percent one ends up in a very small fraction of the spectrum comprised of transient signal. To overcome this limitation the spectrometers wide angle mode (WAM) is used giving rise to a much higher collection efficiency. In turn, the spectrometers high pass filter has to be applied to avoid unduly large count rates and by that restricting the measurable kinetic energy range as indicated in Fig. 4.5. The usage of the WAM allows to reduce the acquisition time by more than two orders of magnitude compared to DM preserving the same signal-to-noise ratio. This calculation clarifies that the WAM of the spectrometer is a key factor for the successful realization of the experiments presented here.

A complete overview of the transient signal recorded for the N719/TiO_2 and N719/FTO interfaces with the use of the WAM can be seen in form of color maps in Fig. 4.6. Both spectra

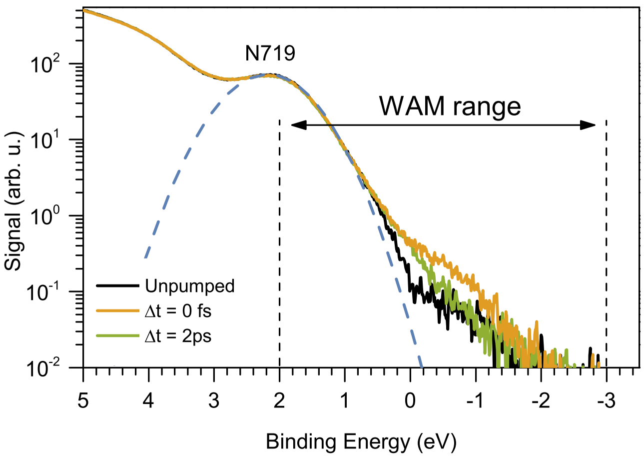

Fig. 4.5 Transient XUV spectra recorded in DM at zero (yellow line) and two ps (green line) time delay compared to the unpumped (black line) spectrum. A clear transient contribution in the range between -2 and 1 eV binding energy can be seen. Additionally the WAM measurement range is indicated.

were obtained with identical integration time and pump intensity and were not normalized. Pump-probe spectra for negative time delays were used as a background correction. In both cases compared to the CC measurement on the bare substrate a clear asymmetric signal is visible. Different spectral components are present exhibiting lifetimes beyond the CC temporal bandwidth. To gain better insight into the transient data cross-sections along the time and energy dimension were examined. Figure 4.7 shows the transient signal recorded for both interfaces in the time domain. The signal represents an electron yield integrated over the range of binding energies between -2 and 1 eV. In this figure the dramatic difference in the electron population dynamics of the sensitized samples as compared to the CC trace of bare samples, which is also reproduced by the gray line, becomes even more apparent. Except for short time delays in the vicinity of time zero, where the finite time resolution prescribes the Gaussian shape of the transient signal, both curves in Fig. 4.7 exhibit a multicomponent exponential decay. This decay, however, is different for the two samples, which allows to identify the unique properties of the electron transfer at the N719/TiO_2 interface. The main difference arises on the early timescale below 2 ps, where the two transient dependencies exhibit a fast decay but clearly deviate from each other. At time delays larger than 2 ps, both transients manifest a similar slow decay that occurs on a timescale of several picoseconds (see the inset in Fig. 4.7 for a larger delay range). In order to identify different decay channels and to determine the binding energies of the involved transient states, we consider separately the XUV spectra measured for the two distinct time domains: at time zero and at time delays larger than 2 ps. These spectra are shown in Fig. 4.8 a) and b).

The long-lived species appear to have the same binding energy and decay rate for both sensitized samples. Therefore, this spectral component is assigned to the population of the

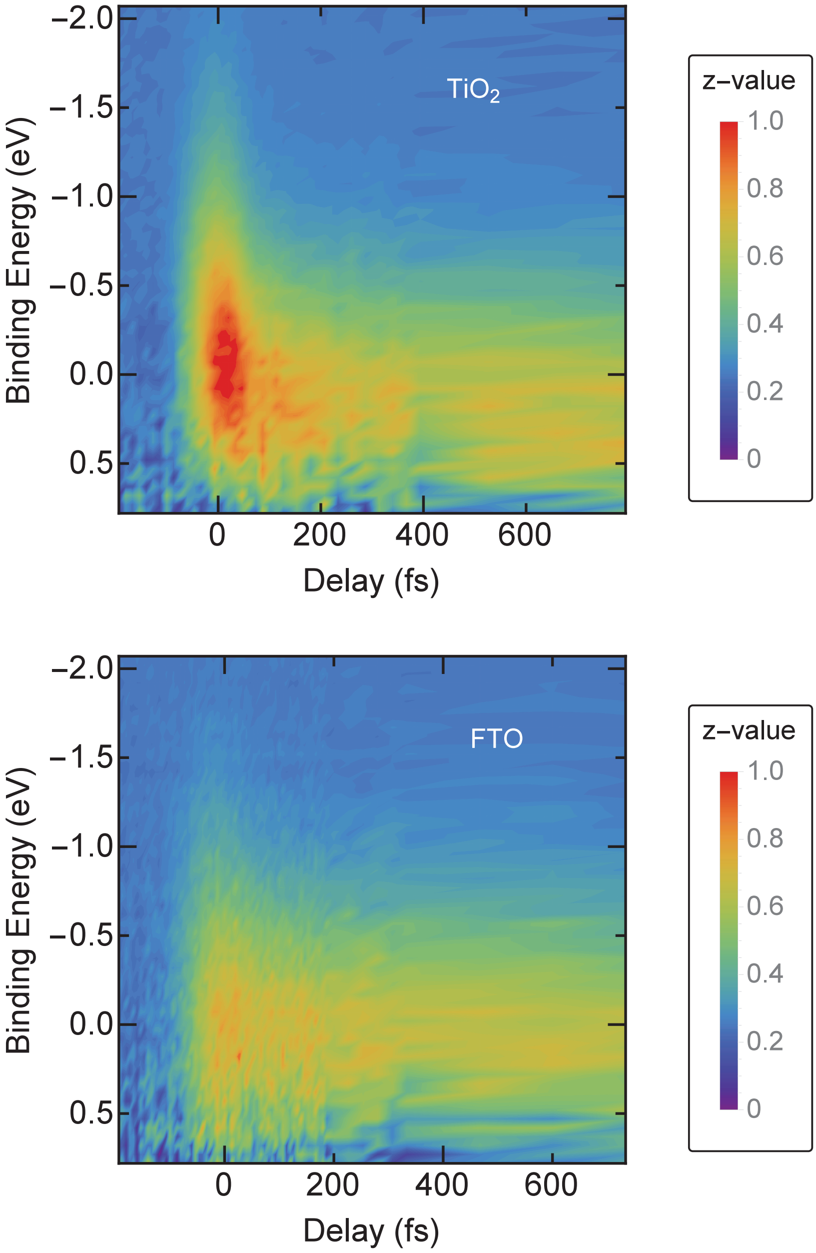

Fig. 4.6 2D color maps of the background-subtracted transient signal obtained at on the sensitized TiO_2 (upper panel) and FTO (lower panel) substrates. The same color scale is used in both representations. The signal was recorded with identical integration time and pump intensity.

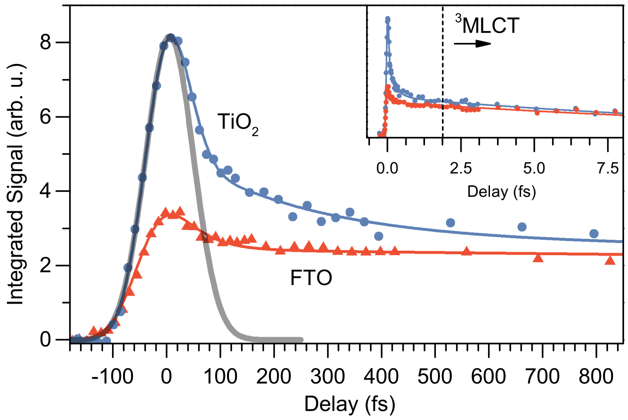

Fig. 4.7 Transient XUV ionization signal from sensitized TiO_2 (circles) and FTO (triangles) samples. The inset shows the transient signal in a larger range of time delays. The vertical line indicates a time delay beyond which the transient signal is dominated by ionization from the ^{3}MLCT state. The solid lines represent fits to the transient signals.

thermally relaxed ^{3}MLCT state of the dye. This is in accordance with the known fact that the triplet state manifests similar injection kinetics at different interfaces[176,181]. Its binding energy of 0.1 eV and a width of 0.8 eV were obtained from a fit of the energy peak to a Gaussian profile (see Fig. 4.8(b)). The specified width represents a result of a deconvolution with the spectral response of the system. It follows that the ^{3}MLCT state lies 0.2 eV below the conduction band minimum. Injection from this state, however, is possible due to its large bandwidth, resulting in a partial energy overlap with the conduction band.

In order to reveal in more detail any differences in the early time dynamics at the N719/TiO_2 and the N719/FTO interfaces, the slow-decaying ^{3}MLCT energy peak was subtracted from the spectra recorded at time zero. The results of the subtraction are shown in Fig. 4.8(c). One can see that the residual signal for the FTO sample is much smaller than for the TiO_2 sample, much more important, the structure of the residual spectrum is different for the two electrodes. Whereas for the FTO electrode, the residual signal consists of a single energy peak centered at a binding energy of -0.8 eV, a superposition of two peaks is apparent in the TiO_2 residual spectrum. This was inferred from a fit of experimental data to a sum of two Gaussian profiles. One of the peaks contributing to the TiO_2 spectrum lies at the same binding energy of -0.8 eV as the single peak of the N719/FTO residual spectrum. For both electrodes, the lifetime of this spectral component is nearly the same as the CC width (see Discussion below). It is therefore attributed to the short-lived ^{1}MLCT state directly populated by the pump beam. Another peak contributing to the N719/TiO_2 residual spectrum lies at a binding energy of -0.2 eV. It arises only in the spectra recorded for the sensitized TiO_2 electrode and, thus, manifests the specific interaction between the dye and the CB of semiconductor. Hence, this peak is denoted by CB of TiO_2.

Since the CB peak is not apparent for the FTO electrode, it can be concluded that the ^{1}MLCT → CB injection is weak and can be neglected. The weakness of this transition is a consequence of the specific electronic coupling at the N719/FTO interface. This is in accordance with the results of previous studies, where electron injection was found to be much slower for nano colloidal SnO_2 compared to TiO_2[16,195,196] It was argued that a possible reason could be the much lower density of acceptor states of the FTO conduction band resulting in a smaller probability for a fast and direct electron transfer process. Considering the competing ultrafast relaxation channel to the triplet state, the total yield of electrons injected from the ^{1}MLCT state is therefore highly suppressed.

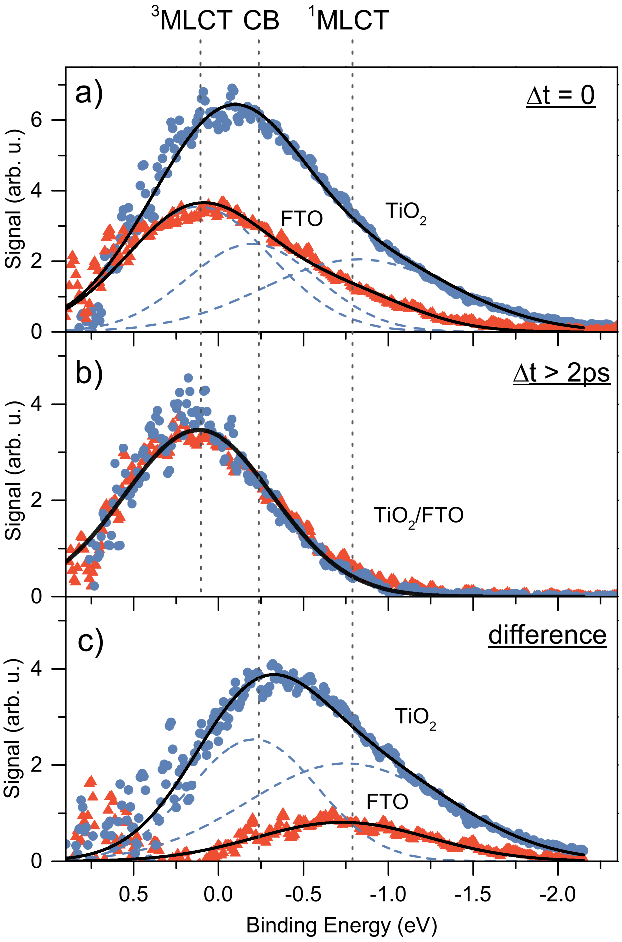

Fig. 4.8 Transient energy spectra of photoelectrons emitted from sensitized TiO_2 (circles) and FTO (triangles) samples at (a) zero time delay and (b) at time delays larger than 2 ps. The panel (c) shows the difference between spectra in (a) and (b). Vertical lines indicate positions of the energy peaks attributed to ionization of the ^{1}MLCT, ^{3}MLCT, and CB states. The individual contributions from the ^{1}MLCT and CB states to the TiO_2 spectrum are shown by dashed lines. Solid lines show results of superposition of the corresponding number of energy peaks: ^{1}MLCT, ^{3}MLCT, and CB peaks in (a); ^{3}MLCT peak in (b); ^{1}MLCT and CB peaks in (c).

The measurement indicates that the energy level of the ^{1}MLCT state lies 0.7 eV above the conduction band edge. Such a driving force is preferable for ultrafast injection. It is important to note that although a pump photon energy of 2.3 eV is applied, the energy difference between the center of the HOMO band and the ^{1}MLCT state is found to be 3.0 eV. This means that the transition amplitude is larger for excitation on the higher-energy side of the HOMO band. As it is known from the theory this part is comprised mainly of the Ruthenium t_{2g} orbital.

The energy positions of the ^{1}MLCT, ^{3}MLCT, and CB peaks identified in Fig. 4.8 were found to be independent of the time delay. Therefore, for each time delay the transient spectra could be fitted to a sum of Gaussian profiles with fixed central energies. A sum of three and two profiles were used for fitting the TiO_2 and FTO data, respectively. Using this routine, the integrated transient yield shown in Fig. 4.7 could be decomposed into its fast and slow individual components. The results of this decomposition are shown in Fig. 4.9 for the TiO_2 (left panel) and FTO (right panel) electrodes, respectively. Because of the small energy difference between the ^{3}MLCT and CB peaks for TiO_2, the fit could not provide reliable amplitudes of their individual contributions. Instead, the transient signal for the TiO_2 electrode was decomposed into a contribution of the ^{1}MLCT peak and a combined contribution of the ^{3}MLCT and CB peaks. For both electrodes, the transient ^{1}MLCT signal has almost the same shape as the CC trace. This means that the lifetime of the ^{1}MLCT state is smaller than the experimental temporal resolution of 98 fs. The transient ^{3}MLCT signal on the other hand exhibits a sharp increase at small time delays followed by a slow decay on a picosecond scale (see the decomposition results for the FTO electrode in the right panel of Fig. 4.9). However, the combined transient signal of ^{3}MLCT and CB of TiO_2 reveals an additional decay time constant. This decay, associated with the electron dynamics in the CB of TiO_2, is faster than the decay of the ^{3}MLCT state. This important issue is discussed in more detail below.

4.1.5 Injection Kinetics

The results of the spectral decomposition of the transient signal were used to describe the electron dynamics at the dye-semiconductor interface and to derive the time constants of involved electronic transitions. For this purpose, the two-state injection model proposed by Asbury et al. [179,181]. was adapted and is schematically depicted at the left side in Fig. 4.10. In this model, the initially populated non thermalized ^{1}MLCT state can either inject electrons to TiO_2 with a rate k_1 or decay to the ^{3}MLCT state with a rate k_2. The decay rate k_2 is determined by intersystem crossing, followed by thermalization of the triplet state. A direct excitation of the ^{3}MLCT state from the ground state of dye was found to be improbable at the pump wavelength of 530 nm [176]. The ^{3}MLCT state can inject electrons to TiO_2 with a rate k_3. In the transient spectra, however, the spectral component associated

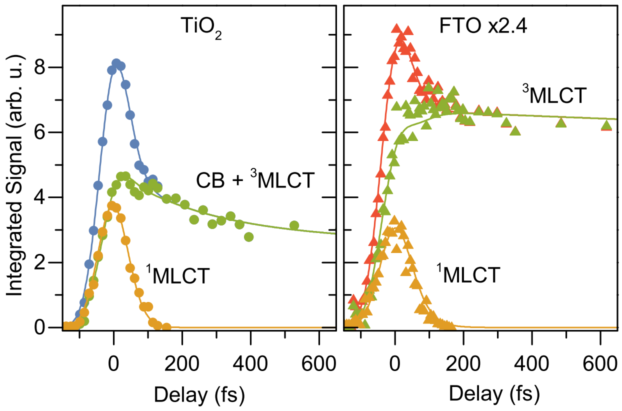

Fig. 4.9 Spectral decomposition of the transient signal shown in Fig.4.7. Left: TiO_2 signal is decomposed into the ^{1}MLCT contribution (yellow) and the combined contribution of ^{3}MLCT and CB states (green). Right panel: FTO signal is decomposed into the ^{1}MLCT (yellow) and ^{3}MLCT (green) contributions. The FTO signal is multiplied by the factor 2.4 to account for the different surface coverage. The solid lines represent fits to the transient signals.

with electrons injected to the CB from the triplet state is not distinguished. Therefore, in the analysis only the transient yield of injection from the singlet state, derived from the spectral decomposition procedure, is considered. The recombination to the ground state of the dye was reported to occur on a microsecond to millisecond time scale [197]. Since this is a by orders of magnitude slower process compared to the injection channels, it is disregarded in in the subsequent consideration. Dissipation of the injected electrons is described by a rate constant k_4. The origin of this decay will be discussed below. The electron dynamics at the N719/FTO interface (right side of Fig. 4.10) are treated in a similar fashion, except that the ^{1}MLCT → CB transition is not considered for the reasons discussed above.

The initial state from which excitation takes place (denoted as ground state, GS) is depicted on the slope of the Gaussian profile representing the HOMO band illustrating that the transition amplitude is larger for excitation on the higher-energy side. The electron population dynamics at the N719/TiO_2 interface can be described by the system of differential equations:

$$\begin{aligned} \dot{n}_S &= -(k_1 + k_2)n_S + P(t), \\ \dot{n}_T &= k_2 n_S - k_3 n_T, \\ \dot{n}_{CB} &= k_1 n_S - k_4 n_{CB}, \end{aligned} \tag{4.1}$$

where $n_{\mathrm{S,T,CB}}$ denote the populations of the ^{1}MLCT, ^{3}MLCT, and CB states, respectively, and P(t) describes the time-dependent population rate of the ^{1}MLCT state with the actual temporal envelope of the pump pulse taken into account. One should stress again that n_{CB}

describes the CB state populated via injection from the ^{1}MLCT state and, thus, the rate constant k_3 is not involved in the third line of Eq. 4.1.

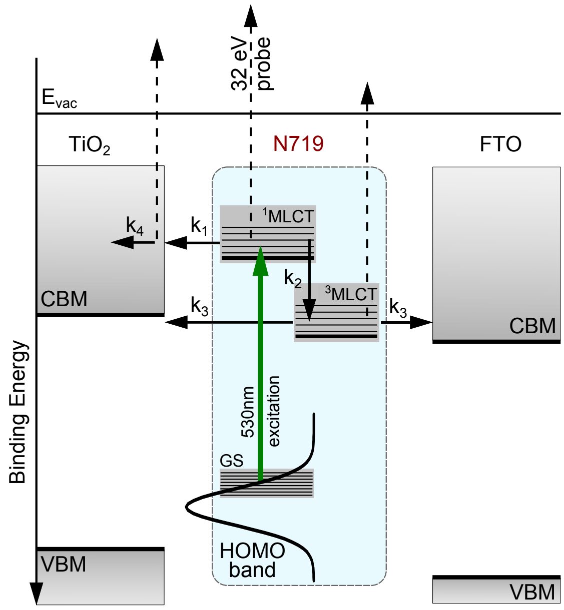

Fig. 4.10 Injection model for TiO$_2$ (left side) and FTO (right side). The vertical axis represents the energy scale. The energy positions of the ground (GS) and excited singlet and triplet MLCT states of the dye are shown together with the energy levels of the minimum CB energy (CBM) and the maximum valence band energy (VBM) for TiO$_2$ and FTO. The HOMO band of the dye is depicted by a Gaussian profile. The solid vertical arrow indicates the photoexcitation transition at the 530 nm wavelength. Dashed arrows indicate XUV ionization transitions. $k_{1,2,3,4}$ denote rates of population and decay transitions considered in the model (see text).

It is instructive to consider first the solution of Eq. 4.1 in the limit of long time delays, $t \gg \tau_{\mathrm{CC}}$, where the population $n_{\mathrm{T}}(t)$ of the triplet ^{3}MLCT state constitutes the transient signal. Here τ_{CC} represents the CC width. In this limit, the term $P(t)$ becomes negligibly small and the solution for $n_{\mathrm{T}}(t)$ can be found analytically. Taking into account that $k_3 \ll k_1, k_2$, one obtains

$$n\,(t) \propto \frac{k_2}{k_1 + k_2 - k_3} \exp\left(-k_3 t\right) \tag{4.2}$$

The same equation describes the population dynamics of the ^{3}MLCT state at the N719/FTO interface in the limit of long time delays. In this case, the rate k_1 should be neglected, $k_1 = 0$, since injection from the ^{1}MLCT state to FTO is excluded. One should note again that the decay rate k_3 of the ^{3}MLCT state is found to be the same for both TiO$_2$ and FTO electrodes. It means that in the asymptotic time limit the ratio of populations of the triplet state at the two interfaces is constant, $n_{\mathrm{T,FTO}}(t)/n_{\mathrm{T,TiO_2}}(t) = A$ $(t \to +\infty)$. Using the inequality $k_3 \ll k_1, k_2$, from Eq. 4.2 one ends up in

$$\frac{k_1}{k_2} = A - 1 \tag{4.3}$$

For the value A = 2.4 obtained from the experimental data, we find that the ratio of the competing injection and relaxation rates of the ^{1}MLCT state at the N719/TiO$_2$ interface is $k_1/k_2 = 1.4$. Thus, the injection rate into the CB is higher than the decay rate. This finding is in good agreement with the previously reported ratio of 1.5 [182]. This further supports the approximation made in the used model, where the injection channel from the ^{1}MLCT state into FTO is neglected.

At shorter time delays, the temporal envelopes of the pump and probe pulses need to be taken into account to reproduce the experimental results. In this case, the system of rate equations in Eq. 4.1 was solved numerically with the initial condition that all involved states were unpopulated at $t \to -\infty$. The ionization signal from the ^{1}MLCT, ^{3}MLCT and CB states was calculated by convolution of $n_{\mathrm{S}}(t)$, $n_{\mathrm{T}}(t)$ and $n_{\mathrm{CB}}(t)$ with the temporal envelope of the probe pulse, assuming that the probe step is non-saturated. A Gaussian envelope was assumed for both pump and probe pulses, with a constrain that their convolution yields the measured CC trace. The numerical results were fitted to the spectrally decomposed experimental data shown in Fig. 4.9, with rates $k_{1,2,3,4}$ being as fit parameters. The fit routine was applied to reproduce simultaneously the data sets obtained for both electrodes. In order to account for the CC signal from the bare substrates, a CC trace centered at time zero was added to the fit function and its amplitude was considered as an independent fit parameter.

Table 4.1 Population (τ_p) and decay (τ_d) time constants of the ^{1}MLCT, ^{3}MLCT, and CB states obtained from the modeling of the electron dynamics with the use of Eq. (4.1). The values obtained in the present work are given in comparison with previously reported results. The binding energies (E_b) of the states and their widths (ΔE_b) are also presented.

State	E_b (eV)	ΔE_b(eV)	τ_p	τ_d
^{1}MLCT	−0.8	1.0	–	(20 ± 10) fs
			–	30 fs [182]
			–	(30 ± 3) fs [181]
CB	−0.2	0.6	(50 ± 20) fs	(250 ± 30) fs
			(50 ± 6) fs [182]	–
			$<$ 100 fs [179]	–
^{3}MLCT	0.1	0.8	(30 ± 20) fs	(15 ± 2) ps
			(75 ± 10) fs [182]	–
			(80 ± 5) fs [181]	–
			$<$ 100 fs [179]	–
HOMO band	2.2	0.6	–	–

Table 4.1 summarizes the results obtained from the simulation of the population and relaxation electron dynamics at the N719/TiO_2 and N719/FTO interfaces. Here the population and the decay time constants represent inverse values of the corresponding transition rates; except for the decay of the ^{1}MLCT state, the time constant is represented by $1/(k_1 + k_2)$. The rather large error bars of the ^{3}MLCT and CB population time constants are due to the limited time resolution in the experiment. It prevents derivation of a convincing value of k_1/k_2 from the early time dynamics simulation. The τ_p value of 50 fs obtained for the ^{1}MLCT → CB transition is in a good agreement with the previously reported results [177,182], though the population rate of the triplet state seems to be overestimated in the simulation. This is most probably due to the presence of the CC signal in the transient spectra which spectrally overlaps with the signal from the triplet state. The ^{1}MLCT state lifetime of 20±10 fs could also be derived by considering the minor broadening of the spectrally separated ^{1}MLCT component (see Fig. 4.9) as compared to the CC trace. This lifetime is in agreement with the literature value of 30 fs [177,182]. The injection rate k_3 is found to yield the lifetime of 15 ps for the ^{3}MLCT state at both interfaces. In a previous investigation focusing on the injection kinetics from the ^{3}MLCT state, it was shown that injection takes place on equal timescales at both interfaces and is controlled by a similar electronic coupling mechanism [176]. Multi-exponential kinetics were measured ranging from several picoseconds up to 100 ps and are in agreement with the findings presented here[176,181].

The ultrafast populated CB peak exhibits a decay constant on the order of 250 fs. Since this signal is due to electrons located at the semiconductor site, the decay mechanism needs to be related to the CB properties. To date, results of studies on the carrier relaxation dynamics in TiO_2 are sparsely presented in literature. By using the method of transient absorption spectroscopy, Tamaki et al. [198] reported on the capture of free electrons into trap states at the semiconductor surface, occurring on a timescale of 200 fs. Such a dissipation mechanism could be particularly efficient in the present experiment due to the enlarged surface area of the substrate. A similar decay time constant of 300 fs was inferred from the measurements of carrier mobility with the use of time-resolved terahertz spectroscopy [199]. An alternative dissipation mechanism could be the electron escape from the probed surface into the bulk. Indeed, photoelectron spectroscopy allows probing the electron population within a surface skin layer of a few angstroms thickness, and the escape mechanism could well-describe our observations. The kinetics of electron escape from surface was considered by Gundlach et al. [200], who applied time-resolved photoemission spectroscopy with a 10 fs time resolution to study heterogeneous charge transfer dynamics between catechol molecules adsorbed on a rutile TiO_2 substrate. It was found that the escape kinetics are characterized by an initial time constant below 10 fs, followed by a slower escape on a timescale of $50 - 100\ fs$ and, eventually, by a long-lived tail in a picosecond range. One should also note that the electron motion direction with respect to the surface plays an important role in the escape kinetics, as reported by Rego et al. [201] on the basis of quantum-dynamics calculations. It was predicted that an injected electron diffuses into the [101] bulk direction on a 100 fs timescale. Considering the random surface orientation of nanocolloidal particles used as the substrate in the present experiment, a good match between this value and the here reported time constant of the CB signal decay is found.

4.1.6 Conclusion

The HET process at the N719/TiO_2 interface was investigated by means of ultrafast photoelectron spectroscopy. In this first experiment it could be demonstrated that the technique is advantageous in revealing simultaneously both the injection kinetics at a dye-semiconductor interface and the energy structure of this complex system. The detailed knowledge about the band alignment between the donor and acceptor is of great importance for the efficient charge transfer. By using this method, the absolute binding energies of the excited states involved in the electron dynamics were for the first time directly determined. The ^{1}MLCT state is found to lie at 0.7 eV above the conduction band minimum, which gives rise to a strong driving force for injection from this state. The ultrafast injection to TiO_2 was confirmed to occur from the nonthermalized ^{1}MLCT state, whereas the injection yield from this state, although exhibiting equal binding energy, was found to be negligible for the FTO electrode. This outcome emphasizes the fact that beside the energetic band alignment between donor and acceptor states the electronic coupling and the density of states are important. The latter property is known to be favorable for the TiO_2 electrode. However, it cannot be excluded that the electronic coupling represents the determining cause already reflected in the appearance of slightly different ground state binding energies. It is important to note that the energy difference between the center of the HOMO band and the center of the ^{1}MLCT band is 3.0 eV, which is by 0.7 eV larger than the photon energy used throughout the experiment. This indicates that the HOMO band is composed of several orbitals where only the higher-energy states are involved in the charge transfer process.

The triplet state was found to lie 0.2 eV below the conduction band. Injection from the triplet state, thus, occurs only due to a partial energy overlap with the conduction band, leading to a slow kinetics of the electron transfer. The spectral decomposition of the transient emission signal allows the ultrafast population and decay dynamics of the excited states to be followed individually. For the N719/TiO_2 interface, contributions from the directly excited ^{1}MLCT state, the CB state of injected electrons, and the thermally relaxed ^{3}MLCT state were identified. By comparing results obtained for the N719/TiO_2 and N719/FTO interfaces, the kinetics of injected electrons at the CB site could be unambiguously revealed.

The time constants of the population and decay dynamics inferred in this study are in good agreement with the values reported in literature. Considering the dissipation of injected electrons at the CB site, both the electron trapping and the electron escape models could interpret the observations. Further investigations are needed to determine the probable dissipation mechanism. Here, time resolved investigation of the bare substrates with sufficient photon energy to directly lift electron into the CB could give probably answers. The detailed characterization of the two interfaces, presented in this section, serves as a basis for the subsequent investigations.

4.2 Charge Transfer Dynamics at Dye-Sensitized ZnO

Publication (2) reproduced in part from Scientific Reports, 2016, 6 (24422)

4.2.1 Motivation

As already pointed out in the previous section, TiO_2 based DSSCs were considered as a reference in the study of fundamental aspects of photo induced charge transfer over the last decades since they have shown solar-to-electric energy conversion efficiencies above 10%. However, Zinc oxide (ZnO) represents a promising alternative to TiO_2 due to its much higher bulk electron mobility [77,78] and great diversity in the nanostructured electrodes that can be produced [76,202], e.g., nanoparticles [79,80], nanorods [81] and nanosheets [82]. Though, the achieved energy conversion efficiencies of ZnO-based DSSCs are still much below the record values of their TiO_2-based counterparts[203]. This issue initiated a long-lasting discussion on the possible reasons. Ultrafast transient absorption spectroscopy has revealed that the injection kinetics in ZnO-based substrates occurs on a different, picosecond, timescale [16,70,195,204–209], whereas the charge separation at TiO_2 interfaces is by order of magnitudes faster and takes place in a femtosecond time domain [172,173,177,210]. The slower dynamic response is, therefore, often related to the limited performance of ZnO-based cells, but its physical origin is still not fully understood. Both semiconductors possess similar band gap and conduction band positions so that the energy level alignment cannot explain these findings. However, the electronic properties of the conduction band determine the coupling between the dye and the semiconductor and, thus, represent a critical factor for the injection process.

For the charge transfer at the TiO_2 interface, the well-established two-state injection model presented in the previous study is used to describe the coexistence of a dominant ultrafast (<100 fs) injection and one or more slower minor components occurring on a picosecond timescale [179]. The initially excited singlet metal-to-ligand charge-transfer-state (^{1}MLCT) directly injects electrons as free mobile charge carriers to the conduction band of TiO_2 on an ultrafast time scale. This process occurs simultaneously with a rapid intramolecular relaxation into the triplet ^{3}MLCT states via intersystem crossing on a similar timescale of 50-100 fs. The subsequent injection from the relaxed triplet state is significantly slower and takes place on a picosecond timescale. The slow injection from the ^{3}MLCT state was argued to be caused by an unfavorable energetic band alignment, where the donor states largely lie below the acceptor states and the electron transfer is possible only due to a partial overlap of the ^{3}MLCT band and the conduction band [211]. In contrast for ZnO, two competing descriptions have been proposed to account for the slow character of the injection kinetics. One mechanism is based on an adapted two-state injection model where the direct ultrafast electron transfer from the ^{1}MLCT is considered to be highly suppressed (see Fig. 4.11(a)). It follows that the majority of the injected electrons originates from the ^{3}MLCT state. This can be compared to the model used in case of the FTO interface in the previous investigation. In this representation, the retained electrons reside on the dye before they become free mobile charge carriers.

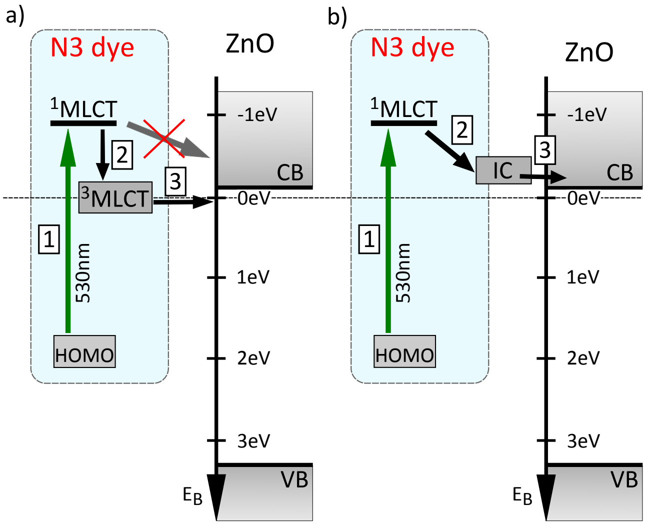

Fig. 4.11 Schematic representation of the two models describing the charge transfer to ZnO after initial photoexcitation (1) of the N3 dye to the ^{1}MLCT state. In (a) after internal relaxation (2) to the ^{3}MLCT state charge transfer (3) occurs on a ps timescale. The electron is retained at the dye molecule and the ultrafast direct injection from ^{1}MLCT, as compared to TiO_2, is suppressed. In (b) the transfer process is mediated by the formation of the interfacial complex (2) followed by slow (ps timescale) charge transfer (3). In this model, the electron is retained at the interface between the dye and the semiconductor.

A second completely different injection mechanism, consisting of the formation of an interfacial electron-cation complex (IC), was suggested on the basis of a variety of experimental results (see Fig. 4.11(b)). It was shown that an increase in the yield of positive dye cations is not necessary directly related to the release of mobile electrons [204,206]. Thus, the electrons are considered to be temporarily delayed at the dye-ZnO interface via the IC formation. The second description does not exclude an ultrafast depopulation of the ^{1}MLCT state via electron ejection from the dye but rather suggests a mechanism of the carrier-formation delay. The possible origin of the IC has been addressed before. Furube et al. [204] proposed that hybridization of the molecular excited states with the surface-localized ZnO states leads to the formation of a new state, called "exciplex", and further explained that this could be an electron-donor (D) and acceptor (A) pair occurring in a neutral (D*A) or ionic (D^+A^-) state. This consideration was further corroborated in Refs. [206,208], where the strong electrostatic interaction between the cations and injected electrons at the surface was argued to stabilize the intermediate state. Due to the lower electrostatic screening in ZnO as compared to TiO_2, such stabilization is more efficient in the former case, which might explain that the IC can be found only at the ZnO interface. For both competing descriptions shown in Fig. 4.11, the intermediate state is populated on a timescale well below 500 fs and has a lifetime in the picosecond domain.

So far, the involved transient states were probed indirectly by means of time-resolved absorption spectroscopy applied in different ranges of photon energy. However, the transient absorption signal in the visible and IR domain is rather difficult to interpret due to the co-existence of broad and overlapping absorption bands [195]. Time-resolved inner-shell photoelectron spectroscopy seems to be a promising approach to identify the suitable injection mechanism [212,213]. Here, core-level of the central Ru atom are used as a reporter to gain inside into the interfacial charge-transfer processes. A transient chemical shift of the Ru 3d line to higher binding energies was observed 500 fs after photoexcitation of the dye. From this finding it was concluded that the formation of an interfacial charge-transfer state is involved in the electron transfer process. A drawback of this approach is that the interpretation of the transient signals relies on the support from complex time-dependent theoretical modeling.

Therefore in this investigation, time-resolved photoelectron spectroscopy in the XUV energy range is applied to probe directly the population dynamics of the intermediate states and their binding energies. By comparing results obtained for TiO_2 and ZnO substrates, the unique properties of the latter interface are revealed. Similar to the previous experiment, N3 dye molecules are excited by an optical pump pulse, close to the absorption maximum of the dye ($\lambda \approx 530\ nm$), and the evolution of the excited system is followed by monitoring the transient changes in the electron kinetic energy spectra.

4.2.2 Sample Characterization

To characterize the samples ground state XUV photoelectron spectra were recorded for the bare and sensitized TiO_2 and ZnO substrates, without application of the pump beam and with equal acquisition times. The spectra taken in the range of binding energies of the semiconductor valence band and the N3-dye HOMO band are shown in Fig. 4.12. The energy positions of the higher-lying electronic structure components, which are important for the photo induced electron transfer at the dye-semiconductor interfaces, can be estimated from these measurements. The valence-band maxima of the non-sensitized substrates can be seen to lie at approximately the same binding energy of 3.3 eV. This confirms the previous findings from literature, but it has to be pointed out again that this procedure suffers from slight uncertainty [214]. By taking the optical band gap of 3.3 eV into account, one finds that for both substrates the conduction band minimum lies close to the Fermi level [71].

The right panel of Fig. 4.12 shows the spectra in the binding energy range encompassing the N3-dye HOMO band. The band shape appears to be very similar for both substrates and its maximum arises at a binding energy of 2.1 eV. This value is in agreement with the previously reported results for the N3-sensitized interfaces [215–217]. As for the N719 dye it is expected that the HOMO band is composed of different molecular orbitals. In order

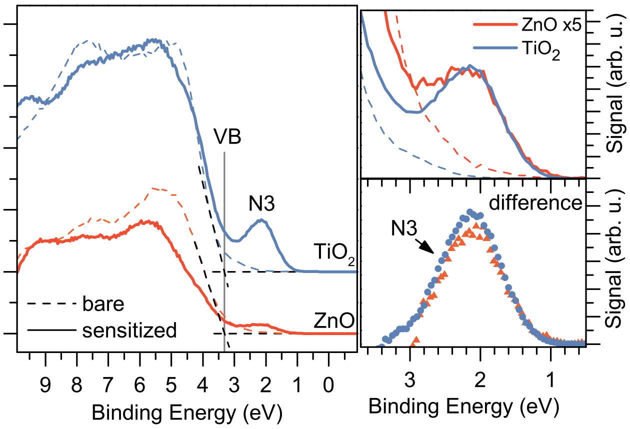

Fig. 4.12 Steady-state XUV spectra of photoelectrons recorded for the bare (dashed lines) and sensitized (solid lines) ZnO and TiO_2 samples. The emission peak from the dye ground state and the valence band maxiumum are labeled by N3 and VB, respectively. (Right) The upper panel shows in detail the ionization contribution from the N3 HOMO band on both substrates. The signal for the bare and sensitized ZnO electrode was multiplied by a factor of five. The lower panel shows the difference in the emission yield between the sensitized and bare substrates for ZnO and TiO_2, respectively.

to obtain an equal ionization yield of the dye on both substrates, the signal from ZnO/N3 interface was multiplied by a factor of five on the right panel in Fig. 4.12. Since the ionization cross section of N3 is expected to be the same, this implies that TiO_2 and ZnO substrates exhibit different surface coverage, which can be easily explained by a difference in the surface morphology and sensitization time.

4.2.3 Sample Damage at the Semiconductor Substrates

Irreversible sample damage can occur when a light-sensitive target is illuminated by a short laser pulse of high peak intensity. Even with low photon energies being below the ionization threshold multiphoton processes can take place leading to bond breaking reactions and chemical modification of the molecular structure of the dye and the semiconductor crystal structure. This issue is even more important when XUV radiation is applied, giving rise to a high direct ionization efficiency. Since solid state samples were analyzed without any refresh between the single laser pulses a sample-damage analysis was carried out. Different aspects were examined in this context. If any degradation is detected the timescale on which the spectral change occurs has to be considerably long compared to a single measurement event. Because the transient signal is exceedingly small compared to the stationary contribution a valid background subtraction is only possible if it appears constant within a single measurement period. For the time resolved experiments that means at least one complete cycle of delay time scans with duration of about 30 minutes. Further it has to be ensured that the radiation damage does not influence the electron transfer reaction under investigation. Finally the impact of the pump and probe beam is analyzed individually. The results presented in the following were obtained for the N3/ZnO interface. However, similar behavior was observed on all other used semiconductor substrates (TiO_2 and FTO) as well as for the N719 dye and are not shown in detail here. Figure 4.13 (a) and (b) demonstrates the spectral change for the bare bZnO and the sensitized N3/ZnO samples, respectively, after their exposure to the XUV beam for 10 hours.

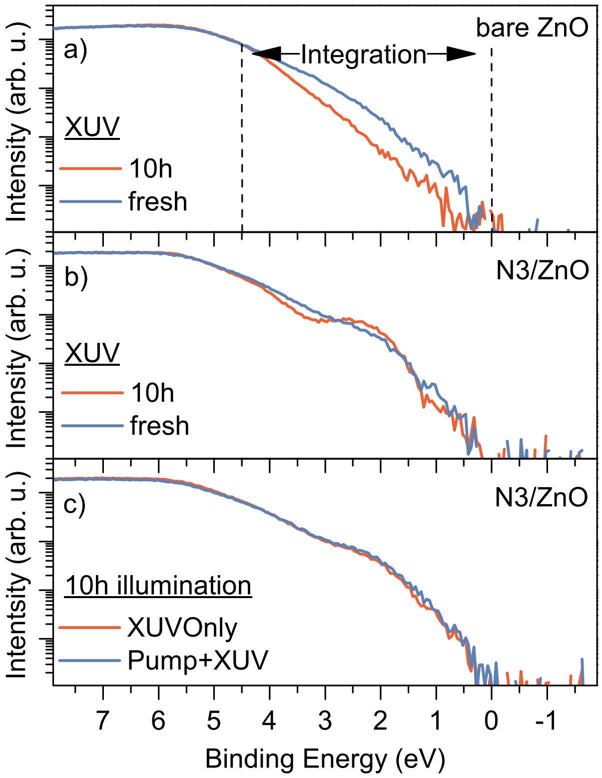

Fig. 4.13 Steady-state XUV spectra of the bare ZnO (a) and sensitized N3/ZnO (b) samples, obtained in the beginning of the exposure to solely the XUV beam (blue line, fresh) and after an exposure time of 10 hours (red line, 10h). Panel (c): Comparison of spectra obtained by 10h XUVonly (red line) and with additional pump beam applied (blue line).

In both cases changes in the XUV spectra are visible. Important to note is use of the logarithmic scale to emphasize the signal over the range of binding energies between 4.5 and 0 eV. This range encompasses the ionization contributions from the HOMO band of N3 and is relevant for the analysis of the transient signal. To quantify the damage effect as a function of time and to disentangle the individual changes of the substrate and the dye, the photoemission yield in both bZnO and N3/ZnO spectra was integrated over this range of binding energies (see Fig. 4.14(a)). One can see from Fig. 4.14(a) that the integrated yield obtained for bZnO is monotonically increasing, whereas for the sensitized sample the dependency appears to be more complex due to a superposition of yields arising from the bare substrate and the dye. Assuming a linear superposition of the yields, the difference between the two dependences demonstrates the change in the HOMO band signal related to a degradation of the dye (see green line in Fig. 4.14(a)). On the basis of this result we limited the maximum exposure time of an individual sample spot to 4 hours, corresponding to 10% decrease of the dyes signal.

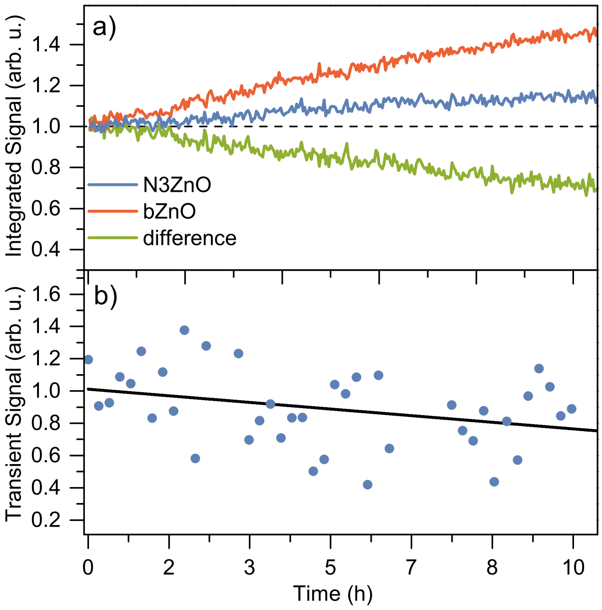

Fig. 4.14 Ionization yield integrated over the range of binding energies between 4.5eV to 0 eV as a function of the XUV exposure time. The red and blue lines show the yields for the bare and the sensitized samples, respectively, and the green line shows the yield difference. In b) the normalized amplitude of the transient signal for N3/ZnO as a function of the exposure time is shown.

The same degradation study was carried out when the pump beam was additionally applied. The result is shown in Fig. 4.13(c). In this case no additional spectral changes were observed, which implies that sample degradation was caused mainly by the XUV probe beam. From literature it is known that the Ru dye complexes possess high photo stability and can sustain more than 10^7 turnovers without significant decomposition [61].

In addition, the amplitude of the transient signal for N3/ZnO was recorded during the same time span of 10 hours. The normalized amplitude as a function of the exposure time is shown in Fig. 4.14(b). One can see that the decrease in the transient signal is comparable to the decrease in the steady-state photoemission yield of N3 shown in Fig. 4.14(a). This finding indicates that the degradation of the dye induced by the XUV beam is directly related to a decrease of active dye involved in the electron transfer process. A faster decrease of the transient signal would indicate additional degradation effects that cannot be monitored by the steady-state photoemission yield of N3 ground state. As already mentioned before, the measurement of the transient signal is divided into single cycles of delay time scans (called series hereafter). Before the transient signals were combined a comparison between the series was done. However, the shape of the transient signal associated with the injection kinetics were found to be unaffected by the sample degradation.

4.2.4 Time-resolved Signals

An overview of the transient photoemission signal recorded for both sensitized interfaces with the use of the WAM is shown in Fig. 4.15 in form of color maps. In both cases an asymmetric signal is visible. However, since the signals noise ratio is weak it is difficult to draw any other conclusions from this. Most distinct is the much broader contribution of the long lived state in case of ZnO. To gain better insight into the transient data cross-sections along the time and energy dimension were examined.

Figure 4.16 shows the time domain were the electron yield is integrated over the range of binding energies between -2 and 1 eV in the background-subtracted XUV spectra. This range lies above the HOMO band of N3 and encompasses the ionization contributions from transient states excited by the pump beam. Again, pump-probe spectra recorded at negative time delays were used as a background in the subtraction routine. Both transients shown in Fig. 4.16 were obtained by applying the same pump intensity and their maxima were normalized to unity. A comparison of the two dependencies reveals a more complex population dynamics of transient states at the TiO_2/N3 interface, manifesting a diverse injection mechanism as compared to ZnO/N3. Although the decay is multi-exponential in both cases, the initial fast component is not as pronounced for ZnO/N3. The different ratio between the fast and slow decay components for the two samples was already reported in literature [208].

In order to characterize the decay dynamics, the time dependence of the transient signal was fitted to a sum of exponential functions, convoluted with a Gaussian profile of 105 fs width representing the system response. The aim of the fit is not to determine precisely the lifetimes of the involved states but rather qualitatively compare both samples. A sum of two and three exponential functions was needed to reproduce results obtained for ZnO/N3 and TiO_2/N3 interfaces, respectively. In case of TiO_2, the fastest decay process is characterized by a lifetime constant of (35 ± 20) fs. This process is not apparent in the ZnO transient. Notably, after this ultra-fast component, a similar time dependence of the transient states population is observed for both systems, i.e., two exponential decay processes; one with a half-life of hundreds of fs and the other slower process with a lifetime $>$50 ps. The ps time constant was obtained in the data with a much larger time frame and is not shown here. The transient signal confirms the assumption of an ultrafast formation of the intermediate state within 500 fs after interaction with a short pump pulse and is found to be in agreement with the literature values [204]. Therefore, any further analysis of the binding energies of transient states is concentrated on pump-probe time delays after the intermediate formation

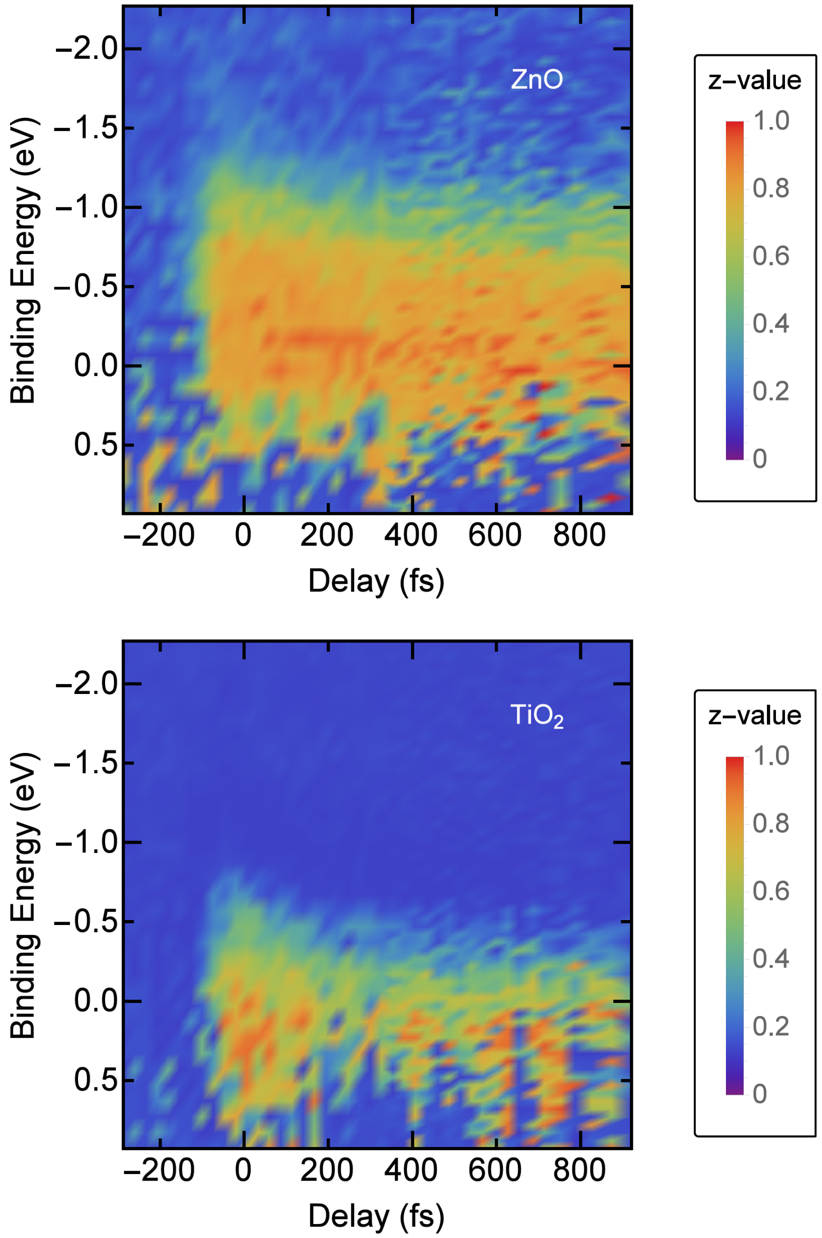

Fig. 4.15 2D color maps of the background-subtracted transient signal obtained at on the sensitized ZnO (upper panel) and TiO_2 (lower panel) substrates. The same color scale is used in both representations. The signal was recorded with identical integration time and pump intensity.

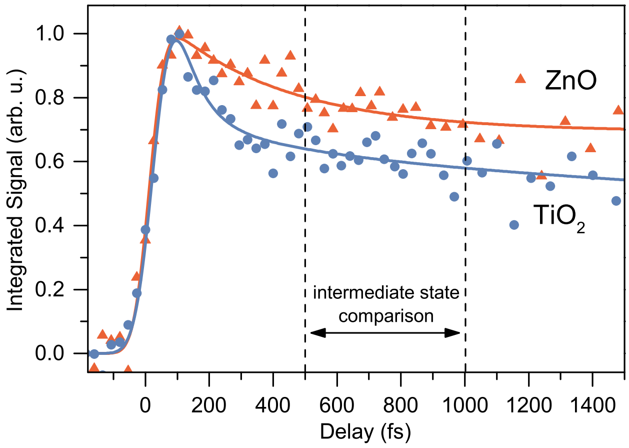

Fig. 4.16 Transient signal of the sensitized ZnO and TiO_2 substrates. Dependence of integrated electron yield of the background-subtracted XUV spectra on the pump-probe time delay. The solid lines represent results of fit to a sum of exponential functions convoluted with the system response function (see text).

is completed. The used interval of pump probe delays between 0.5 and 1 ps is assigned in Fig. 4.16. To gain a better signal-to-noise ratio, the transient XUV spectra were averaged over this range of delays.

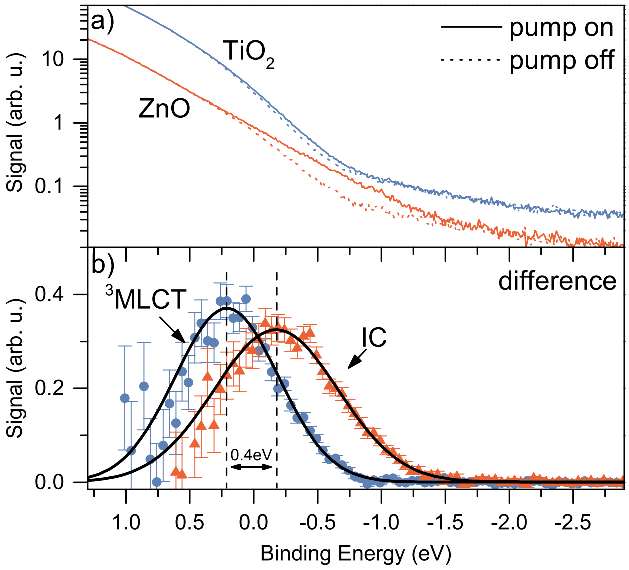

Fig. 4.17 Transient signal of the sensitized ZnO and TiO_2 substrates. (a) Transient spectra averaged over pump-probe time delays between 0.5 to 1.0 ps (pump on) compared to the background steady-state spectra (pump off). (b) Difference of pump-on and pump-off spectra for both samples

Figure 4.17(a) shows the delay-averaged XUV spectra for both substrates as well as the corresponding background spectra obtained without applying the pump beam. The background-subtracted kinetic energy distributions are presented in Fig. 4.17(b). One can see that in the given range of time delays ionization from a single band constitutes the transient photoemission yield for both interfaces. However, the binding energies of the transient states are rather different and lie at (0.2 ± 0.1) eV and (-0.2 ± 0.1) eV for TiO_2/N3 and ZnO/N3, respectively. The large energy shift of 0.4 eV indicates that the origin of the states is different. If the intermediate state of ZnO/N3 would be the ^{3}MLCT state, as in the case of the TiO_2/N3 interface, one should expect equal binding energies of the transient states in the 0.5-1 ps range of time delays, as it was found in the previous investigation on the injection kinetics of TiO_2 and SnO_2 electrodes sensitized with the closely related N719 dye (see section 4.2) (N719 is the doubly deprotonated version of N3). There it was demonstrated that the longer lived transient states of both TiO_2 and SnO_2 substrates possess very similar binding energies and spectral bandwidths. Supported by numerical modeling of the transient signal, it was concluded that the slow injection pathway resulted from the ^{3}MLCT state. The binding energy of 0.1 eV of the ^{3}MLCT state for the TiO_2/N719 interface is reproduced within the error estimate in the present measurement conducted on the TiO_2/N3 interface. This finding indicated that the injection kinetics on ZnO/N3 can not be described by the two-state model used for TiO_2/N3. Thus, one can conclude that the electron dynamics at the ZnO/N3 interface involves the formation of an interfacial electron-cation complex. The formation of this different state is further supported by the fact that the intermediate state of ZnO/N3 exhibits a larger spectral bandwidth of 1.1 eV, as compared to a bandwidth of 0.8 eV for the TiO_2/N3 transient. These values were obtained by deconvolution of the apparatus response function from the energy dependences shown in Fig. 4.17(b). A possible reason of the difference in bandwidth could be a more delocalized character of the interfacial complex as compared to the molecular electronic state. The results provide direct evidence that for ZnO a different charge transfer mechanism is involved in the electron injection process, as compared to TiO_2 and SnO_2. This issue was raised previously by Stockwell et al. [208].

Most important is that the dye-semiconductor electronic coupling can be in particular the limiting fact for the charge transfer and must be taken into consideration in addition to the energy level alignment when rationalizing the electronic properties of dye-semiconductor interfaces. Indeed, the energetic position of the long-lived transient state of ZnO/N3 lies well above the conduction band minimum. Despite this alignment being more favorable for fast electron injection, the experimentally measured rate of injection was much slower. Previous argumentation in terms of the low density of acceptor states, used to explain the slow injection from the relaxed excited donor states near the conduction band edge of TiO_2 might therefore be questionable.

Since the intersystem crossing of the N3 dye has been found to occur on a time scale of 100 fs [181,182] and we do not observe a signature of the ^{3}MLCT state formation, we conclude that the IC formation has to be considerably faster than 100 fs. A similar conclusion was drawn on the basis of transient absorption measurements by Furube et al. [204] as well as with the use of time-resolved inner-shell photoelectron spectroscopy by Siefermann et al. [213]. However, a much higher time resolution is required to reveal the IC formation dynamics in greater detail. As mentioned before, the long-lived character of the intermediate state was considered to be the reason for the poor performance of the ZnO-based DSSCs. However, it was shown previously that the injection rate at the TiO_2 surface can also dramatically decrease to similar values in the presence of an electrolyte, while still yielding high device efficiency [218,219]. Therefore, the lifetime of the intermediate state as well as the rate at which the dye returns to the ground state (recombination) are both crucial factors determining the overall electron transfer probability to the semiconductor. Presumably, the different electronic coupling of the ZnO/N3 interfacial state with the ground N3 molecular state leads to an increased recombination rate, resulting in a smaller electron-transfer efficiency. This is in accordance with the conclusion drawn by Sundström and co-workers [206] who found likewise the cause of a lowered device efficiency of ZnO-based solar cells in an increased recombination rate.

4.2.5 Conclusion

The heterogeneous electron transfer from the N3 dye complex to the ZnO surface was investigated. The time and energy dependent population of donor and acceptor states at the interface were probed by means of ultrashort XUV pulses. A comparison between the previously analyzed TiO_2 and ZnO revealed the latter's specific properties. With this approach direct evidence of the formation of interfacial electronic states at the dye-sensitized ZnO interface could be provided. This feature of ZnO, in comparison to other materials such as TiO_2 and SnO_2, gives rise to a specific electronic coupling which governs the charge transfer process at ZnO electrodes. The ultrafast formation of the intermediate state was confirmed being the origin of the delayed release of free charges at N3/ZnO interface. Only the coupling of these states to the ZnO bulk states determines the rate of free electron generation. This finding shows that ZnO bulk properties such as the conduction band density of states are less significant for the electron transfer process than what is commonly assumed. Particularly notable is, that the energetic band alignment at the ZnO interface was found to be more favorable compared to TiO_2. Since electron injection in ZnO lags behind the other substrates the electronic coupling between donor and acceptor states appears to be of major importance. This fact has to be considered with regard to potential further improvements in the performance of ZnO-based DSSCs which may be achievable by means of a better control of the surface chemistry of ZnO. New designs capable of reducing such detrimental effects of delayed charge formation at the ZnO interfaces should be focused on this issue. Beside the insights with respect to the charge transfer dynamics the here developed method of transient XUV photoelectron spectroscopy has demonstrated to be a powerful tool in revealing both - the ultrafast electron dynamics at interfaces and the absolute binding energies of the involved states. The latter capability makes it advantageous in comparison with other developed techniques such as transient absorption spectroscopy in the near-infrared or terahertz regime. Due to its high surface sensitivity, PES is able to provide valuable insights into the charge transfer dynamics at dye-semiconductor interfaces.

4.3 Excited States Dynamics of $[Ru(bpy)_3]^{2+}$ Dissolved in Ionic Liquids

Publication (1) Phys. Chem. Chem. Phys., 2016, 18 (28893-28900) - Reproduced by permission of the PCCP Owner Societies

4.3.1 Motivation

Room-temperature ionic liquids (ILs) have been extensively investigated as promising new materials for numerous applications [86–88]. The attractiveness of this material class stems from their manifold of interesting physico-chemical properties [90,92,95,220] such as the liquid state over a wide range of temperatures, the chemical inertness, high ionic conductivity and very low vapor pressures [103,221]. The latter makes ILs perfectly suitable for examination under UHV conditions required for many surface sensitive techniques. Among those photoelectron spectroscopy (PES) represents one of the most powerful methods to study the IL-vacuum interface and has been proven to provide unique data on the near surface composition, chemical state identification and the valence band structure [222–227]. Most of the investigations were primarily focused on the IL samples themselves whereas the use of ILs as solvents opens up a range of exciting new experimental possibilities to study isolated molecules and complexes in solutions via this UHV technique [228–232].

In this section the excited states dynamics of the Ruthenium transition metal complex $[Ru(bpy)_3]^{2+}$ dissolved in the IL 1-Ethyl-3-methylimidazolium trifluoromethanesulfonate [EMIM][TfO] are examined. The molecules excited state properties have already been intensively studied by other spectroscopic methods [46–50]. It was therefore chosen as a prototype for this class of compounds and depicts a model system for studying intramolecular electron transfer reactions. Here, femtosecond time-resolved PES in the spectral XUV range is applied and the methods capabilities in both - revealing the intramolecular relaxation kinetics and determining the binding energies of the involved states are demonstrated. For this purpose the process of high-order harmonic generation [14,233] (HHG) is utilized to achieve the necessary photon energy of up to 40 eV and a high temporal resolution, which enables to probe the ground as well as the excited states simultaneously on an ultrafast timescale. To the best of our knowledge, there has been no attempt reported about the usage of ILs as a solvent in a PES experiment to investigate solutes energetics and dynamic behavior. It can therefore be seen as a first benchmark to explore the advantages of the spectroscopic method in this field and to answer important scientific questions about the IL/solute interaction.

The study is organized as follows. At first, the steady state characteristics of the bare IL are presented, including the valence PES spectrum as well as its stability under continuous XUV illumination. Subsequently the solutes appearance dissolved in [EMIM][TfO] is characterized and its frontier molecular orbitals are addressed. A concentration of 100 mM $[\mathrm{Ru(bpy)_3}]^{2+}$ is used being close to the solubility limit. The main part of this investigation presents the analysis of the transient signal obtained by applying of a pump beam of 480 nm wavelength. The findings are compared to the previously reported description of the photo-cycle and the correlation between the solute and its IL environment is discussed.

4.3.2 Steady State Spectrum of the bare IL

The energy structure of the valence band of [EMIM][TfO] is inferred from the steady-state XUV spectrum shown in Fig. 4.18, recorded with the use of the 21st harmonic (32 eV photon energy) and without application of the pump beam.

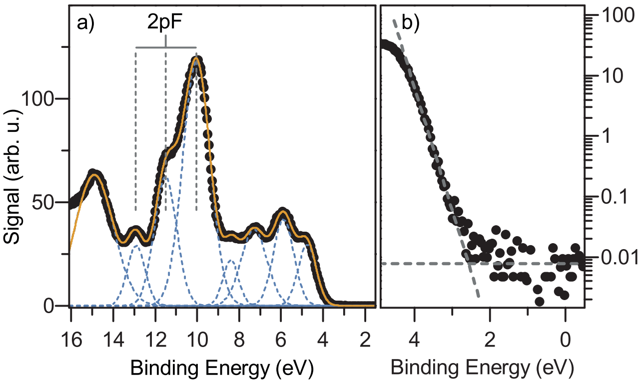

Fig. 4.18 Steady state spectrum of the bare [EMIM][TfO]. Panel a) shows the entire XUV spectrum. The contributions of individual peaks are shown by Gaussian profiles (dashed lines) obtained from the fit. The pronounced contributions of the fluorine 2p orbital of the anion $\mathrm{TfO^-}$ are indicated. In panel b) the spectral range of the highest occupied orbitals is shown in greater detail.

The spectrum exhibits pronounced peaks that were fitted to Gaussian contributions (see dashed lines). Previously reported DFT calculations enable the identification and assignment of specific spectral features [223,227]. The three peaks at 10.0, 11.5, and 14.9 eV binding energies can be clearly attributed to the fluorine 2p orbital of the $\mathrm{TfO^-}$ anion. The peak with the highest amplitude, lying at 10.0 eV, was chosen as a reference to calibrate the binding energy scale according to the corresponding literature value from Refs. [224,227]. A direct determination of the absolute binding energy scale, e.g. by measuring a metal Fermi edge, causes problems due to the space charge effect. It originates from the accumulation of positive charges at the IL surface because of the reduced electric conductivity of the sample. This effect is identical to the one described previously induced by intense pump pulse ionization. The energy calibration in previous studies was commonly accomplished by referencing the spectra to the aliphatic carbon 1s state with a binding energy of 285.0 eV [226]. Since the reference core states are not accessible by means of the XUV photon energy used throughout this investigation, the above mentioned peak of $\mathrm{TfO^-}$ was chosen here as the reference.

The peaks in the range of binding energies between 4 and 9 eV cannot be clearly associated neither to the anion nor cation states [234]. However, the ionization potential of the solvent, given by the minimum amount of energy required to remove an electron from the solvent molecules, represents an important characteristic. A large ionization potential is preferable, so that an overlap with the solutes HOMO is avoided leading to a better resolution of the solute spectral contributions and higher signal to noise ratio. Figure 4.18(b) shows the magnified spectral range of the highest occupied orbitals of [EMIM][TfO]. The onset of the occupied states is determined by the crossing point of the horizontal line representing the noise level with the straight line describing the slope of the HOMO energy peak in the [EMIM][TfO] spectrum. Differently from the analysis of valence band maxima applied in the studies on semiconductors, a logarithmic scale is used here to determine the binding energy onset of occupied states. By means of this procedure an energy onset value of 2.6 eV was found. This value has to be considered when analyzing the HOMO level position of the dye, as discussed in the following part.

4.3.3 Steady State Spectrum of $[Ru(bpy)_3]^{2+}$ Dissolved in IL

The steady state spectrum of the $[Ru(bpy)_3]^{2+}$ complex dissolved in [EMIM][TfO] was recorded under similar experimental conditions as for the previously shown bare solvent. A comparison between both measurements is presented in Fig. 4.19. For a better visibility of the solute contributions, the difference between the two steady state spectra is shown on the right side.

The contribution of the HOMO band of the dye to the spectrum is apparent at a binding energy of 2.3 eV. Thus, it is clearly separated from the IL contribution exhibiting the 2.6 eV energy onset, and can be assigned to the Ruthenium t_{2g} molecular orbital. Such a spectral composition is highly preferable for the time resolved PES study since it allows a better transient signal quality, not suffering from an additional and potentially strong background of solvent ionization. For the $[Ru(bpy)_3]^{2+}$ complex dissolved in water, a binding energy value of 6.81 eV can be found in literature [235]. However, this number refers to the vacuum level as it is a common procedure to define the absolute energy scale in water jet experiments. Taking the spectrometers work function of 4.4 eV into account, the binding energy values are in good agreement.

Adjacent to the dye HOMO band at the higher binding energy site, a second even stronger pronounced peak is apparent. This signal is attributed to ionization of the Cl^- 3p counter ion of the sample. Its maximum arises at a binding energy of 4.8 eV. The previously reported value of the binding energy of aqueous Cl^- relative to the vacuum level is 9.6 eV [235,236]. Thus, there is a slight deviation of 0.4 eV in binding energies of Cl^- in water and the IL. However, a precise determination of the Cl^- peak energy is rather difficult due to the spectral overlap with the much stronger ionization contribution of the IL, and one should also not exclude that ionization of the $[Ru(bpy)_3]^{2+}$ complex can give rise to other energy peaks lying in the vicinity of 4.8 eV binding energy. The latter issue represents an interesting subject for further investigations.

It is important to point out that the experiment was conducted with a $[Ru(bpy)_3]^{2+}$ concentration close to the solubility limit. However, the Ruthenium contribution appears to be relatively weak in the emission spectra. Though, without knowledge of the ionization cross sections of the solvent and the solute it is difficult to draw any conclusion with regard to the absolute signal amplitude of the Ruthenium peak. Comparing the ionization yield from the Cl^- 3p and Ru t_{2g} orbitals, a ratio of approximately 25 is found whereas the previously reported value is 2 [235]. The depletion of $[Ru(bpy)_3]^{2+}$ ions at the surface can be the reason for this discrepancy. The low ionization yield of $[Ru(bpy)_3]^{2+}$ represents an important issue in this study, since it extends considerably the acquisition time required to obtain sufficient statistic of the transient signal. Further efforts are needed to verify the reason for the relatively low signal of $[Ru(bpy)_3]^{2+}$ and to develop approaches enabling to enrich the concentration of the metal complex at the surface.

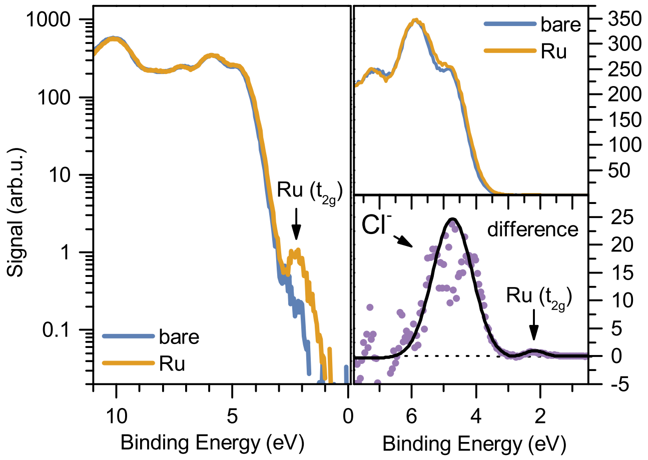

Fig. 4.19 (Left) Steady-state XUV spectra of photoelectrons recorded for the bare IL (blue line) and for the 100 mM solution of $[Ru(bpy)_3]^{2+}$ (yellow line) (logarithmic scale). (Right) The upper panel presents in detail the ionization contribution from the solute (linear scale). The lower panel shows the difference in the emission yield between the two spectra. The emission peak from the $[Ru(bpy)_3]^{2+}$ ground state arises at 2.3 eV binding energy.

4.3.4 Long Term Stability

The stability of IL under exposure to XUV radiation represents an important issue in the present study. Sample damage or diffusion might be possible effects giving rise to unintended spectral changes. Therefore, XUV spectra for the bare IL and the solute-containing sample were recorded over a time span of several hours.

Results obtained for the bare IL are presented below first. Figure 4.20(a) shows exemplary spectra acquired after three different XUV exposure times: 0h (fresh sample), 1h exposure, and 14h exposure. The signal was normalized according to the applied XUV intensity which was monitored during the experiment. In the binding energy range between 4.5 and 7 eV, the spectra exhibit no distinct differences. The photoemission yield integrated over this energy range is shown in Fig. 4.20(b) by red dots as a function of the exposure time (also denoted by int1). Note that the integrated yield after each exposure time is normalized to the value of the fresh sample and the latter is assigned to 1. The absence of any variation in the shown dependency confirms the stability of XUV spectra in this energy range.

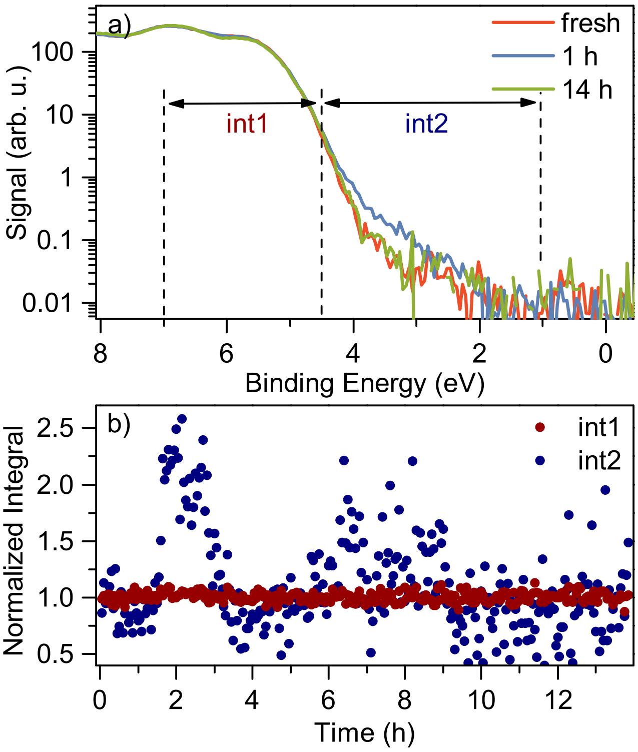

Fig. 4.20 a) Steady-state XUV spectra of the bare IL obtained in the beginning of exposure to the XUV beam (red line, fresh), after an exposure time of 1 hour (blue line, 1h) and 14 hours (green line, 14h). b) Ionization yield integrated over the range of binding energies between 7 and 4.5 eV (int1, red dots) and between 4.5 and 0 eV (int2, blue dots) as a function of the XUV exposure time. The integrated yield is normalized to the value of the fresh sample, which is assigned to 1.

In contrast, a change of the XUV spectra in the range of binding energies between 4.5 and 1 eV can be observed. To quantify the spectral changes as a function of the exposure time, the photoemission yield was integrated over this range of binding energies. The results are shown in Fig. 4.20(b) by blue dots (also denoted by int2). The changes exhibit no distinct structure. From the dependency of the integrated yield on the exposure time, it can be seen that the appearance of the additional shoulder in the spectrum (see Fig. 4.20(a)) is randomly distributed in time. Approximately after one hour of illumination, it starts to grow on a timescale of less than 30 minutes. Afterwards, the yield stabilizes for one hour before it starts to decrease again. Such a behavior is repeated again at later time. However, the spectra acquired with the fresh sample and after 14h of exposure appear to be identical. This finding leads to the conclusion that the spectral changes are reversible. A possible origin can lie in the fact that the liquid sample consists of ions which are able to randomly move from the bulk to the surface and vice versa. In addition, since the IL is an ionic conductor a directed transport in the form of ion flow is required to recharge the photo-ionized sample surface. This might lead to a continuous ion exchange in the probed sample. Thermal instabilities and other experimental circumstances might influence the formation of a constant equilibrium.

The obtained results do not reveal any clear indications of sample damage in terms of chemical changes. One should not exclude that the mentioned above ion exchange can lead to a refreshment of the sample surface in a continuous way and, thus, to the surface recovery from damages in single molecules. Since a volume of approximately 1 µL of IL was used, a sufficient amount of sample can be replaced in the interfacial region.

Figure 4.21 illustrates the steady state spectra recorded for the solute-containing IL. For this sample, the HOMO band contribution of the dye is clearly apparent in the spectra. One can see that the spectra exhibit changes which are very similar as in the previous investigation. The same two energy intervals were used to calculate the integrated yield which is shown in Fig. 4.21(b). For the range of higher binding energies (int1) a constant yield is observed, whereas for the lower energy part (int2) variations in the integrated yield are present.

As a supplementary measurement, the XUV exposure was interrupted for one hour after 13.5 hours of continuous illumination. The spectra recorded immediately after the break appeared to be rather identical to the spectrum of the fresh sample. However, the same tendency in spectral changes starts arising again, and after one hour of exposure the deviation of the integrated yield reaches similar amplitude as before the break. This finding provides further support for the conclusion that irradiation by XUV beam induces an ion flow which neutralizes the deficiency of negative charges at the samples surface caused by photo-emission. However, the charge equilibrium seems to be unstable, leading to the observed fluctuations.

Another important finding is the fact that the dyes HOMO band appears identical in the spectrum after enduring XUV exposure (see Fig. 4.21(a). This implies that the spectral changes are related solely to ionization of IL. Even if degradation of the dye is present, the continuous ion flow at the surface seems to renew the surface coverage.

In general, the found instabilities complicate investigation of the electron dynamics in solute molecules. Nevertheless, the spectral changes appear on a much longer timescale than a typical duration of 20 minutes of pump-probe scans. This yields the possibility to perform a proper background correction. The data analysis of the transient signal is presented in the following part.

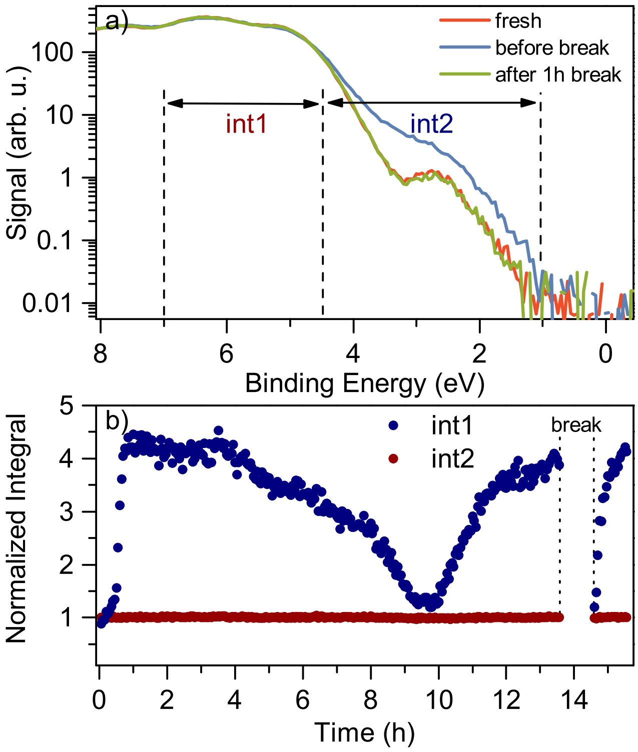

Fig. 4.21 Steady-state XUV spectra of the IL containing 100 mM of $[\mathrm{Ru(bpy)_3}]^{2+}$, obtained at the beginning of exposure to the XUV beam (red line, fresh), after an exposure time of 13.5 hours (blue line, before break) and after a break of 1 hour (green line, after 1h break). b) Ionization yield integrated over the range of binding energies between 7 and 4.5 eV (int1, red dots) and between 4.5 and 0 eV (int2, blue dots) as a function of the XUV exposure time. The integrated yield is normalized to the value of the fresh sample, which is assigned to 1. After 13.5 hours of exposure, the XUV beam was blocked for 1 hour.

4.3.5 Transient PES Study

The properties of the molecular excited states of $[\mathrm{Ru(bpy)_3}]^{2+}$ have been intensively studied and the electronic transitions involved in the light-induced photo-cycle in this complex are known. Fig. 4.22 illustrates the photochemical cycle of $[\mathrm{Ru(bpy)_3}]^{2+}$.

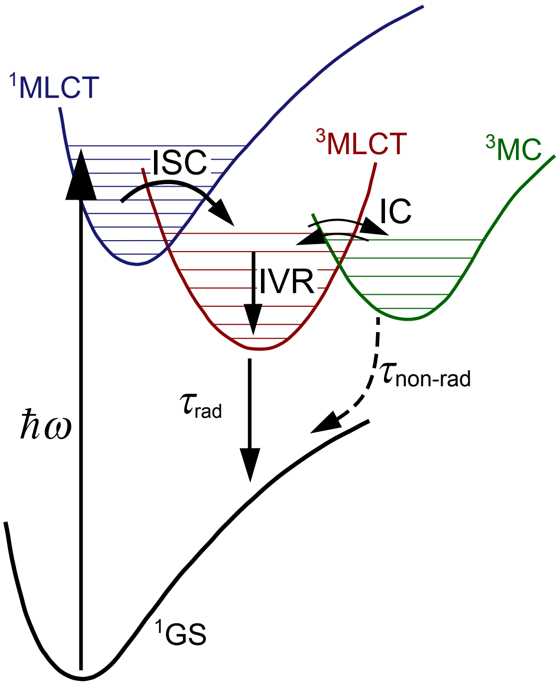

Fig. 4.22 The photochemical cycle of $[\mathrm{Ru(bpy)_3}]^{2+}$ depicted in a simplified energy level diagram. Absorption of visible light lifts a Ru d electron from the ground ^{1}GS state to the excited ^{1}MLCT state, where it undergoes ultrafast intersystem-crossing into the ^{3}MLCT state. The ^{3}MLCT state decays via two channels: non-radiatively via internal conversion to the ^{3}MC state and radiatively to the ground state with a time decay constant of up to 1 µs.

Optical excitation leads to a charge transfer transition from the metal-centered d orbital of the singlet ground state (^{1}GS) to the ligand-centered π^* orbital of the excited MLCT state. The prepared excited state is singlet (^{1}MLCT) and it undergoes ultrafast intersystem crossing, leading to the formation of the long-lived triplet ^{3}MLCT state with nearly unity quantum yield. It is commonly accepted that this process occurs on a time scale well below 100 fs [237,238] whereas much shorter transition times of 15 fs [58] are reported. From luminescence measurements in liquid solutions, the radiative decay of the ^{3}MLCT was found to exhibit a time constant on the order of 1 µs with an overall quantum yield of 5% [239,240] in H_2O and 9% [240] in CH_3CN. The reason for the rather low quantum yield is the competing non-radiative decay channel to the triplet metal-centered states ^{3}MC via an efficient internal conversion (IC) mechanism. For $[\mathrm{Ru(bpy)_3}]^{2+}$ the ^{3}MC state was found to be energetically higher than the ^{3}MLCT state [239,241,242]. Therefore, the quenching of the ^{3}MLCT luminescence appears to be thermally activated. Though, the population of this intermediate state remains negligible at all times due to a much higher non-radiative relaxation rate of the ^{3}MC to the ^{1}GS.

Another simultaneously occurring energy disposal mechanism is internal vibrational relaxation (IVR) within the complex. For the initially populated high vibrational levels of the ^{3}MLCT state, femtosecond fluorescence spectroscopy revealed their decay time via IVR being completed within 300 fs[55,58]. This value has been the subject of intense discussions since larger values of up to picoseconds have been also reported [237]. At room temperature, the luminescence does not exhibit any structure originating from the thermally equilibrated excited state and has a maximum at approximately 2 eV photon energy [239].

The transient PES study was performed with a pump beam of 480 nm wavelength, giving rise to resonant excitation of the singlet metal-to-ligand charge-transfer state (^{1}MLCT). The electron population distribution among transient states is probed by applying the 21st harmonic of 32 eV photon energy. The transient signal (TS) was derived by subtracting the XUV spectra recorded at negative delay times as a background from the pump-probe spectra. The color map given in Fig. 4.23 (Data) presents the two-dimensional dependency of TS on the binding energy and the time delay.

The TS exhibits several distinct features which are first discussed qualitatively below. A detailed analysis of the data by using a global fit and the derivation of kinetic values and binding energies of the involved states are presented in the next section.

At short time delays (± 100 fs), the TS exhibits a strong contribution at binding energy of approximately 3.0 eV. This component can be clearly attributed to the cross-correlation (CC) signal originating from the bare IL substrate. Its temporal width is found to be 120 fs (FWHM), which reproduces the value from experiments on the bare ILs and depicts the overall temporal resolution of the spectrometer throughout these studies. The CC component represents an unavoidable contribution to the TS. However, due to its favorable appearance in the TS at higher binding energies, a clear spectral separation of the sample-related signal is achieved. This represents another important issue which one needs to consider when choosing an IL as a solvent for a transient PES experiment. In addition to the requirement of large IL's ionization potential in order to avoid the overlap between the solvent and solute XUV spectra, the IL spectrum shifted by one photon energy of the pump beam should not coincide with the ionization signal from a transient state of the solute.

The negative value of the TS at kinetic energies corresponding to the Ru t_{2g} molecular orbital at 2.3 eV arises due to the depletion of the ground state caused by photo-excitation. The ground state bleach is formed within the pump pulse duration and remains constant over the pump-probe time interval shown in Fig. 4.23. Even on a larger timescale of up to 2 ns (not shown here), no changes in the negative TS signal could be observed. This characterizes the long lifetime of the molecular excited state, associated with a weak relaxation transition to the ground state configuration. Another long-lived feature, which remains unknown yet, is the positive signal appearing at binding energies larger than 3 eV. Since this feature lies in

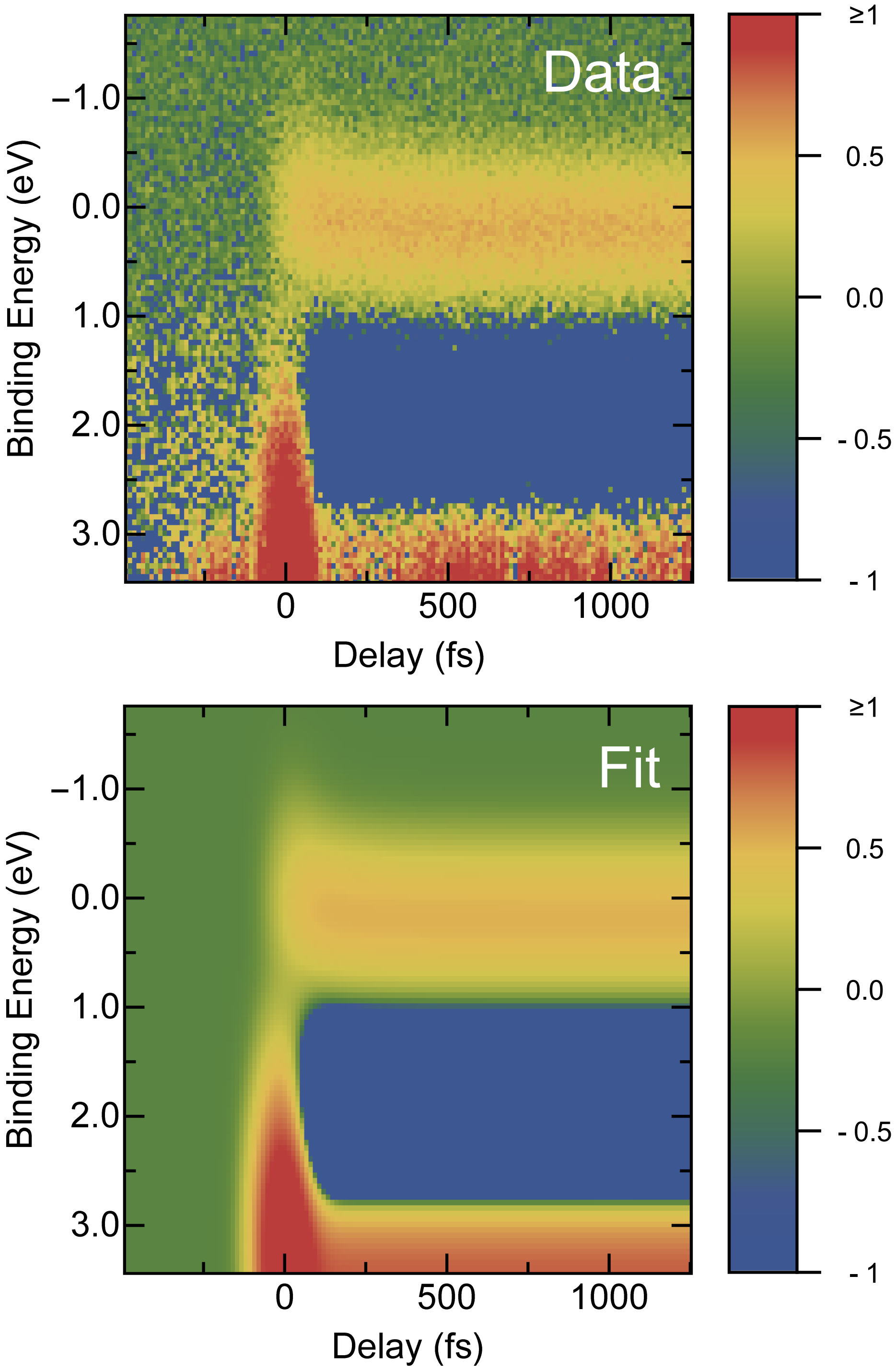

Fig. 4.23 2D color maps of the background-subtracted transient signal obtained for a 100 mM solution of $[Ru(bpy)_3]^{2+}$ in [EMIM][TfO]. Bottom panel shows the reproduction of experimental data by a global fit with the use of the sequential model (see text).

the vicinity of the ground state bleach, it needs to be considered in the global fit analysis presented below.

In the range of binding energies below 1 eV, the TS is more complex. This spectral region encompasses the excited states of $[\mathrm{Ru(bpy)_3}]^{2+}$, including the initially populated ^{1}MLCT as well as the states involved in the subsequent relaxation dynamics. The signals appearance in the time domain is clearly shifted with respect to the CC peak which determines time zero. It indicates that this part of the TS originates from resonantly populated states with lifetimes in the order or larger than the CC duration. Particularly noteworthy is the spectral drift of the component which is centered at approximately -0.2 eV at low time delays and is shifted to 0.3 eV at time delays larger than 500 fs. Similar to the ground state bleach, this shifted spectral component remains constant over the range of long time delays applied in the experiment and, apparently, can be assigned to the long lived ^{3}MLCT. Another proof of this assignment is given by the difference in binding energy of 2.0 eV between the ^{3}MLCT and the ground state, which fits well to the wavelength of fluorescence originating from the thermally equilibrated ^{3}MLCT excited state.

It is important to note that this occurrence is not self-evident since the PES and fluorescence spectroscopic methods obey different selection rules. The fluorescence signal is defined by the overlap integral between the occupied vibrational ^{3}MLCT states and the ground state, which is not the case for PES. However, since the thermal equilibrium is reached, only a minor discrepancy is expected. The drift in the TS below 500 fs and the possible contributions from other states are discussed in the subsequent section.

4.3.6 Global Fit Analysis

The TS shown in Fig. 4.23 was analyzed in terms of a global fit. The kinetic model implemented on the basis of previously reported relaxation channels has the form:

$$S_0 \xrightarrow{P(t)} {}^1MLCT \xrightarrow{k_1} {}^3MLCT_{hot} \xrightarrow{k_2} {}^3MLCT_{cold} \xrightarrow{k_3} S_0 \tag{4.4}$$

where $P(t)$ denotes the photo-excitation rate of the ^{1}MLCT state from the ground state S_0. The rate constants k_{1-3} characterize the subsequent transitions to the hot and then cold ^{3}MLCT state as well as the recombination to the ground state. Hereby the triplet state is divided into two contributions (${}^3MLCT_{hot}$ and ${}^3MLCT_{cold}$) to account for the vibrational cooling within this state. This approach can be seen as a simplification for taking into account a finite number of vibrational states with individual binding energies and relaxation rates. The following system of differential equations describes the above depicted population dynamics:

$$\begin{aligned}
\frac{d\left[{}^1MLCT\right]}{dt} &= P\left(t\right)\left[S_0\right] - k_1\left[{}^1MLCT\right] \\
\frac{d\left[{}^3MLCT_{hot}\right]}{dt} &= +k_1\left[{}^1MLCT\right] - k_2\left[{}^3MLCT_{hot}\right] \\
\frac{d\left[{}^3MLCT_{cold}\right]}{dt} &= +k_2\left[{}^3MLCT_{hot}\right] - k_3\left[{}^3MLCT_{cold}\right] \\
\frac{d\left[S_0\right]}{dt} &= -P\left(t\right)\left[S_0\right] + k_3\left[{}^3MLCT_{cold}\right]
\end{aligned} \tag{4.5}$$

The system of rate Eqs. 4.5 was solved numerically with the initial condition that all involved excited states are unpopulated and only the ground state S_0 is initially occupied. The ionization signal from the individual states was calculated by convoluting their transient population with the temporal envelope of the XUV probe pulse. Hereby the probe step was assumed to be non-saturated and the emission energy peaks were considered to have Gaussian envelopes. For both pump and probe pulses Gaussian time envelopes were used, with a constraint that their convolution yields the measured CC width. Additionally to the four states considered above, the CC signal as well as the signal above 3 eV binding energy, denoted by Q_0, were taken into account in the numerical procedure. The transition rates k_{1-3} and the emission spectra of transient states were obtained from the global fit of predictions by the model to the measured TS. A reproduction of the experimental data can be seen in Fig. 4.23 (Fit). It demonstrates the excellent agreement of the TS and the fit results. The obtained fit parameters, such as the binding energies E_b, the bandwidths ΔE_b, and the decay time constants τ_d of the transient states, are summarized in Table 4.2. Additionally, time traces as well as energy traces at specific time delays and binding energies are shown in Fig. 4.24 and Fig. 4.25, respectively, including the TS decomposition to individual contributions from the involved states obtained from the fit.

Table 4.2 Lifetime constants (τ_d) of the ^{1}MLCT, ^{3}MLCT$_{cold}$ and ^{3}MLCT$_{hot}$ states obtained from the modeling of the transient signal with the use of Eq. (4.5). The binding energies (E_b) of the states and their widths (ΔE_b) are also presented.

State	E_b (eV)	ΔE_b(eV)	τ_d
^{1}MLCT	-0.2 ± 0.2	1.2	(37 ± 10) fs
^{3}MLCT$_{hot}$	0.1 ± 0.2	0.9	(120 ± 20) fs
^{3}MLCT$_{cold}$	0.3 ± 0.1	0.9	> 1 ns
S_0	2.3 ± 0.1	1.2	> 1 ns

The initially populated ^{1}MLCT state is found to lie at a binding energy of -0.2±0.2 eV. The energy difference to the S_0 ground state is therefore given by 2.5 eV and matches within the error estimate the applied excitation photon energy of 2.58 eV. This finding supports for the assignment of this spectral component to the singlet ^{1}MLCT state. Its lifetime (inverse of the transition rate k_1) of (37±10) fs is inferred from the fit. This value is identical to the intersystem crossing time constant that was reported by Bhasikuttak et al. [237]. However, the much shorter decay time in the order of 15 fs reported in Ref. [58] cannot be confirmed. One should note that the cross-correlation width imposes limitations on the time resolution in the present experiment, so that any rigorous conclusion on such a short timescale appears to be difficult.

The vibrational relaxation from the $^3MLCT_{hot}$ to the $^3MLCT_{cold}$ was found to take place within 120 fs. This number represents the inverse value of the fitted transition rate k_2, meaning that the amplitude of the hot state decreased down by the factor of 1/e. The literature values mostly refer to the complete disappearance of signal from vibrationally hot states, and provide time constants within 300 fs [55,58]. Considering a signal decrease by one order of magnitude, one can recalculate a relaxation time of 280 fs, which is in good agreement with the previously reported values. The present work reveals that a total energy dissipation of approximately 0.6 eV occurs within this time interval. Since in previous experiments a much higher photon energy of 3.1 eV was applied, even higher dissipation values of 1.1 eV were found [55,58]. Such a fast dissipation raised the discussion to what extend the solvent environment influences the intramolecular excited states dynamics. Canizzo et al. [58] argued that due to the fast progression of the energy dissipation, a transfer to the solvent is unlikely and rather an energy transfer from high-frequency modes to low-frequency modes takes place as reported for the case of bacteriorhodopsin [243]. In contrast, Damrauer et al. [55] claimed that the intramolecular vibrational relaxation is connected to solvent reorganization due to the formation of an excited state exhibiting a large dipole moment. The similarities between the reported values for commonly used solvents (H_2O in [58] and CH_3CN in [55]) and the present value obtained for the IL environment indicate that solute–solvent interactions are only of minor importance. However, theoretical modeling of the electrostatic interactions in ILs remains on a poor level until today[244], preventing any valuable prediction of the correlation strength between solvent and solute.

One should note that the found energy positions of the two highest excited states (^{1}MLCT, $^3MLCT_{hot}$) exhibit uncertainties because of their broad and overlapping character as well as because of the limited experimental temporal and spectral resolution. Additional complication arises when considering that the intersystem crossing and the intramolecular vibrational relaxation take place simultaneously, making the modeling much more complex. However, the position of the long-lived $^3MLCT_{cold}$ can be unambiguously determined from the TS above 500 fs. To describe the early-time dynamics, an attempt was made to prove the validity of the three-state model by omitting the intermediate $^3MLCT_{hot}$ state. As a result the fastest decay constant was found to be larger than 100 fs and, therefore, the fit did not reproduce the spectral components at the binding energies below -0.2 eV which evolve on a much faster timescale. Since the ultrafast component could not be adequately reproduced, the three-state model described above was found to yield a better qualitative agreement. On the other hand, introducing even more states in addition to the $^3MLCT_{hot}$ certainly leads to more flexibility and better fit results on the basis of the residual analysis. However, due to the above mentioned limitations a more complex fit model associated with a larger number of parameters would not yield to a better understanding of the relaxation mechanisms.

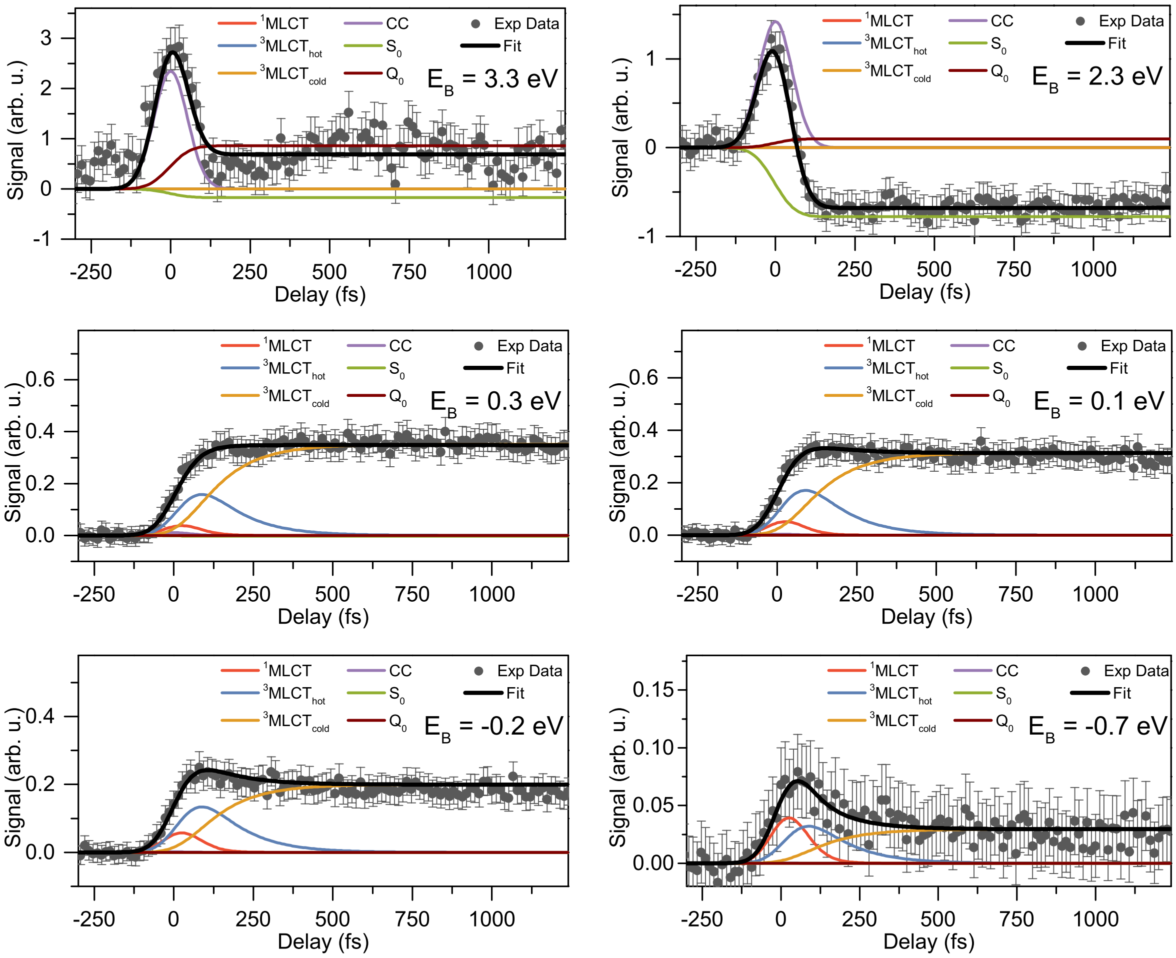

Fig. 4.24 Time dependency of the transient signal at different binding energies indicated in each panel individually.

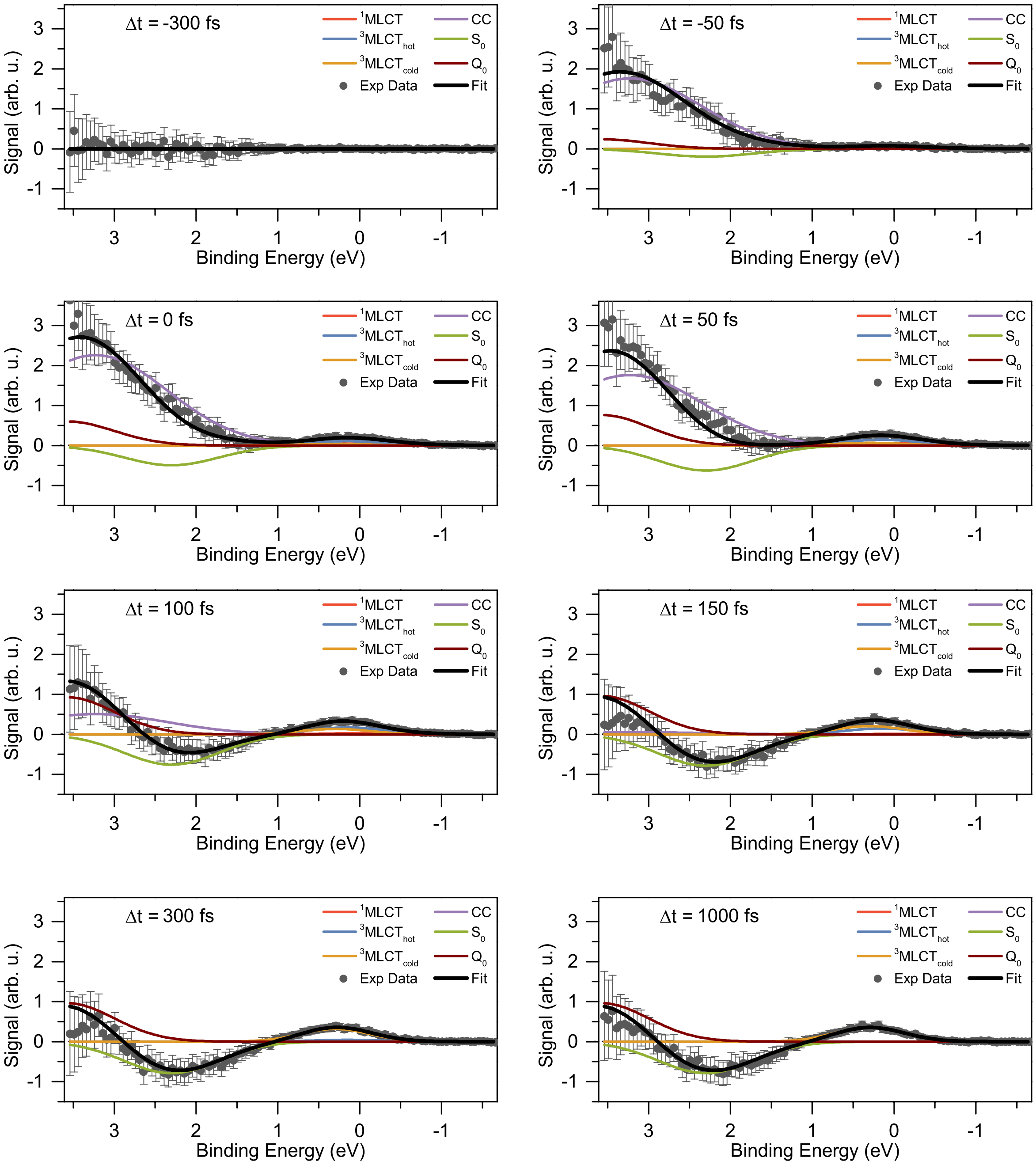

Fig. 4.25 Energy dependency of the transient signal at different pump probe time delays indicated in each panel individually.

4.3.7 Conclusion

The photo-physical properties of $[\mathrm{Ru(bpy)_3}]^{2+}$ dissolved in ILs was investigated by means of time resolved photoelectron spectroscopy. Hereby, the general applicability of ILs as solvent in view of their stability under UHV conditions, the visibility of the solute signatures, and the solvent-solute interaction was characterized in detail.

At first, the analysis of the bare ILs showed a favorable ionization potential, enabling to clearly separate the HOMO state contributions of the solute from the solvents features in the XUV photoemission spectrum. This makes ILs beneficial if the structure of the frontier molecular orbitals and dynamics of different samples need to be addressed. Though, the long-term investigation showed minor fluctuations in ILs, which are tolerable on the timescale of pump-probe scans applied in this investigation but still require an appropriate evaluation procedure. Diffusion effects induced by the current flow recharging the samples surface were suggested as the possible origin of these fluctuations. However, a direct correlation between their discontinuities and the surrounding experimental conditions is still unclear and further analysis of the solvent behavior is needed.

Steady state spectra exhibit emission yield from the HOMO band of the $[\mathrm{Ru(bpy)_3}]^{2+}$ molecule with the absolute binding energy being identical to the value found in aqueous solution. A comparison of the ratio of $\mathrm{Cl^-}$ 3p and Ru t_{2g} emission yields with the ratio previously observed in aqueous solution indicates a possible surface depletion of the$[\mathrm{Ru(bpy)_3}]^{2+}$ ion, leading to a reduced sensitivity of PES applied to study the photo-induced effects in this metal complex.

Further, the transient signal of $[\mathrm{Ru(bpy)_3}]^{2+}$ was analyzed by applying a global fit procedure. The kinetic model included the intersystem crossing from the ^{1}MLCT to the ^{3}MLCT state as well as the intra-molecular vibrational relaxation within the triplet state. The obtained transition rates were found to be in good agreement with literature values and provided evidence that the solvation dynamics has only minor influence on the ultrafast deactivation processes. The initially populated ^{1}MLCT state and the final thermally relaxed ^{3}MLCT could be clearly separated, whereas for the intermediate species the description relies on the kinetic model used in the fit analysis. This is due to the fact that the relaxation dynamics can undergo different channels simultaneously and involve different states closely lying on the energy scale.

Summarizing, this study demonstrates the advantageous properties of ILs serving as solvents. The particular problem arising from sample evaporation, which needs to be overcome in PES experiments, can be solved due to the extremely low vapor pressure of ILs. The ultrafast photoemission spectroscopy applied here has proven to be a powerful tool for exploring both the ultrafast electron dynamics and the absolute binding energies of the involved states. As a next step, more complex mechanisms such as electron transfer reaction between different species can be investigated, which represents a wide field of potential applications in photochemistry and photobiology.

Chapter 5

Summary

In this work, the ultrafast dynamics of photo-excited Ruthenium transition metal complexes and their heterogeneous electron transfer (HET) to nanostructured semiconductor interfaces was investigated by means of time-resolved XUV photoelectron spectroscopy (PES). Fundamental questions regarding the energetic band alignment at the various donor and acceptor interfaces, the charge separation across such interfaces, and the relaxation dynamics of charge carriers due to recombination and energy dissipation were addressed. In this context, the capabilities of PES were systematically investigated and its advantages compared to other spectroscopic methods were demonstrated.

The process of high harmonic generation was applied to achieve the necessary photon energy and time resolution. At first, the spectral and temporal characteristics of the recently built experimental setup were presented. It was found that the use of a reflective zone plate is highly beneficial in terms of simplified handling and stable operation of the XUV light source on a daily basis, as well as when a minimum of temporal broadening is required. Beside these experimental details, an important aspect related to the application of ultra-short and intense light pulses, the so called space-charge effect, was discussed. It was shown that this effect can have a detrimental impact on the measured photoelectron spectra. These findings underlined that special attention has to be paid to particularly limit the pump pulse intensity and the necessity of developing correction routines to handle the SCE appropriately.

The thesis focus was laid on the direct determination of the band alignment between donor and acceptor states at the dye-sensitized semiconductor substrates. Due to the fact that comparable studies at such nanostructured interfaces with the use of time-resolved PES in the XUV regime were not available, the initial investigation at the commonly used TiO_2 substrate can be considered as a benchmark establishing the PES method as a routine technique in this field. As pointed out throughout the thesis, the detailed knowledge about the band alignment is very crucial for understanding the charge transfer mechanisms. The specific application of PES allowed to determine for the first time directly the absolute binding energies of the excited states involved in the electron dynamics. On the basis of detailed modeling, the transient signal could be decomposed into contributions of the involved particular states and assigned in accordance with the previously reported two-state injection model. The initially populated ^{1}MLCT state was found to lie at 0.7 eV above the conduction band minimum. Such an energetic position was argued to be a strong driving force for injection from this state and the reason for the ultrafast charge transfer. This is indicated by the lifetime of the ^{1}MLCT yielding a value of (20 ± 10) fs. The ^{3}MLCT state populated by intersystem crossing was determined at 0.2 eV below the conduction band. The energy position of the triplet state well below the ^{1}MLCT constitutes a considerable energy dissipation mechanism. Injection from the triplet state, thus, occurs only due to a partial energy overlap with the conduction band, leading to slow kinetics of the electron transfer on the picosecond time scale. Due to the spectral decomposition of the transient emission signal, it was possible to follow the ultrafast population and decay dynamics of the excited states individually. The time constants inferred in this study are in good agreement with reported values in literature.

Subsequently, based on the detailed characterization of the HET mechanism at the sensitized TiO_2 interface, another promising semiconductor substrate, ZnO, was investigated. Previous investigations found that the HET occurs in this material on a much slower picosecond timescale as compared to TiO_2. The comparative study between both interfaces could confirm these findings and revealed direct evidence for the formation of an interfacial electronic state at ZnO being the origin of the delayed release of free charges into the conduction band. In both cases, multi-exponential decay of the transient signal was revealed. However, the initial fast component of (35 ± 10) fs decay time, measured at the TiO_2 interface, was not present at ZnO. Since the intersystem crossing of the used N3 dye complex has been found to occur on a time scale of 100 fs, this finding strongly indicates that the intermediate state formation has to be considerably faster. It has to be emphasized that although the energetic band alignment at the ZnO interface was found to be more favorable compared to TiO_2, the generation of free electrons appeared to be delayed. Hence, contrary to previous assumptions this finding demonstrates that in the case of ZnO bulk properties such as the conduction band density of states and energetic band alignment are of minor importance for the electron transfer process, whereas rather the dye-ZnO interaction plays the key role in the HET. Further analysis is needed to gain more detailed insight into the true nature of the intermediate state formation and its origin.

The last part of this thesis was focused on the electron dynamics of the transition metal complex $[Ru(bpy)_3]^{2+}$ dissolved in ionic liquid (IL) EMIM TfO. Usually investigation of samples in a liquid environment is associated with commonly high vapor pressure, which often represents a limiting factor for the application of PES. Therefore this study aimed to explore the applicability of ILs as solvents with regard to their stability under UHV conditions, the possibility to follow the photo-induced dynamics in the solute, and the effects of solvent-solute interaction. One important aspect is the valence-shell electronic structure of the solute characterized by the ionization potential. The noise level of the transient signal is limited by the steady state background and therefore a clear distinction of the solute and solvent contributions is required. The analysis of the electronic structure of bare IL showed a favorable ionization potential, suitable to clearly separate the HOMO state of the solute from the solvent-related features in the emission spectra. From this point of view, it follows that ILs are beneficial if the frontier molecular orbitals and dynamics need to be addressed. From the steady state spectra of $[\mathrm{Ru(bpy)_3}]^{2+}$ it was found that the HOMO band of the complex, composed of the metal-center t_{2g} molecular orbital, exhibits identical absolute binding energy as compared to the value obtained for aqueous solution. However, the ratio of ionization yields of the Cl^- counter ion and the Ru t_{2g} state deviates significantly from the literature values obtained in aqueous solution. This indicates a possible depletion of the $[\mathrm{Ru(bpy)_3}]^{2+}$ ion at the IL surface, leading to a reduce sensitivity of the PES method and extended acquisition times.

Finally, the transient signal of $[\mathrm{Ru(bpy)_3}]^{2+}$ was analyzed with the use of a global fit. The results were compared to a kinetic three-state model which describes the intersystem crossing from the ^{1}MLCT to the $^3\mathrm{MLCT}_{hot}$ state as well as the population of the thermally relaxed $^3\mathrm{MLCT}_{cold}$ state to account for the intramolecular vibrational relaxation within the triplet configuration. The derived decay characteristics of states are in good agreement with literature values obtained in aqueous solution, which reveals that the solvation dynamics have only minor influence on the early ultrafast deactivation processes. By means of the global fit analysis, the binding energies of the initially populated ^{1}MLCT state and the thermally relaxed ^{3}MLCT could be determined. Their values are found to be -0.2 eV and 0.3 eV, respectively. Compared to a simplified two-state model, the three-step model gives much better qualitative agreement with the experiment, consisting in the fact that the ultrafast spectral component could be adequately reproduced.

Summarizing, the thesis demonstrates throughout all three investigations the potential application of time-resolved XUV photoelectron spectroscopy to study the ultrafast electron dynamics in such molecular systems. Due to the unique ability of this method in revealing absolute binding energies, its advantages compared to other approaches based on absorption and fluorescence spectroscopies are demonstrated. A promising enhancement of the PES approach could be the application of even higher photon energies, enabling the direct access to element-specific information. Photon energies used in this work, applied to probe exclusively the valence-shell electronic structure, do not allow to draw directly any site-specific conclusions within the charge transfer process. Such experiments might be beneficial in monitoring the acceptor and donor states separately but have been performed so far only at expensive Free Electron Lasers, with access to such facilities being extremely limited. To expand the laser based light source into the X-ray spectral region new laser technologies and the HHG process driven by ultrashort mid-infrared laser pulses are currently under development.

References

[1] Thomas, C. D., Cameron, A., Green, R. E., Bakkenes, M., Beaumont, L. J., Collingham, Y. C., Erasmus, B. F. N., de Siqueira, M. F., Grainger, A., Hannah, L., et al. *Extinction risk from climate change.* Nature, 427(6970):145–148 (**2004**).

[2] Canadell, J. G., Quere, C. L., Raupach, M. R., Field, C. B., Buitenhuis, E. T., Ciais, P., Conway, T. J., Gillett, N. P., Houghton, R. A., and Marland, G. *Contributions to accelerating atmospheric CO_2 growth from economic activity, carbon intensity, and efficiency of natural sinks.* Proceedings of the National Academy of Sciences, 104(47):18866–18870 (**2007**).

[3] Würfel, P. *Physics of Solar Cells: From Basic Principles to Advanced Concepts.* John Wiley & Sons (**2009**). ISBN 9783527408573.

[4] Dittrich, T. *Materials Concepts for Solar Cells.* Imperial College Press (**2014**). ISBN 978-1-78326-444-5.

[5] Hagfeldt, A., Boschloo, G., Sun, L., Kloo, L., and Pettersson, H. *Dye-Sensitized Solar Cells.* Chemical Reviews, 110(11):6595–6663 (**2010**).

[6] Nozik, A. J. *Nanoscience and Nanostructures for Photovoltaics and Solar Fuels.* Nano Letters, 10(8):2735–2741 (**2010**).

[7] Ye, M., Wen, X., Wang, M., Iocozzia, J., Zhang, N., Lin, C., and Lin, Z. *Recent advances in dye-sensitized solar cells: from photoanodes, sensitizers and electrolytes to counter electrodes.* Materials Today, 18(3):155–162 (**2015**).

[8] O'Regan, B. and Grätzel, M. *A low-cost, high-efficiency solar cell based on dye-sensitized colloidal TiO_2 films.* Nature, 353(6346):737–740 (**1991**).

[9] Gao, F., Wang, Y., Zhang, J., Shi, D., Wang, M., Humphry-Baker, R., Wang, P., Zakeeruddin, S. M., and Grätzel, M. *A new heteroleptic ruthenium sensitizer enhances the absorptivity of mesoporous titania film for a high efficiency dye-sensitized solar cell.* Chemical Communications, (23):2635 (**2008**).

[10] Ardo, S. and Meyer, G. J. *Photodriven heterogeneous charge transfer with transition-metal compounds anchored to TiO_2 semiconductor surfaces.* Chemical Society Reviews, 38(1):115–164 (**2008**).

[11] Huang, Z. and Kim, K.-J. *Review of x-ray free-electron laser theory.* Physical Review Special Topics - Accelerators and Beams, 10(3):034801 (**2007**).

[12] McNeil, B. W. J. and Thompson, N. R. *X-ray free-electron lasers.* Nature Photonics, 4(12):814–821 (**2010**).

[13] Protopapas, M., Keitel, C. H., and Knight, P. L. *Atomic physics with super-high intensity lasers.* Reports on Progress in Physics, 60(4):389 (**1997**).

[14] Brabec, T. and Krausz, F. *Intense few-cycle laser fields: Frontiers of nonlinear optics.* Reviews of Modern Physics, 72(2):545–591 (**2000**).

[15] Balzani, V. *Electron Transfer in Chemistry.* Wiley-VCH Verlag GmbH (**2001**). ISBN 978-3-527-29912-6.

[16] Asbury, J. B., Hao, E., Wang, Y., Ghosh, H. N., and Lian, T. *Ultrafast Electron Transfer Dynamics from Molecular Adsorbates to Semiconductor Nanocrystalline Thin Films.* The Journal of Physical Chemistry B, 105(20):4545–4557 (**2001**).

[17] Jortner, J. and Bixon, M. *Advances in Chemical Physics, Volume 106, Part 1: Electron Transfer From Isolated Molecules to Biomolecules.* John Wiley & Sons (**2009**). ISBN 978-0-470-14218-9.

[18] Jortner, J. and Bixon, M. *Advances in Chemical Physics, Volume 107, Part 2: Electron Transfer From Isolated Molecules to Biomolecules.* John Wiley & Sons (**2009**). ISBN 978-0-470-14219-6.

[19] Marcus, R. A. *On the theory of oxidation-reduction reactions involving electron transfer. i.* The Journal of Chemical Physics, 24(5):966 (**1956**).

[20] Hush, N. S. *Homogeneous and heterogeneous optical and thermal electron transfer.* Electrochimica Acta, 13(5):1005–1023 (**1968**).

[21] Jortner, J. *Temperature dependent activation energy for electron transfer between biological molecules.* The Journal of Chemical Physics, 64(12):4860–4867 (**1976**).

[22] Hopfield, J. J. *Electron Transfer Between Biological Molecules by Thermally Activated Tunneling.* Proceedings of the National Academy of Sciences of the United States of America, 71(9):3640–3644 (**1974**).

[23] Gerischer, H. *Über den ablauf von redoxreaktionen an metallen und an halbleitern.* Zeitschrift für Physikalische Chemie, 26(5–6):325–338 (**1960**).

[24] Fox, M. A. and Chanon, M. *Photoinduced Electron Transfer*, volume A-D. Elsevier (**1988**). ISBN 978-0-444-87125-1.

[25] Barbara, P. F., Meyer, T. J., and Ratner, M. A. *Contemporary Issues in Electron Transfer Research.* The Journal of Physical Chemistry, 100(31):13148–13168 (**1996**).

[26] Kavarnos, G. J. and Turro, N. J. *Photosensitization by reversible electron transfer: theories, experimental evidence, and examples.* Chemical Reviews, 86(2):401–449 (**1986**).

[27] Marcus, R. A. *Electron Transfer Reactions in Chemistry: Theory and Experiment (Nobel Lecture).* Angewandte Chemie International Edition in English, 32(8):1111–1121 (**1993**).

[28] Marcus, R. A. and Sutin, N. *Electron transfers in chemistry and biology.* Biochimica et Biophysica Acta (BBA) - Reviews on Bioenergetics, 811(3):265–322 (**1985**).

[29] Adams, D. M., Brus, L., Chidsey, C. E. D., Creager, S., Creutz, C., Kagan, C. R., Kamat, P. V., Lieberman, M., Lindsay, S., Marcus, R. A., et al. *Charge Transfer on the Nanoscale: Current Status.* The Journal of Physical Chemistry B, 107(28):6668–6697 (**2003**).

[30] Miller, R. J. D. *Surface Electron Transfer Processes.* Wiley-Vch (**1995**). ISBN 978-1-56081-036-0.

[31] Schatz, G. C. and Ratner, M. A. *Quantum Mechanics in Chemistry.* Courier Corporation (**2012**). ISBN 978-0-486-13672-1.

[32] May, V. and Kühn, O. *Charge and Energy Transfer Dynamics in Molecular Systems.* Wiley-VCH (**2004**). ISBN 978-3-527-40396-7.

[33] Mikami, Y. *The numerical evaluations of the density of states weighted franck condon factor in large molecules. Effects of frequency changes.* The Journal of Chemical Physics, 73(7):3314–3320 (**1980**).

[34] Devault, D. *Quantum mechanical tunnelling in biological systems.* Quarterly Reviews of Biophysics, 13(04):387 (**1980**).

[35] Miller, J. R., Calcaterra, L. T., and Closs, G. L. *Intramolecular long-distance electron transfer in radical anions. The effects of free energy and solvent on the reaction rates.* Journal of the American Chemical Society, 106(10):3047–3049 (**1984**).

[36] Bixon, M. *Intramolecular radiationless transitions.* The Journal of Chemical Physics, 48(2):715 (**1968**).

[37] Moser, C. C., Keske, J. M., Warncke, K., Farid, R. S., and Dutton, P. L. *Nature of biological electron transfer.* Nature, 355(6363):796–802 (**1992**).

[38] Jortner, J. and Bixon, M. *Intramolecular vibrational excitations accompanying solvent-controlled electron transfer reactions.* The Journal of Chemical Physics, 88(1):167 (**1988**).

[39] Sumi, H. and Marcus, R. A. *Dynamical effects in electron transfer reactions.* The Journal of Chemical Physics, 84(9):4894–4914 (**1986**).

[40] Ramakrishna, S., Willig, F., and May, V. *Photoinduced ultrafast electron injection from a surface attached molecule: Control of electronic and vibronic distributions via vibrational wave packets.* Phys. Rev. B, 62(24):R16330–R16333 (**2000**).

[41] Ramakrishna, G., Jose, D. A., Kumar, D. K., Das, A., Palit, D. K., and Ghosh, H. N. *Strongly coupled ruthenium-polypyridyl complexes for efficient electron injection in dye-sensitized semiconductor nanoparticles.* The Journal of Physical Chemistry B, 109(32):15445–15453 (**2005**).

[42] Lanzafame, J. M., Miller, R. J. D., Muenter, A. A., and Parkinson, B. A. *Ultrafast charge-transfer dynamics at tin disulfide surfaces.* The Journal of Physical Chemistry, 96(7):2820–2826 (**1992**).

[43] Lanzafame, J. M., Palese, S., Wang, D., Miller, R. J. D., and Muenter, A. A. *Ultrafast Nonlinear Optical Studies of Surface Reaction Dynamics: Mapping the Electron Trajectory.* The Journal of Physical Chemistry, 98(43):11020–11033 (**1994**).

[44] Griffith, J. S. *The Theory of Transition-Metal Ions.* Cambridge University Press (**2009**). ISBN 978-0-521-11599-5.

[45] Kettle, S. F. A. *Physical Inorganic Chemistry: A Coordination Chemistry Approach.* Springer (**2013**). ISBN 978-3-662-25191-1.

[46] Paris, J. P. and Brandt, W. W. *CHARGE TRANSFER LUMINESCENCE OF A RUTHENIUM(II) CHELATE.* Journal of the American Chemical Society, 81(18):5001–5002 (**1959**).

[47] Vlček, A. *The life and times of excited states of organometallic and coordination compounds.* Coordination Chemistry Reviews, 200-202:933–978 (**2000**).

[48] Ferguson, J., Herren, F., Krausz, E. R., Maeder, M., and Vrbancich, J. *Electronic spectroscopy of M(bpy)2+3 (M = Fe, Ru, Os), Cr(bpy)3+3 and related compounds.* Coordination Chemistry Reviews, 64:21–39 (**1985**).

[49] Juris, A., Balzani, V., Barigelletti, F., Campagna, S., Belser, P., and von Zelewsky, A. *Ru(II) polypyridine complexes: photophysics, photochemistry, eletrochemistry, and chemiluminescence.* Coordination Chemistry Reviews, 84:85–277 (**1988**).

[50] Balzani, V., Juris, A., Venturi, M., Campagna, S., and Serroni, S. *Luminescent and Redox-Active Polynuclear Transition Metal Complexes.* Chemical Reviews, 96(2):759–834 (**1996**).

[51] Rillema, D. P. and Jones, D. S. *Structure of tris(2,2-bipyridyl)ruthenium(II) hexafluorophosphate, [Ru(bipy)3][PF6]2: X-ray crystallographic determination.* Journal of the Chemical Society, Chemical Communications, (19):849–851 (**1979**).

[52] Rillema, D. P., Jones, D. S., Woods, C., and Levy, H. A. *Comparison of the crystal structures of tris heterocyclic ligand complexes of ruthenium(II).* Inorganic Chemistry, 31(13):2935–2938 (**1992**).

[53] Harris, D. C. and Bertolucci, M. D. *Symmetry and Spectroscopy: An Introduction to Vibrational and Electronic Spectroscopy.* Courier Corporation (**1978**). ISBN 978-0-486-66144-5.

[54] Calzaferri, G. and Rytz, R. *Electronic Transition Oscillator Strength by the Extended Hueckel Molecular Orbital Method.* The Journal of Physical Chemistry, 99(32):12141–12150 (**1995**).

[55] Damrauer, N. H., Cerullo, G., Yeh, A., Boussie, T. R., Shank, C. V., and McCusker, J. K. *Femtosecond Dynamics of Excited-State Evolution in [Ru(bpy)3]2+.* Science, 275(5296):54–57 (**1997**).

[56] Yeh, A. T., Shank, C. V., and McCusker, J. K. *Ultrafast Electron Localization Dynamics Following Photo-Induced Charge Transfer.* Science, 289(5481):935–938 (**2000**).

[57] McCusker, J. K. *Femtosecond Absorption Spectroscopy of Transition Metal Charge-Transfer Complexes.* Accounts of Chemical Research, 36(12):876–887 (**2003**).

[58] Cannizzo, A., van Mourik, F., Gawelda, W., Zgrablic, G., Bressler, C., and Chergui, M. *Broadband Femtosecond Fluorescence Spectroscopy of [Ru(bpy)3]2+.* Angewandte Chemie International Edition, 45(19):3174–3176 (**2006**).

[59] Creutz, C., Chou, M., Netzel, T. L., Okumura, M., and Sutin, N. *Lifetimes, spectra, and quenching of the excited states of polypyridine complexes of iron(II), ruthenium(II), and osmium(II).* Journal of the American Chemical Society, 102(4):1309–1319 (**1980**).

[60] Eichberger, R. and Willig, F. *Ultrafast electron injection from excited dye molecules into semiconductor electrodes.* Chemical Physics, 141(1):159–173 (**1990**).

[61] Nazeeruddin, M. K., Kay, A., Rodicio, I., Humphry-Baker, R., Mueller, E., Liska, P., Vlachopoulos, N., and Grätzel, M. *Conversion of light to electricity by cis-X2bis(2,2'-bipyridyl-4,4'-dicarboxylate)ruthenium(II) charge-transfer sensitizers (X = Cl-, Br-, I-, CN-, and SCN-) on nanocrystalline titanium dioxide electrodes.* Journal of the American Chemical Society, 115(14):6382–6390 (**1993**).

[62] Baur, W. H. *Atomabstände und bindungswinkel im brookit, TiO_2.* Acta Crystallographica, 14(3):214–216 (**1961**).

[63] Pelaez, M., Nolan, N. T., Pillai, S. C., Seery, M. K., Falaras, P., Kontos, A. G., Dunlop, P. S. M., Hamilton, J. W. J., Byrne, J. A., O'Shea, K., et al. *A review on the visible light active titanium dioxide photocatalysts for environmental applications.* Applied Catalysis B: Environmental, 125:331–349 (**2012**).

[64] Cromer, D. T. and Herrington, K. *The Structures of Anatase and Rutile.* Journal of the American Chemical Society, 77(18):4708–4709 (**1955**).

[65] Diebold, U. *The surface science of titanium dioxide.* Surface Science Reports, 48(5-8):53–229 (**2003**).

[66] Mo, S.-D. and Ching, W. Y. *Electronic and optical properties of three phases of titanium dioxide: Rutile, anatase, and brookite.* Physical Review B, 51(19):13023–13032 (**1995**).

[67] Horn, M., Schwebdtfeger, C. F., and Meagher, E. P. *Refinement of the structure of anatase at several temperatures.* Zeitschrift für Kristallographie - Crystalline Materials, 136(1-6) (**1972**).

[68] Tang, H., Berger, H., Schmid, P., Lévy, F., and Burri, G. *Photoluminescence in TiO_2 anatase single crystals.* Solid State Communications, 87(9):847–850 (**1993**).

[69] Kavan, L., Grätzel, M., Gilbert, S. E., Klemenz, C., and Scheel, H. J. *Electrochemical and Photoelectrochemical Investigation of Single-Crystal Anatase.* Journal of the American Chemical Society, 118(28):6716–6723 (**1996**).

[70] Tiwana, P., Docampo, P., Johnston, M. B., Snaith, H. J., and Herz, L. M. *Electron Mobility and Injection Dynamics in Mesoporous ZnO, SnO2, and TiO2 Films Used in Dye-Sensitized Solar Cells.* ACS Nano, 5(6):5158–5166 (**2011**).

[71] Lyon, J. E., Rayan, M. K., Beerbom, M. M., and Schlaf, R. *Electronic structure of the indium tin oxide/nanocrystalline anatase (TiO2)/ruthenium-dye interfaces in dye-sensitized solar cells.* Journal of Applied Physics, 104(7):073714 (**2008**).

[72] Pomoni, K., Sofianou, M. V., Georgakopoulos, T., Boukos, N., and Trapalis, C. *Electrical conductivity studies of anatase TiO2 with dominant highly reactive {0 0 1} facets.* Journal of Alloys and Compounds, 548:194–200 (**2013**).

[73] Henrich, V. E. and Cox, P. A. *The Surface Science of Metal Oxides.* Cambridge University Press (**1996**). ISBN 978-0-521-56687-2.

[74] Scanlon, D. O., Dunnill, C. W., Buckeridge, J., Shevlin, S. A., Logsdail, A. J., Woodley, S. M., Catlow, C. R. A., Powell, M. J., Palgrave, R. G., Parkin, I. P., et al. *Band alignment of rutile and anatase* TiO_2. Nature Materials, 12(9):798–801 (**2013**).

[75] Özgür, U., Alivov, Y. I., Liu, C., Teke, A., Reshchikov, M. A., Doguan, S., Avrutin, V., Cho, S.-J., and Morkoc, H. *A comprehensive review of ZnO materials and devices.* J. Appl. Phys., 98(4):041301 (**2005**).

[76] Klingshirn, C. *ZnO: Material, physics and applications.* ChemPhysChem, 8(6):782–803 (**2007**).

[77] Look, D. C., Reynolds, D. C., Sizelove, J. R., Jones, R. L., Litton, C. W., Cantwell, G., and Harsch, W. C. *Electrical properties of bulk ZnO.* Solid State Communications, 105(6):399–401 (**1998**).

[78] Forro, L., Chauvet, O., Emin, D., Zuppiroli, L., Berger, H., and Levy, F. *High mobility n-type charge carriers in large single crystals of anatase (*TiO_2*).* Journal of Applied Physics, 75(1):633–635 (**1994**).

[79] Ambade, S. B., Mane, R. S., Han, S.-H., Lee, S.-H., Sung, M.-M., and Joo, O.-S. *Indoline-dye immobilized ZnO nanoparticles for whopping 5.44 percent light conversion efficiency.* Journal of Photochemistry and Photobiology A: Chemistry, 222(2–3):366–369 (**2011**).

[80] Saito, M. and Fujihara, S. *Large photocurrent generation in dye-sensitized ZnO solar cells.* Energy & Environmental Science, 1(2):280–283 (**2008**).

[81] Xie, Y., Joshi, P., Darling, S. B., Chen, Q., Zhang, T., Galipeau, D., and Qiao, Q. *Electrolyte Effects on Electron Transport and Recombination at ZnO Nanorods for Dye-Sensitized Solar Cells.* The Journal of Physical Chemistry C, 114(41):17880–17888 (**2010**).

[82] Lin, C.-Y., Lai, Y.-H., Chen, H.-W., Chen, J.-G., Kung, C.-W., Vittal, R., and Ho, K.-C. *Highly efficient dye-sensitized solar cell with a ZnO nanosheet-based photoanode.* Energy & Environmental Science, 4(9):3448–3455 (**2011**).

[83] Shokry Hassan, H., Kashyout, A. B., Soliman, H. M. A., Uosif, M. A., and Afify, N. *Effect of reaction time and Sb doping ratios on the architecturing of ZnO nanomaterials for gas sensor applications.* Applied Surface Science, 277:73–82 (**2013**).

[84] Lee, G., Kawazoe, T., and Ohtsu, M. *Difference in optical bandgap between zinc-blende and wurtzite ZnO structure formed on sapphire (0001) substrate.* Solid State Communications, 124(5-6):163–165 (**2002**).

[85] Tsukazaki, A., Ohtomo, A., Onuma, T., Ohtani, M., Makino, T., Sumiya, M., Ohtani, K., Chichibu, S. F., Fuke, S., Segawa, Y., et al. *Repeated temperature modulation epitaxy for p-type doping and light-emitting diode based on ZnO.* Nature Materials, 4(1):42–46 (**2005**).

[86] Wasserscheid, P. and Keim, W. *Ionic liquids—new "solutions" for transition metal catalysis.* Angewandte Chemie International Edition, 39(21):3772–3789 (**2000**).

[87] Rogers, R. D. and Voth, G. A. *Ionic Liquids.* Accounts of Chemical Research, 40(11):1077–1078 (**2007**).

[88] Weingärtner, H. *Understanding Ionic Liquids at the Molecular Level: Facts, Problems, and Controversies.* Angewandte Chemie International Edition, 47(4):654–670 (**2008**).

[89] Walden, P. and others. *Molecular weights and electrical conductivity of several fused salts.* Bull. Acad. Imper. Sci.(St. Petersburg), 8:405–422 (**1914**).

[90] Welton, T. *Room-Temperature Ionic Liquids. Solvents for Synthesis and Catalysis.* Chemical Reviews, 99(8):2071–2084 (**1999**).

[91] Wasserscheid, P. and Whelton, T. *Ionic Liquids in Synthesis (Green Chemistry (Wiley)(2 vol. set).* Wiley-VCH (**2007**). ISBN 3527312390.

[92] Plechkova, N. V. and Seddon, K. R. *Applications of ionic liquids in the chemical industry.* Chemical Society Reviews, 37(1):123–150 (**2007**).

[93] Paul T. Anastas, Peter Wasserscheid, and Annegret Stark. *Handbook of Green Chemistry, Green Solvents, Ionic Liquids.* John Wiley & Sons (**2014**). ISBN 978-3-527-68852-4.

[94] Krossing, I., Slattery, J. M., Daguenet, C., Dyson, P. J., Oleinikova, A., and Weingrätner, H. *Why Are Ionic Liquids Liquid? A Simple Explanation Based on Lattice and Solvation Energies.* Journal of the American Chemical Society, 128(41):13427–13434 (**2006**).

[95] van Rantwijk, F. and Sheldon, R. A. *Biocatalysis in Ionic Liquids.* Chemical Reviews, 107(6):2757–2785 (**2007**).

[96] Pârvulescu, V. I. and Hardacre, C. *Catalysis in ionic liquids.* Chemical Reviews, 107(6):2615–2665 (**2007**).

[97] Haumann, M. and Riisager, A. *Hydroformylation in Room Temperature Ionic Liquids (RTILs): Catalyst and Process Developments.* Chemical Reviews, 108(4):1474–1497 (**2008**).

[98] Byrne, N., Howlett, P. C., MacFarlane, D. R., and Forsyth, M. *The Zwitterion Effect in Ionic Liquids: Towards Practical Rechargeable Lithium-Metal Batteries.* Advanced Materials, 17(20):2497–2501 (**2005**).

[99] Wang, P., Zakeeruddin, S. M., Moser, J.-E., and Grätzel, M. *A New Ionic Liquid Electrolyte Enhances the Conversion Efficiency of Dye-Sensitized Solar Cells.* The Journal of Physical Chemistry B, 107(48):13280–13285 (**2003**).

[100] Kawano, R. and Watanabe, M. *Anomaly of charge transport of an iodide/tri-iodide redox couple in an ionic liquid and its importance in dye-sensitized solar cells.* Chemical Communications, (16):2107–2109 (**2005**).

[101] Gorlov, M. and Kloo, L. *Ionic liquid electrolytes for dye-sensitized solar cells.* Dalton Transactions, (20):2655 (**2008**).

[102] Teuscher, J., Marchioro, A., Andrès, J., Roch, L. M., Xu, M., Zakeeruddin, S. M., Wang, P., Grätzel, M., and Moser, J.-E. *Kinetics of the regeneration by iodide of dye sensitizers adsorbed on mesoporous titania.* J. Phys. Chem. C, 118(30):17108–17115 (**2014**).

[103] Bier, M. and Dietrich, S. *Vapour pressure of ionic liquids.* Molecular Physics, 108(2):211–214 (**2010**).

[104] Demtröder, W. *Laser Spectroscopy 1: Basic Principles.* Springer (**2014**). ISBN 978-3-642-53859-9.

[105] Jortner, J., Rice, S. A., and Hochstrasser, R. M. *Radiationless Transitions in Photochemistry.* In *Advances in Photochemistry*, pp. 149–309. John Wiley & Sons, Inc. (**1969**). ISBN 978-0-470-13337-8.

[106] Schoenlein, R. W., Peteanu, L. A., Mathies, R. A., and Shank, C. V. *The first step in vision: femtosecond isomerization of rhodopsin.* Science, 254(5030):412–415 (**1991**).

[107] Domcke, W. and Stock, G. *Theory of Ultrafast Nonadiabatic Excited-State Processes and their Spectroscopic Detection in Real Time.* In *Advances in Chemical Physics*, pp. 1–169. John Wiley & Sons, Inc. (**1997**). ISBN 978-0-470-14159-5.

[108] Zewail, A. H. *Femtochemistry: Atomic-Scale Dynamics of the Chemical Bond.* The Journal of Physical Chemistry A, 104(24):5660–5694 (**2000**).

[109] Drescher, M., Hentschel, M., Kienberger, R., Uiberacker, M., Yakovlev, V., Scrinzi, A., Westerwalbesloh, T., Kleineberg, U., Heinzmann, U., and Krausz, F. *Time-resolved atomic inner-shell spectroscopy.* Nature, 419(6909):803–807 (**2002**).

[110] Stolow, A., Bragg, A. E., and Neumark, D. M. *Femtosecond Time-Resolved Photoelectron Spectroscopy.* Chemical Reviews, 104(4):1719–1758 (**2004**).

[111] Wu, G., Hockett, P., and Stolow, A. *Time-resolved photoelectron spectroscopy: from wavepackets to observables.* Physical Chemistry Chemical Physics, 13(41):18447–18467 (**2011**).

[112] Griffiths, D. J. *Introduction to Electrodynamics.* Prentice Hall (**1999**). ISBN 978-0-13-805326-0.

[113] Jackson, J. D. *Classical Electrodynamics.* Wiley (**1998**). ISBN 978-0-471-30932-1.

[114] Eichhorn, M. *Laser Physics: From Principles to Practical Work in the Lab.* Springer Science & Business Media (**2014**). ISBN 978-3-319-05128-4.

[115] Shapiro, S. L. *Ultrashort Light Pulses: Picosecond Techniques and Applications.* Springer Science & Business Media (**2013**). ISBN 978-3-662-22574-5.

[116] Antoine, P., L'Huillier, A., and Lewenstein, M. *Attosecond pulse trains using high-order harmonics.* Phys. Rev. Lett., 77(7):1234–1237 (**1996**).

[117] Krausz, F. and Ivanov, M. *Attosecond physics.* Reviews of Modern Physics, 81(1):163–234 (**2009**).

[118] Salieres, P. and Lewenstein, M. *Generation of ultrashort coherent XUV pulses by harmonic conversion of intense laser pulses in gases: towards attosecond pulses.* Measurement Science and Technology, 12(11):1818 (**2001**).

[119] McPherson, A., Gibson, G., Jara, H., Johann, U., Luk, T. S., McIntyre, I. A., Boyer, K., and Rhodes, C. K. *Studies of multiphoton production of vacuum-ultraviolet radiation in the rare gases.* Journal of the Optical Society of America B, 4(4):595 (**1987**).

[120] Ferray, M., L'Huillier, A., Li, X. F., Lompre, L. A., Mainfray, G., and Manus, C. *Multiple-harmonic conversion of 1064 nm radiation in rare gases.* Journal of Physics B: Atomic, Molecular and Optical Physics, 21(3):L31 (**1988**).

[121] Sarukura, N., Hata, K., Adachi, T., Nodomi, R., Watanabe, M., and Watanabe, S. *Coherent soft-x-ray generation by the harmonics of an ultrahigh-power KrF laser.* Physical Review A, 43(3):1669–1672 (**1991**).

[122] Kondo, K., Sarukura, N., Sajiki, K., and Watanabe, S. *High-order harmonic generation by ultrashort KrF and Ti:sapphire lasers.* Physical Review A, 47(4):R2480–R2483 (**1993**).

[123] Akiyama, Y., Midorikawa, K., Matsunawa, Y., Nagata, Y., Obara, M., Tashiro, H., and Toyoda, K. *Generation of high-order harmonics using laser-produced rare-gas-like ions.* Physical Review Letters, 69(15):2176–2179 (**1992**).

[124] Miyazaki, K. and Sakai, H. *High-order harmonic generation in rare gases with intense subpicosecond dye laser pulses.* Journal of Physics B: Atomic, Molecular and Optical Physics, 25(3):L83 (**1992**).

[125] Balcou, P., Cornaggia, C., Gomes, A. S. L., Lompre, L. A., and L'Huillier, A. *Optimizing high-order harmonic generation in strong fields.* Journal of Physics B: Atomic, Molecular and Optical Physics, 25(21):4467 (**1992**).

[126] Crane, J. K., Falcone, R. W., Perry, M. D., and Herman, S. *High-field harmonic generation in helium.* Optics Letters, 17(18):1256 (**1992**).

[127] Arpin, P., Popmintchev, T., Wagner, N. L., Lytle, A. L., Cohen, O., Kapteyn, H. C., and Murnane, M. M. *Enhanced High Harmonic Generation from Multiply Ionized Argon above 500 eV through Laser Pulse Self-Compression.* Physical Review Letters, 103(14):143901 (**2009**).

[128] Seres, E., Seres, J., and Spielmann, C. *X-ray absorption spectroscopy in the keV range with laser generated high harmonic radiation.* Applied Physics Letters, 89(18):181919 (**2006**).

[129] Corkum, P. B. *Plasma perspective on strong field multiphoton ionization.* Physical Review Letters, 71(13):1994–1997 (**1993**).

[130] Kulander, K., Schafer, K., and Krause, J. *Theoretical model for intense field high-order harmonic generation in rare gases.* 3(2):359–364 (**1993**).

[131] Lewenstein, M., Balcou, P., Ivanov, M. Y., L'Huillier, A., and Corkum, P. B. *Theory of high-harmonic generation by low-frequency laser fields.* Physical Review A, 49(3):2117–2132 (**1994**).

[132] Antoine, P., L'Huillier, A., Lewenstein, M., Salieres, P., and Carre, B. *Theory of high-order harmonic generation by an elliptically polarized laser field.* Physical Review A, 53(3):1725–1745 (**1996**).

[133] Keldysh, L. *IONIZATION IN THE FIELD OF A STRONG ELECTROMAGNETIC WAVE.* 20(5):1945 (**1964**).

[134] Posthumus, J. H. *The dynamics of small molecules in intense laser fields.* Reports on Progress in Physics, 67(5):623 (**2004**).

[135] Milošević, D. B., Paulus, G. G., and Becker, W. *High-order above-threshold ionization with few-cycle pulse: a meter of the absolute phase.* Opt. Express, 11(12):1418 (**2003**).

[136] Milošević, D. B., Hasović, E., Busuladžić, M., Gazibegović-Busuladžić, A., and Becker, W. *Intensity-dependent enhancements in high-order above-threshold ionization.* Phys. Rev. A, 76(5) (**2007**).

[137] Hüfner, S. *Photoelectron Spectroscopy: Principles and Applications.* Springer Science & Business Media (**2013**). ISBN 978-3-662-03150-6.

[138] Eland, J. H. D. *Photoelectron Spectroscopy: An Introduction to Ultraviolet Photoelectron Spectroscopy in the Gas Phase.* Elsevier (**2013**). ISBN 978-1-4831-0321-1.

[139] Suga, S. and Sekiyama, A. *Photoelectron Spectroscopy: Bulk and Surface Electronic Structures.* Springer (**2013**). ISBN 978-3-642-37530-9.

[140] Seah, M. P. and Dench, W. A. *Quantitative electron spectroscopy of surfaces: A standard data base for electron inelastic mean free paths in solids.* Surface and Interface Analysis, 1(1):2–11 (**1979**).

[141] Metje, J., Borgwardt, M., Moguilevski, A., Kothe, A., Engel, N., Wilke, M., Al-Obaidi, R., Tolksdorf, D., Firsov, A., Brzhezinskaya, M., et al. *Monochromatization of femtosecond XUV light pulses with the use of reflection zone plates.* Optics Express, 22(9):10747–10760 (**2014**).

[142] Rulliere, C. *Femtosecond Laser Pulses: Principles and Experiments.* Springer (**2007**). ISBN 9780387266749.

[143] Liem, A., Nickel, D., Limpert, J., Zellmer, H., Griebner, U., Unger, S., Tünnermann, A., and Korn, G. *High average power ultra-fast fiber chirped pulse amplification system.* Applied Physics B, 71(6):889–891 (**2000**).

[144] Uhlig, S. *Self-Organized Surface Structures with Ultrafast White-Light: First Investigation of LIPSS with Supercontinuum.* Springer (**2015**). ISBN 978-3-658-09894-0.

[145] Yang, G. and Shen, Y. R. *Spectral broadening of ultrashort pulses in a nonlinear medium.* Optics Letters, 9(11):510 (**1984**).

[146] Alfano, R. R., ed. *The Supercontinuum Laser Source.* Springer-Verlag, New York (**2006**). ISBN 978-0-387-24504-1.

[147] Lochbrunner, S., Huppmann, P., and Riedle, E. *Crosscorrelation measurements of ultrashort visible pulses: comparison between nonlinear crystals and SiC photodiodes.* Optics Communications, 184(1):321–328 (**2000**).

[148] Salières, P., L'Huillier, A., and Lewenstein, M. *Coherence Control of High-Order Harmonics.* Physical Review Letters, 74(19):3776–3779 (**1995**).

[149] Villoresi, P. *Compensation of optical path lengths in extreme-ultraviolet and soft-x-ray monochromators for ultrafast pulses.* Applied Optics, 38(28):6040 (**1999**).

[150] Nugent-Glandorf, L., Scheer, M., Samuels, D. A., Bierbaum, V., and Leone, S. R. *A laser-based instrument for the study of ultrafast chemical dynamics by soft x-ray-probe photoelectron spectroscopy.* Review of Scientific Instruments, 73(4):1875–1886 (**2002**).

[151] Ito, M., Kataoka, Y., Okamoto, T., Yamashita, M., and Sekikawa, T. *Spatiotemporal characterization of single-order high harmonic pulses from time-compensated toroidal-grating monochromator.* Optics express, 18(6):6071–6078 (**2010**).

[152] Igarashi, H., Makida, A., Ito, M., and Sekikawa, T. *Pulse compression of phase-matched high harmonic pulses from a time-delay compensated monochromator.* Optics Express, 20(4):3725 (**2012**).

[153] Poletto, L., Villoresi, P., Frassetto, F., Calegari, F., Ferrari, F., Lucchini, M., Sansone, G., and Nisoli, M. *Time-delay compensated monochromator for the spectral selection of extreme-ultraviolet high-order laser harmonics.* Review of Scientific Instruments, 80(12):123109 (**2009**).

[154] Siffalovic, P., Drescher, M., Spieweck, M., Wiesenthal, T., Lim, Y. C., Weidner, R., Elizarov, A., and Heinzmann, U. *Laser-based apparatus for extended ultraviolet femtosecond time-resolved photoemission spectroscopy.* Review of Scientific Instruments, 72(1):30–35 (**2001**).

[155] Miaja-Avila, L., Lei, C., Aeschlimann, M., Gland, J. L., Murnane, M. M., Kapteyn, H. C., and Saathoff, G. *Laser-Assisted Photoelectric Effect from Surfaces.* Physical Review Letters, 97(11):113604 (**2006**).

[156] Saathoff, G., Miaja-Avila, L., Aeschlimann, M., Murnane, M. M., and Kapteyn, H. C. *Laser-assisted photoemission from surfaces.* Physical Review A, 77(2):022903 (**2008**).

[157] Keis, K., Bauer, C., Boschloo, G., Hagfeldt, A., Westermark, K., Rensmo, H., and Siegbahn, H. *Nanostructured ZnO electrodes for dye-sensitized solar cell applications.* Journal of Photochemistry and Photobiology A: Chemistry, 148(1):57–64 (**2002**).

[158] Srinivasan-Rao, T., Fischer, J., and Tsang, T. *Photoemission studies on metals using picosecond ultraviolet laser pulses.* Journal of Applied Physics, 69(5):3291–3296 (**1991**).

[159] Villeneuve, D. M., Fischer, I., Zavriyev, A., and Stolow, A. *Space charge and plasma effects in zero kinetic energy (ZEKE)photoelectron spectroscopy.* The Journal of Chemical Physics, 107(14):5310–5318 (**1997**).

[160] Zhou, X. J., Wannberg, B., Yang, W. L., Brouet, V., Sun, Z., Douglas, J. F., Dessau, D., Hussain, Z., and Shen, Z. X. *Space charge effect and mirror charge effect in photoemission spectroscopy.* Journal of Electron Spectroscopy and Related Phenomena, 142(1):27–38 (**2005**).

[161] Passlack, S., Mathias, S., Andreyev, O., Mittnacht, D., Aeschlimann, M., and Bauer, M. *Space charge effects in photoemission with a low repetition, high intensity femtosecond laser source.* Journal of Applied Physics, 100(2):024912 (**2006**).

[162] Pietzsch, A., Föhlisch, A., Beye, M., Deppe, M., Hennies, F., Nagasono, M., Suljoti, E., Wurth, W., Gahl, C., Dobrich, K., et al. *Towards time resolved core level photoelectron spectroscopy with femtosecond x-ray free-electron lasers.* New Journal of Physics, 10(3):033004 (**2008**).

[163] Hellmann, S., Rossnagel, K., Marczynski-Bühlow, M., and Kipp, L. *Vacuum space-charge effects in solid-state photoemission.* Physical Review B, 79(3):035402 (**2009**).

[164] Verna, A., Greco, G., Lollobrigida, V., Offi, F., and Stefani, G. *Space-charge effects in high-energy photoemission.* Journal of Electron Spectroscopy and Related Phenomena, 209:14–25 (**2016**).

[165] Siffalovic, P., Drescher, M., and Heinzmann, U. *Femtosecond time-resolved core-level photoelectron spectroscopy tracking surface photovoltage transients on p-GaAs.* EPL (Europhysics Letters), 60(6):924 (**2002**).

[166] Frietsch, B., Carley, R., Döbrich, K., Gahl, C., Teichmann, M., Schwarzkopf, O., Wernet, P., and Weinelt, M. *A high-order harmonic generation apparatus for time- and angle-resolved photoelectron spectroscopy.* Review of Scientific Instruments, 84(7):075106 (**2013**).

[167] Hellmann, S., Sohrt, C., Beye, M., Rohwer, T., Sorgenfrei, F., Marczynski-Bühlow, M., KallÃ¤ne, M., Redlin, H., Hennies, F., M Bauer, et al. *Time-resolved x-ray photoelectron spectroscopy at FLASH.* New Journal of Physics, 14(1):013062 (**2012**).

[168] Oloff, L.-P., Oura, M., Rossnagel, K., Chainani, A., Matsunami, M., Eguchi, R., Kiss, T., Nakatani, Y., Yamaguchi, T., Miyawaki, J., et al. *Time-resolved HAXPES at SACLA: probe and pump pulse-induced space-charge effects.* New Journal of Physics, 16(12):123045 (**2014**).

[169] Al-Obaidi, R., Wilke, M., Borgwardt, M., Metje, J., Moguilevski, A., Engel, N., Tolksdorf, D., Raheem, A., Kampen, T., Mähl, S., et al. *Ultrafast photoelectron spectroscopy of solutions: space-charge effect.* New Journal of Physics, 17(9):093016 (**2015**).

[170] Nazeeruddin, M. K., Zakeeruddin, S. M., Humphry-Baker, R., Jirousek, M., Liska, P., Vlachopoulos, N., Shklover, V., Fischer, C.-H., and Grätzel, M. *Acid-base equilibria of (2, 2‘-bipyridyl-4, 4‘-dicarboxylic acid)ruthenium(II) complexes and the effect of protonation on charge-transfer sensitization of nanocrystalline titania.* Inorganic Chemistry, 38(26):6298–6305 (**1999**).

[171] Grätzel, M. *Recent advances in sensitized mesoscopic solar cells.* Accounts of Chemical Research, 42(11):1788–1798 (**2009**).

[172] Tachibana, Y., Moser, J. E., Grätzel, M., Klug, D. R., and Durrant, J. R. *Subpicosecond Interfacial Charge Separation in Dye-Sensitized Nanocrystalline Titanium Dioxide Films.* The Journal of Physical Chemistry, 100(51):20056–20062 (**1996**).

[173] Hannappel, T., Burfeindt, B., Storck, W., and Willig, F. *Measurement of Ultrafast Photoinduced Electron Transfer from Chemically Anchored Ru-Dye Molecules into Empty Electronic States in a Colloidal Anatase* TiO_2 *Film.* The Journal of Physical Chemistry B, 101(35):6799–6802 (**1997**).

[174] Tachibana, Y., Nazeeruddin, M. K., Grätzel, M., Klug, D. R., and Durrant, J. R. *Electron injection kinetics for the nanocrystalline* TiO_2 *films sensitised with the dye (Bu4n)2ru(dcbpyH)2(NCS)2.* Chemical Physics, 285(1):127–132 (**2002**).

[175] Anderson, N. A. and Lian, T. *Ultrafast Electron Transfer at the Molecule-Semiconductor Nanoparticle Interface.* Annual Review of Physical Chemistry, 56(1):491–519 (**2005**).

[176] Myllyperkiö, P., Benkő, G., Korppi-Tommola, J., Yartsev, A. P., and Sundström, V. *A study of electron transfer in ru(dcbpy) 2 (NCS) 2 sensitized nanocrystalline TiO 2 and SnO 2 films induced by red-wing excitation.* Phys. Chem. Chem. Phys., 10(7):996–1002 (**2008**).

[177] Asbury, J. B., Ellingson, R. J., Ghosh, H. N., Ferrere, S., Nozik, A. J., and Lian, T. *Femtosecond IR Study of Excited-State Relaxation and Electron-Injection Dynamics of Ru(dcbpy)2(NCS)2 in Solution and on Nanocrystalline TiO2 and Al2o3 Thin Films.* The Journal of Physical Chemistry B, 103(16):3110–3119 (**1999**).

[178] Asbury, J. B., Wang, Y.-Q., Hao, E., Ghosh, H. N., and Lian, T. *Evidences of hot excited state electron injection from sensitizer molecules to TiO2 nanocrystalline thin films.* Research on Chemical Intermediates, 27(4-5):393–406 (**2001**).

[179] Asbury, J. B., Anderson, N. A., Hao, E., Ai, X., and Lian, T. *Parameters Affecting Electron Injection Dynamics from Ruthenium Dyes to Titanium Dioxide Nanocrystalline Thin Film.* The Journal of Physical Chemistry B, 107(30):7376–7386 (**2003**).

[180] Bräm, O., Cannizzo, A., and Chergui, M. *Ultrafast fluorescence studies of dye sensitized solar cells.* Phys. Chem. Chem. Phys., 14(22):7934 (**2012**).

[181] Benkö, G., Kallioinen, J., Korppi-Tommola, J. E. I., Yartsev, A. P., and Sundström, V. *Photoinduced ultrafast dye to semiconductor electron injection from nonthermalized and thermalized donor states.* J. Am. Chem. Soc., 124(3):489–493 (**2002**).

[182] Kallioinen, J., Benkö, G., Sundström, V., Korppi-Tommola, J. E. I., and Yartsev, A. P. *Electron transfer from the singlet and triplet excited states of ru(dcbpy) 2 (NCS) 2 into nanocrystalline TiO 2 thin films.* The Journal of Physical Chemistry B, 106(17):4396–4404 (**2002**).

[183] Gerischer, H. *Charge transfer processes at semiconductor-electrolyte interfaces in connection with problems of catalysis.* Surface Science, 18(1):97–122 (**1969**).

[184] Liu, G., Klein, A., Thissen, A., and Jaegermann, W. *Electronic properties and interface characterization of phthalocyanine and Ru-polypyridine dyes on TiO2 surface.* Surface Science, 539(1):37–48 (**2003**).

[185] Snook, J. H., Samuelson, L. A., Kumar, J., Kim, Y.-G., and Whitten, J. E. *Ultraviolet photoelectron spectroscopy of nanocrystalline TiO2 films sensitized with (2,2-bipyridyl)ruthenium(II) dyes for photovoltaic applications.* Organic Electronics, 6(2):55–64 (**2005**).

[186] Lenzmann, F., Krueger, J., Burnside, S., Brooks, K., Grätzel, M., Gal, D., Rühle, S., and Cahen, D. *Surface Photovoltage Spectroscopy of Dye-Sensitized Solar Cells with TiO2, Nb2o5, and SrTiO3 Nanocrystalline Photoanodes: Indication for Electron Injection from Higher Excited Dye States.* The Journal of Physical Chemistry B, 105(27):6347–6352 (**2001**).

[187] Angelis, F. D., Fantacci, S., and Selloni, A. *Alignment of the dye's molecular levels with the TiO2 band edges in dye-sensitized solar cells: a dft tddft study.* Nanotechnology, 19(42):424002 (**2008**).

[188] De Angelis, F., Fantacci, S., Mosconi, E., Nazeeruddin, M. K., and Grätzel, M. *Absorption Spectra and Excited State Energy Levels of the N719 Dye on TiO2 in Dye-Sensitized Solar Cell Models.* The Journal of Physical Chemistry C, 115(17):8825–8831 (**2011**).

[189] Xiong, G., Shao, R., Droubay, T. C., Joly, A. G., Beck, K. M., Chambers, S. A., and Hess, W. P. *Photoemission Electron Microscopy of TiO2 Anatase Films Embedded with Rutile Nanocrystals.* Advanced Functional Materials, 17(13):2133–2138 (**2007**).

[190] Lindblad, R., Cappel, U. B., O'Mahony, F. T. F., Siegbahn, H., Johansson, E. M. J., Haque, S. A., and Rensmo, H. *Energy level alignment in TiO2/metal sulfide/polymer interfaces for solar cell applications.* Physical Chemistry Chemical Physics, 16(32):17099–17107 (**2014**).

[191] Nazeeruddin, M. K., De Angelis, F., Fantacci, S., Selloni, A., Viscardi, G., Liska, P., Ito, S., Takeru, B., and Grätzel, M. *Combined Experimental and DFT-TDDFT Computational Study of Photoelectrochemical Cell Ruthenium Sensitizers.* Journal of the American Chemical Society, 127(48):16835–16847 (**2005**).

[192] Nazeeruddin, M. K., Bessho, T., Cevey, L., Ito, S., Klein, C., De Angelis, F., Fantacci, S., Comte, P., Liska, P., Imai, H., et al. *A high molar extinction coefficient charge transfer sensitizer and its application in dye-sensitized solar cell.* Journal of Photochemistry and Photobiology A: Chemistry, 185(2):331–337 (**2007**).

[193] Rensmo, H., Södergren, S., Patthey, L., Westermark, K., Vayssieres, L., Kohle, O., Brühwiler, P., Hagfeldt, A., and Siegbahn, H. *The electronic structure of the cis-bis(4, 4'-dicarboxy-2, 2'-bipyridine)-bis(isothiocyanato)ruthenium(II) complex and its ligand 2, 2'-bipyridyl-4, 4'-dicarboxylic acid studied with electron spectroscopy.* Chemical Physics Letters, 274(1):51–57 (**1997**).

[194] Hahlin, M., Johansson, E. M. J., Scholin, R., Siegbahn, H., and Rensmo, H. *Influence of Water on the Electronic and molecular surface structures of ru dyes at nanostructured TiO2.* The Journal of Physical Chemistry C, 115(24):11996–12004 (**2011**).

[195] Ai, X., Anderson, N. A., Guo, J., and Lian, T. *Electron injection dynamics of ru polypyridyl complexes on SnO 2 nanocrystalline thin films.* The Journal of Physical Chemistry B, 109(15):7088–7094 (**2005**).

[196] Furube, A., Murai, M., Watanabe, S., Hara, K., Katoh, R., and Tachiya, M. *Near-IR transient absorption study on ultrafast electron-injection dynamics from a Ru-complex dye into nanocrystalline In2o3 thin films: Comparison with SnO2, ZnO, and TiO2 films.* Journal of Photochemistry and Photobiology A: Chemistry, 182(3):273–279 (**2006**).

[197] Haque, S. A., Tachibana, Y., Klug, D. R., and Durrant, J. R. *Charge Recombination Kinetics in Dye-Sensitized Nanocrystalline Titanium Dioxide Films under Externally Applied Bias.* The Journal of Physical Chemistry B, 102(10):1745–1749 (**1998**).

[198] Tamaki, Y., Furube, A., Murai, M., Hara, K., Katoh, R., and Tachiya, M. *Dynamics of efficient electron hole separation in tio nanoparticles.* Physical Chemistry Chemical Physics, 9(12):1453–1460 (**2007**).

[199] Turner, G. M., Beard, M. C., and Schmuttenmaer, C. A. *Carrier Localization and Cooling in Dye-Sensitized Nanocrystalline Titanium Dioxide.* The Journal of Physical Chemistry B, 106(45):11716–11719 (**2002**).

[200] Gundlach, L., Ernstorfer, R., and Willig, F. *Escape dynamics of photoexcited electrons at catechol : TiO2(110).* Physical Review B, 74(3):035324 (**2006**). WOS:000239426700089.

[201] Rego, L. G. C. and Batista, V. S. *Quantum Dynamics Simulations of Interfacial Electron Transfer in Sensitized TiO2 Semiconductors.* Journal of the American Chemical Society, 125(26):7989–7997 (**2003**).

[202] Wang, Z. L. *Nanostructures of zinc oxide.* Materials Today, 7(6):26–33 (**2004**).

[203] Memarian, N., Concina, I., Braga, A., Rozati, S. M., Vomiero, A., and Sberveglieri, G. *Hierarchically Assembled ZnO Nanocrystallites for High-Efficiency Dye-Sensitized Solar Cells.* Angewandte Chemie International Edition, 50(51):12321–12325 (**2011**).

[204] Furube, A., Katoh, R., Hara, K., Murata, S., Arakawa, H., and Tachiya, M. *Ultrafast Stepwise Electron Injection from Photoexcited Ru-Complex into Nanocrystalline ZnO Film via Intermediates at the Surface.* The Journal of Physical Chemistry B, 107(17):4162–4166 (**2003**).

[205] Katoh, R., Furube, A., Yoshihara, T., Hara, K., Fujihashi, G., Takano, S., Murata, S., Arakawa, H., and Tachiya, M. *Efficiencies of Electron Injection from Excited N3 Dye into Nanocrystalline Semiconductor (ZrO2, TiO2, ZnO, Nb2o5, SnO2, In2o3) Films.* The Journal of Physical Chemistry B, 108(15):4818–4822 (**2004**).

[206] Němec, H., Rochford, J., Taratula, O., Galoppini, E., Kužel, P., Polívka, T., Yartsev, A., and Sundström, V. *Influence of the electron-cation interaction on electron mobility in dye-sensitized ZnO and TiO 2 nanocrystals: A study using ultrafast terahertz spectroscopy.* Phys. Rev. Lett., 104(19) (**2010**).

[207] Furube, A., Katoh, R., and Hara, K. *Electron injection dynamics in dye-sensitized semiconductor nanocrystalline films.* Surface Science Reports, 69(4):389–441 (**2014**).

[208] Stockwell, D., Yang, Y., Huang, J., Anfuso, C., Huang, Z., and Lian, T. *Comparison of Electron-Transfer Dynamics from Coumarin 343 to TiO2, SnO2, and ZnO Nanocrystalline Thin Films: Role of Interface-Bound Charge-Separated Pairs.* The Journal of Physical Chemistry C, 114(14):6560–6566 (**2010**).

[209] Bauer, C., Boschloo, G., Mukhtar, E., and Hagfeldt, A. *Electron Injection and Recombination in Ru(dcbpy)2(NCS)2 Sensitized Nanostructured ZnO.* The Journal of Physical Chemistry B, 105(24):5585–5588 (**2001**).

[210] Tachibana, Y., Haque, S. A., Mercer, I. P., Durrant, J. R., and Klug, D. R. *Electron Injection and Recombination in Dye Sensitized Nanocrystalline Titanium Dioxide Films: A Comparison of Ruthenium Bipyridyl and Porphyrin Sensitizer Dyes.* The Journal of Physical Chemistry B, 104(6):1198–1205 (**2000**).

[211] Borgwardt, M., Wilke, M., Kampen, T., Mähl, S., Xiang, W., Spiccia, L., Lange, K. M., Kiyan, I. Y., and Aziz, E. F. *Injection Kinetics and Electronic Structure at the N719/TiO2 Interface Studied by Means of Ultrafast XUV Photoemission Spectroscopy.* The Journal of Physical Chemistry C, 119(17):9099–9107 (**2015**).

[212] Neppl, S., Shavorskiy, A., Zegkinoglou, I., Fraund, M., Slaughter, D. S., Troy, T., Ziemkiewicz, M. P., Ahmed, M., Gul, S., Rude, B., et al. *Capturing interfacial photoelectrochemical dynamics with picosecond time-resolved X-ray photoelectron spectroscopy.* Faraday Discussions, 171(0):219–241 (**2014**).

[213] Siefermann, K. R., Pemmaraju, C. D., Neppl, S., Shavorskiy, A., Cordones, A. A., Vura-Weis, J., Slaughter, D. S., Sturm, F. P., Weise, F., Bluhm, H., et al. *Atomic Scale Perspective of Ultrafast Charge Transfer at a Dye Semiconductor Interface.* The Journal of Physical Chemistry Letters, 5(15):2753–2759 (**2014**).

[214] Veal, T. D., King, P. D. C., Hatfield, S. A., Bailey, L. R., McConville, C. F., Martel, B., Moreno, J. C., Frayssinet, E., Semond, F., and Zuniga-Perez, J. *Valence band offset of the ZnO/AlN heterojunction determined by x-ray photoemission spectroscopy.* Appl. Phys. Lett., 93(20):202108 (**2008**).

[215] Rensmo, H., Westermark, K., Södergren, S., Kohle, O., Persson, P., Lunell, S., and Siegbahn, H. *XPS studies of Ru-polypyridine complexes for solar cell applications.* The Journal of Chemical Physics, 111(6):2744–2750 (**1999**).

[216] Hagfeldt, A. and Grätzel, M. *Molecular Photovoltaics.* Accounts of Chemical Research, 33(5):269–277 (**2000**).

[217] Schwanitz, K., Weiler, U., Hunger, R., Mayer, T., and Jaegermann, W. *Synchrotron-Induced Photoelectron Spectroscopy of the Dye-Sensitized Nanocrystalline TiO2/Electrolyte Interface: Band Gap States and Their Interaction with Dye and Solvent Molecules.* The Journal of Physical Chemistry C, 111(2):849–854 (**2007**).

[218] Antila, L. J., Myllyperkiö, P., Mustalahti, S., Lehtivuori, H., and Korppi-Tommola, J. *Injection and ultrafast regeneration in dye-sensitized solar cells.* J. Phys. Chem. C, 118(15):7772–7780 (**2014**).

[219] Juozapavicius, M., Kaucikas, M., van Thor, J. J., and O'Regan, B. C. *Observation of Multiexponential Pico to Subnanosecond Electron Injection in Optimized Dye Sensitized Solar Cells with Visible Pump Mid Infrared Probe Transient Absorption Spectroscopy.* The Journal of Physical Chemistry C, 117(1):116–123 (**2013**).

[220] Hapiot, P. and Lagrost, C. *Electrochemical Reactivity in Room-Temperature Ionic Liquids.* Chemical Reviews, 108(7):2238–2264 (**2008**).

[221] Aschenbrenner, O., Supasitmongkol, S., Taylor, M., and Styring, P. *Measurement of vapour pressures of ionic liquids and other low vapour pressure solvents.* Green Chemistry, 11(8):1217–1221 (**2009**).

[222] Yoshimura, D., Yokoyama, T., Nishi, T., Ishii, H., Ozawa, R., Hamaguchi, H., and Seki, K. *Electronic structure of ionic liquids at the surface studied by UV photoemission.* Journal of Electron Spectroscopy and Related Phenomena, 144:319–322 (**2005**).

[223] Höfft, O., Bahr, S., Himmerlich, M., Krischok, S., Schaefer, J. A., and Kempter, V. *Electronic Structure of the Surface of the Ionic Liquid [EMIM][Tf2n] Studied by Metastable Impact Electron Spectroscopy (MIES), UPS, and XPS.* Langmuir, 22(17):7120–7123 (**2006**).

[224] Kanai, K., Nishi, T., Iwahashi, T., Ouchi, Y., Seki, K., Harada, Y., and Shin, S. *Anomalous electronic structure of ionic liquids determined by soft x-ray emission spectroscopy: Contributions from the cations and anions to the occupied electronic structure.* The Journal of Chemical Physics, 129(22):224507 (**2008**).

[225] Lovelock, K. R. J., Villar-Garcia, I. J., Maier, F., Steinrück, H.-P., and Licence, P. *Photoelectron Spectroscopy of Ionic Liquid-Based Interfaces.* Chemical Reviews, 110(9):5158–5190 (**2010**).

[226] Villar-Garcia, I. J., Smith, E. F., Taylor, A. W., Qiu, F., Lovelock, K. R. J., Jones, R. G., and Licence, P. *Charging of ionic liquid surfaces under X-ray irradiation: the measurement of absolute binding energies by XPS.* Physical Chemistry Chemical Physics, 13(7):2797–2808 (**2011**).

[227] Ulbrich, A., Reinmöller, M., Beenken, W. J. D., and Krischok, S. *Photoelectron spectroscopy on ionic liquid surfaces Theory and experiment.* Journal of Molecular Liquids, 192:77–86 (**2014**).

[228] Smith, E. F., Garcia, I. J. V., Briggs, D., and Licence, P. *Ionic liquids in vacuo; solution-phase X-ray photoelectron spectroscopy.* Chemical Communications, (45):5633–5635 (**2005**).

[229] Maier, F., Gottfried, J. M., Rossa, J., Gerhard, D., Schulz, P. S., Schwieger, W., Wasserscheid, P., and Steinrück, H.-P. *Surface Enrichment and Depletion Effects of Ions Dissolved in an Ionic Liquid: An X-ray Photoelectron Spectroscopy Study.* Angewandte Chemie International Edition, 45(46):7778–7780 (**2006**).

[230] Mikkola, J.-P., Virtanen, P., Karhu, H., Salmi, T., and Murzin, D. Y. *Supported ionic liquids catalysts for fine chemicals: citral hydrogenation.* Green Chemistry, 8(2):197–205 (**2006**).

[231] Ruta, M., Laurenczy, G., Dyson, P. J., and Kiwi-Minsker, L. *Pd Nanoparticles in a Supported Ionic Liquid Phase: Highly Stable Catalysts for Selective Acetylene Hydrogenation under Continuous-Flow Conditions.* The Journal of Physical Chemistry C, 112(46):17814–17819 (**2008**).

[232] Tao, R., Miao, S., Liu, Z., Xie, Y., Han, B., An, G., and Ding, K. *Pd nanoparticles immobilized on sepiolite by ionic liquids: efficient catalysts for hydrogenation of alkenes and Heck reactions.* Green Chemistry, 11(1):96–101 (**2009**).

[233] Li, X. F., L' Huillier, A., Ferray, M., Lompre, L. A., and Mainfray, G. *Multiple harmonic generation in rare gases at high laser intensity.* Physical Review A, 39(11):5751–5761 (**1989**).

[234] Reinmöller, M., Ulbrich, A., Ikari, T., Preiss, J., Höfft, O., Endres, F., Krischok, S., and Beenken, W. J. D. *Theoretical reconstruction and elementwise analysis of photoelectron spectra for imidazolium based ionic liquids.* Physical Chemistry Chemical Physics, 13(43):19526–19533 (**2011**).

[235] Seidel, R., Faubel, M., Winter, B., and Blumberger, J. *Single-Ion Reorganization Free Energy of Aqueous Ru(bpy)32+/3+ and Ru(H2o)62+/3+ from Photoemission Spectroscopy and Density Functional Molecular Dynamics Simulation.* Journal of the American Chemical Society, 131(44):16127–16137 (**2009**).

[236] Winter, B. and Faubel, M. *Photoemission from Liquid Aqueous Solutions.* Chemical Reviews, 106(4):1176–1211 (**2006**).

[237] Bhasikuttan, A. C., Suzuki, M., Nakashima, S., and Okada, T. *Ultrafast Fluorescence Detection in Tris (2,2 bipyridine)ruthenium(II) Complex in Solution: Relaxation Dynamics Involving Higher Excited States.* Journal of the American Chemical Society, 124(28):8398–8405 (**2002**).

[238] Yoon, S., Kukura, P., Stuart, C. M., and Mathies, R. A. *Direct observation of the ultrafast intersystem crossing in tris(2,2-bipyridine)ruthenium(II) using femtosecond stimulated Raman spectroscopy.* Molecular Physics, 104(8):1275–1282 (**2006**).

[239] Van Houten, J. and Watts, R. J. *Temperature dependence of the photophysical and photochemical properties of the tris(2,2'-bipyridyl)ruthenium(II) ion in aqueous solution.* Journal of the American Chemical Society, 98(16):4853–4858 (**1976**).

[240] Suzuki, K., Kobayashi, A., Kaneko, S., Takehira, K., Yoshihara, T., Ishida, H., Shiina, Y., Oishi, S., and Tobita, S. *Reevaluation of absolute luminescence quantum yields of standard solutions using a spectrometer with an integrating sphere and a back-thinned CCD detector.* Physical Chemistry Chemical Physics, 11(42):9850–9860 (**2009**).

[241] Sauvage, J. P., Collin, J. P., Chambron, J. C., Guillerez, S., Coudret, C., Balzani, V., Barigelletti, F., De Cola, L., and Flamigni, L. *Ruthenium(II) and Osmium(II) Bis(terpyridine) Complexes in Covalently-Linked Multicomponent Systems: Synthesis, Electrochemical Behavior, Absorption Spectra, and Photochemical and Photophysical Properties.* Chemical Reviews, 94(4):993–1019 (**1994**).

[242] Islam, A., Ikeda, N., Yoshimura, A., and Ohno, T. *Nonradiative Transition of Phosphorescent Charge Transfer States of Ruthenium(II) to 2,2 Biquinoline and Ruthenium(II) to 2 2:6,2-Terpyridine in the Solid State.* Inorganic Chemistry, 37(12):3093–3098 (**1998**).

[243] Kobayashi, T., Saito, T., and Ohtani, H. *Real time spectroscopy of transition states in bacteriorhodopsin during retinal isomerization.* Nature, 414(6863):531–534 (**2001**).

[244] Kobrak, M. N. and Li, H. *Electrostatic interactions in ionic liquids: the dangers of dipole and dielectric descriptions.* Physical Chemistry Chemical Physics, 12(8):1922–1932 (**2010**).

Abstract

The ultrafast dynamics of photo excited Ruthenium transition metal complexes and the heterogeneous electron transfer (HET) to nanostructured semiconductor interfaces are investigated by means of time-resolved XUV photoelectron spectroscopy (PES). The process of high-order harmonic generation is utilized to achieve the necessary photon energy of up to 40 eV and a temporal resolution below 100 fs. The capabilities of PES are systematically studied and its advantages compared to other spectroscopic pump-probe methods are demonstrated.

At the interface between the N719 ruthenium dye complex and the commonly used TiO_2 substrate the application of PES allowed to determine for the first time directly the absolute binding energies of the excited states involved in the electron dynamics. The transient signal could be decomposed into the particular contributions. The found energetic structure gives rise to a strong driving force for the injection from the singlet ^{1}MLCT state and a slow electron transfer from the triplet ^{3}MLCT state, the latter being possible due to a partial overlap of the triplet state band of N719 and the conduction band of TiO_2. The lifetimes inferred in this study of (20 ± 10) fs for the ^{1}MLCT and the ^{3}MLCT yielding a slow electron transfer on the picosecond time scale are in excellent agreement with the values reported in literature.

Based on these findings, the interfacial charge transfer from N3 dye molecules into ZnO thin films is analyzed. Previous investigations found that the HET occurs on a generally much slower picosecond timescale related to their TiO_2 counterparts. A comparative study between both interfaces reveals direct evidence for the formation of an interfacial electronic state at ZnO being the origin of the delayed release of free charge carriers into the conduction band. It is further highlighted that ZnO bulk properties such as the conduction band density of states and the energetic band alignment are of minor importance for the electron transfer process whereas the specific dye-ZnO interaction is argued to play a key role in the HET.

In the last part, the ultrafast excited states properties of $[Ru(bpy)_3]^{2+}$ dissolved in ionic liquids (ILs) are investigated. The focus is laid on the general applicability of ILs as solvents with regard to time resolved PES experiments. This material class is known to exhibit extremely low vapor pressures being suitable if UHV conditions are required. It is demonstrated that ILs are beneficial if the frontier molecular orbitals and dynamics of different solutes needs to be addressed. From steady state spectra the HOMO band of the $[Ru(bpy)_3]^{2+}$ molecule, comprised of the Ru t_{2g} orbital, can be clearly distinguished from the solvent contribution. Its absolute binding energy is found to be identical to results obtained from liquid water microjet experiments. From a global fit analysis of the transient signals the binding energies of the initially populated ^{1}MLCT state and the thermally relaxed ^{3}MLCT are determined. The results in terms of a kinetic three state model which includes the intersystem crossing from the ^{1}MLCT to the ^{3}MLCT state as well as a state to account for the intra-molecular vibrational relaxation within the triplet configuration are in good agreement with literature values obtained in aqueous solution.

Kurzzusammenfassung

Diese Arbeit untersucht die Ladungsträgerdynamiken von optisch angeregten Ruthenium Übergangsmetallkomplexen chemisch gebunden auf der Oberfläche von nanostrukturierten Halbleitern mittels zeitaufgelöster Photoelektronen Spektroskopie (PES). Die dazu benötigten ultrakurzen Laserpulse im extremultravioletten Spektralbereich (XUV) werden durch den Prozess der Erzeugung von Hohen Harmonischen bereitgestellt. Die besondere Eignung der zeitaufgelösten PES im Bereich von Farbstoff-Halbleiter Grenzflächen sowie die Vorteile gegenüber anderen spektroskopischen Methoden werden aufgezeigt.

Unter Verwendung von PES konnten erstmalig an der Grenzfläche zwischen dem Farbstoffkomplex N719 und dem Halbleitersubstrat TiO_2 direkt die absoluten Bindungsenergien der am Ladungstransfer beteiligten angeregten Zustände bestimmt werden. Die Positionen der Energieniveaus des Singulett ^{1}MLCT Zustandes wurden mit 0.7 eV über sowie die des Triplett ^{3}MLCT Zustandes mit 0.2 eV unter dem Leitungsbandminimum gefunden. Dies bedeutet für den erstgenannten Zustand eine große Triebkraft für den Ladungstransfer und stellt die Hauptursache für die ultrakurzen Lebenszeiten im Bereich von (20 ± 10) fs dar. Im Gegensatz dazu ist eine Ladungsträgerinjektion vom tieferliegenden Triplett Zustand nur aufgrund einer partiellen Überlappung mit dem Leitungsband des Halbleiters möglich und erklärt die in diesem Fall gefundenen deutlich langsameren Injektionszeiten im Pikosekundenbereich.

Unter Zuhilfenahme der bisherigen Erkenntnisse auf der TiO_2 Oberfläche wurde nachfolgend der Ladungstransfer an ZnO Schichten untersucht. Hier ergaben frühere Untersuchungen, dass die Elektroneninjektion vorwiegend im Pikosekundenbereich stattfindet. Die Ursache konnte in einer vergleichenden Studie in der Bildung eines Grenzflächenzustandes zwischen Farbstoff und Halbleiter gefunden werden. Dadurch stehen diese nicht mehr unmittelbar als freie Ladungsträger zur Verfügung und es kommt zu einer erhöhten Rekombination in den Grundzustand. Dabei ist besonders hervorzuheben, dass die Stoffeigenschaften von ZnO wie z.B. die Zustandsdichte im Leitungsband sowie dessen relative Lage zu den ladungsträgerinjizierenden Zuständen des Farbstoffmoleküls nur eine untergeordnete Rolle spielen und vielmehr die Wechselwirkung zwischen Farbstoff und Halbleiter von zentraler Bedeutung ist.

Abschließend wurde die Eignung von Ionischen Flüssigkeiten (IL) in Bezug auf die Anwendung im Ultrahochvakuum untersucht. Dabei wurde überprüft, ob die ultraschnellen Ladungsträgerdynamiken des in IL gelösten Farbstoffmoleküls $[Ru(bpy)_3]^{2+}$ gezielt adressiert werden können. Es zeigt sich dabei, dass aufgrund der positiven Eigenschaften des Lösungsmittels eine klare Differenzierung zwischen den Valenzbändern von Farbstoff und Lösungsmittel möglich ist. Weiterführende Untersuchen von Ladungstransferprozessen und Farbstoff Halbleiter System in flüssiger Umgebung werden diskutiert.

Publications

Articles directly related to this work

1. M. Borgwardt, M. Wilke, I. Kiyan and E. F. Aziz
   Ultrafast excited states dynamics of $[Ru(bpy)_3]^{2+}$ dissolved in ionic liquids
   Phys. Chem. Chem. Phys., 18, 28893-28900 (2016). doi: 10.1039/C6CP05655E

2. M. Borgwardt, M. Wilke, T. Kampen, S. Mähl, M. Xiao, L. Spiccia, K. Lange. I. Kiyan and E. F. Aziz
   Charge Transfer Dynamics at Dye-Sensitized ZnO and TiO2 Interfaces Studied by Ultrafast XUV Photoelectron Spectroscopy
   Sci. Rep., 6, 24422 (2016). doi: 10.1038/srep24422

3. M. Borgwardt, M. Wilke, T. Kampen, S. Mähl, W. Xiang, L. Spiccia, K.M. Lange, I. Kiyan, E.F. Aziz
   Capturing Charge Transfer Dynamics with Ultrafast Time-Resolved XUV Photoelectron Spectroscopy at Dye - Semiconductor Interfaces
   Proceedings EUPVSEC (2015), doi: 10.4229/EUPVSEC20152015-1AO.1.2

4. M. Borgwardt, M. Wilke, T. Kampen, S. Mähl, W. Xiang, L. Spiccia, K. Lange. I. Kiyan and E. F. Aziz
   Injection Kinetics and Electronic Structure at the N719/TiO2 Interface Studied by Means of Ultrafast XUV Photoemission Spectroscopy
   J. Phys. Chem. C, 119, 9099-9107 (2015). doi: 10.1021/acs.jpcc.5b01216

5. R. Al-Obaidi, M. Wilke, M. Borgwardt, J. Metje, A. Moguilevski, N. Engel, D. Tolksdorf, A. Raheem, T. Kampen, S. Mähl, I. Kiyan and E. F. Aziz
   Ultrafast photoelectron spectroscopy of solutions: space-charge effect
   New J. Phys., 17, 93016, (2015). doi: 10.1088/1367-2630/17/9/093016

6. J. Metje, M. Borgwardt, A. Moguilevski, A. Kothe, N. Engel, M. Wilke, R. Al-Obaidi, D. Tolksdorf, A. Firsov, M. Brzhezinskaya, A. Erko, I. Kiyan and E. F. Aziz
   Monochromatization of femtosecond XUV light pulses with the use of reflection zone plates
   Opt. Express, 22, 10747–60, (2014). doi: 10.1364/OE.22.010747

Author Contributions:

- Articles 1), 2), 3), 4): M. B. designed and carried out the experiment, performed the sample characterization measurements, analyzed the data, prepared figures and wrote the manuscript.
- Articles 5), 6): M.B. carried out the experiment, performed the sample characterization measurements, analyzed the data and prepared figures. M. B. further took part in discussions throughout the work, and revising of the manuscripts

Acknowledgements

I would like to express my deepest gratitude to all the people who helped me to realize this thesis...

...Prof. Dr. Emad Aziz, for giving me the opportunity to join his team and to write this thesis, for frequent motivation, for sharing his experience and lots of scientific inspiration.

...Prof. Dr. Ludger Wöste for his willingness to evaluate this thesis but even more as one of the best and inspiring reader I had during my studies at the Freie Universität Berlin.

...Prof. Leone Spiccia for providing me with a variety of fascinating materials and substantial scientific discussion.

...Dr. Igor Kiyan for taking excellent care of the laser system, for the technical assistance and for co-supervising my thesis. His experience and attention to details in the experiments was always helpful.

...Dr. Kathrin Lange-Aziz for the arrangement of research opportunities and fruitful discussions.

...Martin Wilke. I'm grateful for the daily exchange of scientific thoughts, for his drive to realize experimental ideas, our joint fight with Mathematica and many more things. His presence during the past three years pushed me towards higher level.

...Dr. Thomas Dittrich und Prof. Dr. Thomas Hannappel for giving exciting lectures in the field of solar energy conversion and inspiring me to focus on this research topic.

...Dr. Philipp Sippel, Dr. Klaus Schwarzburg und Dr. Rainer Eichberger as previous supervisors during my master thesis who introduced me to the ultrafast world of fs-lasers. They have taught me all the fundamental principles that were necessary to be successful within the last three years.

...the entire FU team. I enjoyed the pleasant and productive working environment over the years and want to thank Jan Metje, Ruba Al-Obaidi, Nicholas Engel, Alexandre Moguilevski, Daniel Tolksdorf, Azhr Abdulzahraa Raheem and Dr. Christoph Merschjann.

...and the Bessy Team for their technical support, lending me instruments and tools, by sharing consumables and generally giving valuable scientific or technical advices. I want to thank Dr. Bernd Winter, Dr. Kaan Atak, Tim Brandenburg, Dr. Tristan Petit, Marvin Pohl, Isaak Unger, Dr. Jie Xiao and Dr. Ronny Golnak.

Selbständigkeitserklärung

Hiermit erkläre ich, dass ich die vorliegende Dissertation selbständig und nur mit Hilfe der angegebenen Quellen angefertigt habe. Ich versichere, dass diese Arbeit nicht in einem vorhergehenden Promotionsverfahren angenommen wurde oder als ungenügend beurteilt wurde.

Mario Borgwardt
Berlin, den 13.07.2016